LBL-23450
c.2

Lawrence Berkeley Laboratory
UNIVERSITY OF CALIFORNIA

RECEIVED
LAWRENCE
BERKELEY LABORATORY

JUL 31 1987

LIBRARY AND
DOCUMENTS SECTION

LOCAL HUMAN SKIN POTENTIAL-SPATIAL DISTRIBUTION, MAGNITUDE AND ORIGIN

C. Cullander
(Ph.D. Thesis)

April 1987

TWO-WEEK LOAN COPY
This is a Library Circulating Copy which may be borrowed for two weeks.

Donner Laboratory
Biology & Medicine Division

Prepared for the U.S. Department of Energy under Contract DE-AC03-76SF00098

LBL-23450
c.2

DISCLAIMER

This document was prepared as an account of work sponsored by the United States Government. While this document is believed to contain correct information, neither the United States Government nor any agency thereof, nor the Regents of the University of California, nor any of their employees, makes any warranty, express or implied, or assumes any legal responsibility for the accuracy, completeness, or usefulness of any information, apparatus, product, or process disclosed, or represents that its use would not infringe privately owned rights. Reference herein to any specific commercial product, process, or service by its trade name, trademark, manufacturer, or otherwise, does not necessarily constitute or imply its endorsement, recommendation, or favoring by the United States Government or any agency thereof, or the Regents of the University of California. The views and opinions of authors expressed herein do not necessarily state or reflect those of the United States Government or any agency thereof or the Regents of the University of California.

LBL-23450

LOCAL HUMAN SKIN POTENTIAL - SPATIAL DISTRIBUTION, MAGNITUDE AND ORIGIN

Christopher Cullander

Ph.D. Thesis

Lawrence Berkeley Laboratory
University of California
Berkeley, California 94720

April 1987

This work was supported in part by Public Health Service Fellowship No. 5 T32 GM07379-03, by the U.S. Department of Energy under Contract No. DE-AC03-76SF00098, and also by the National Institute of Health, National Heart, Lung, and Blood Institute under Grant No. PO1 HL25840-01.

LOCAL HUMAN SKIN POTENTIAL - SPATIAL DISTRIBUTION, MAGNITUDE AND ORIGIN

Christopher Cullander

ABSTRACT

This thesis is an investigation of the sources and distribution of the slowly-varying electric potential across hairy skin and the spatial distribution of the eccrine gland pores, which may be related to the skin potential. The electrical characterization of skin may lead to non-invasive means of quantifying skin and skin diseases and monitoring the effectiveness and progress of dermatologic treatment as well as providing insight into fundamental skin physiology.

The transdermal electrical potential in the same area on the back of the hands of eight subjects was measured under experimental conditions designed to minimize eccrine gland activity. The mean potential over all subjects was 24.86±8.16 mV. The pore distribution was evaluated by transferring the imprint of pilocarpine-stimulated gland secretions on special paper to digitized arrays. The average gland count over all records for the mean electrode radius (1 mm) was 9.09±3.55 glands.

The correlation between the measured potential and the number of glands at each measurement site was calculated, and in general, the measured potential was independent of gland count. Where some correlation was observed, it was probably due to experimental error. Care was taken to ensure that both distributions were adequately sampled. This lack of correlation was consistent with an equivalent circuit model for non-sudorific potential generation. This model predicted a minimal

contribution from the passive glands and the existence of at least one other source of potential. One such source is regional variability in the permeability barrier of the skin.

The pore location arrays were also used to make a spectral analysis of the spatial frequencies present in the point pattern. Radial profiles of the power spectra and autocorrelation estimates demonstrated that the inter-pore distance is nearly constant (0.49 $\pm$0.043 mm). The larger scale periodicity of 1.84$\pm$0.35 mm is related to the absence of glands surrounding hair follicles. This is evidently the first application of Fourier-transform based cross-correlation techniques to the spectral analysis of an anatomically-related spatial point pattern. Simulations of gland distributions by a stochastic model were used to verify the uniqueness of the findings.

Dedication

This thesis is dedicated to my wife Helen, in token of her support and encouragement during my graduate career.

Acknowledgements

I would like to thank all those who contributed to this project, particularly Dr. Budinger and the members of the Research Medicine Group; Dorothy Denny and the Donner library staff; Frank Upham and his co-workers in the Electronics Shop; Pete Dowling and his fellow machinists, and the many people who volunteered as experimental subjects.

Contents

Dedication i

Acknowledgements i

1 Introduction 1

1.1 Motivation 1

1.2 Potential as the variable of interest 2

1.3 Review of the literature 2

1.4 Outline of thesis 5

2 Sources of Non-Sudorific Transdermal Potential 6

2.1 Summary 6

2.2 The anatomy and physiology of skin 6

2.2.1 Overview 6

2.2.2 Influence of skin type on potential measurements 7

2.3 The epidermis and skin permeability 8

2.3.1 Epidermal cornification 8

2.3.2 The permeability barrier of the skin 9

2.3.3 The barrier as a source of potential 10

2.3.4 Sub-barrier permeability 12

2.4 Dermis and subdermis 12

2.4.1 Structure and function 12

2.4.2 Dermal contributions to the transdermal potential 13

2.5 Eccrine glands 14

2.5.1 Structure and function 14

2.5.2 Contributions to potential from non-secreting glands 15

2.6 Hair follicles 16

2.6.1 Structure and function 16

2.6.2 Contributions to potential by the hairs 16

2.7 Additional biological sources 17

2.8 The influence of regional variation in skin on electrical measurements 17

3 Measurement of Slowly-varying Transdermal Potentials - Materials and Methods 19

3.1 Summary 19

3.2 Electrolyte, electrodes and interfaces 21

3.2.1 Electrolyte 22

3.2.2 Fabrication and selection of electrodes 22

3.2.3 Connections from electrode to skin 23

3.2.4 Electrode terminations 24

3.2.5 Syringe micropump for search electrode 26

3.2.6 Measurement of electrode area in the dehydrated skin 26

3.2.7 Stabilization of interfaces 27

3.2.8 Maintenance of electrodes and electrode apparatus 28

3.3 Spatial positioning references 28

3.3.1 Establishment of a common fixed reference frame 29

3.3.2 Establishing correspondence between measures in the same area 29

3.4 Amplification, recording and electrical environment 32

3.4.1 Determination of source resistance 32

3.4.2 Preamplifier circuit 33

3.4.3 Signal flow, final amplification and recording 33

3.4.4 Reduction of noise and interference 35

3.4.5 Establishment of earth ground 35

3.5 Eccrine gland imaging 36

3.5.1 Print method of pore location 36

3.5.2 Pilocarpine iontophoresis 37

3.5.3 Location of gland centers 37

3.6 Summary of study protocols 39

3.6.1 Selection of subjects 39

3.6.2 Preparation of skin for in-vivo potential measurement 40

3.6.3 Potential measurement and gland location 41

3.7 Attempts to constrain the in-vivo system 42

3.8 Physical and biological model systems for skin electrical behavior . . 44

3.8.1 In-vitro human skin as a model membrane 44

3.8.2 Artificial membrane models 46

3.9 Measurement requirements 47

3.9.1 Limitations on size of test area 47

3.9.2 Choice of electrodes and electrolyte 48

3.9.3 Location of test area 49

4 Experimental Results and Statistical Analysis 50

4.1 Summary 50

4.2 Results of potential measurements 50

4.2.1 Potential contributions from hair follicles and other sources . 54

4.3 Results of gland location analysis 56

4.4 Registering the potential grid with the gland locations 57

4.5 Choice of analysis and formulas used 59

4.6 Results of statistical analysis 62

4.6.1 Sampling considerations 63

4.6.2 Statistical analysis 65

4.6.3 Discussion 65

5 Modelling Non-sudorific Electrical Potential Behavior of the Skin 72

5.1 Overview 72

5.2 A circuit model for skin 73

5.2.1 Simplifying assumptions 73

5.2.2 Paths of current flow in the skin 73

5.3 Analysis of the circuit model 74

5.4 Determination of circuit element values 77

5.4.1 Estimating resistances 77

5.4.2 Estimation of resistivities for the barrier layer and stratum corneum 78

5.4.3 Constraints on the resistivity of the epidermal duct wall . . . 79

5.4.4 Formulas for the resistances of skin structures 81

5.4.5 Structural dimensions 82

5.4.6 Choice of values for voltage sources 83

5.5 Behavior of the model 84

5.5.1 Potential as a function of the number of glands 84

5.5.2 Potential as a function of barrier properties 88

5.6 Summary of modelling results 90

5.7 Discussion of model 91

6 Detection of Pore Pattern by Fourier Analysis 104

6.1 Summary 104

6.2 Two-dimensional Fourier transform analysis 105

6.2.1 Theory 105

6.2.2 Implementation 106

6.2.3 Radial profile representation of the spatial power spectrum and the autocorrelation estimate 107

6.2.4 The effects of zero-filling and windowing on the radial profile 109

6.3 Analysis results and interpretation 114

6.3.1 Gland location power spectra 114

6.3.2 Gland location autocorrelation estimates 119

6.4 Interpretation of results 122

6.5 Simulations and modelling 124

6.5.1 Cumulative inversion 124

6.5.2 Derivation of the interpoint distance distribution 125

6.5.3 Derivation of the distribution of points in a circular field . . . 127

6.6 Results of simulations 129

6.7 Comparison of Fourier analysis with conventional methods for detection of pattern. 132

7 Conclusions **136**

7.1 Summary of results 136

7.2 Inactive glands as a source of potential 136

7.3 Potential contributions from hairs 137

7.4 Evaluation of methods 138

7.5 Spatial distribution patterns of eccrine glands 138

7.6 Directions for future investigations 139

8 Bibliography **141**

A Human Use Approvals **154**

List of Tables

1 *Summary of potential measurements, including mean estimated number of glands for an electrode radius of one mm. The mean $\overline{X}_\psi$ and sample variance σ of the potentials are in mV.* 52

2 *Summary of gland location results.* 58

3 *Summary of statistical results. Numbers in () indicate counts if only the central five radii (0.9 to 1.1 mm) are considered.* [1]*Rejection Level of Null hypothesis,* [2]*Not Rejected.* 66

4 *Variable values for ρ_{bar} and ρ_{sc}. ρ_{sc} is a function of t_{epi}, t_{bar}, t_{sc} and ρ_{epi}, and varies with them. The middle column of ρ_{bar} (8.0, 3.5 and 1.27) are base values. 'B' denotes 'both'.* 79

5 *Variable values. (*) denotes a base value.* 84

6 *Nine-point range and spread of modelling plots. Barrier thicknesses are 'T' = 10.0 μm, 't' = 4.0 μm, and 'V' if t_{bar} varies. Potential (ψ) increased ($\nearrow$), decreased ($\searrow$), or stayed the same ($\equiv$) as the parameter increased. Starred (*) values did not change.* 86

7 *Nine-point range and spread of modelling plots (continued) . Barrier thicknesses are 'T' = 10.0 μm, 't' = 4.0 μm, and 'V' if t_{bar} varies. Potential (ψ) increased ($\nearrow$), decreased ($\searrow$), or stayed the same ($\equiv$) as the parameter increased. Starred (*) values did not change.* . . . 87

8 *Nine-point range and spread of modelling plots (continued). Barrier thicknesses are 'T' = 10.0 μm, 't' = 4.0 μm, and 'V' if t_{bar} varies. Potential (ψ) increased (↗), decreased (↘), or stayed the same (≡) as the parameter increased. Starred (*) values did not change.* . . . 89

9 *Interpattern distances associated with peaks of low spatial frequency. $\overline{X}$ is the arithmetic mean, and σ_u is the unbiased estimate of the standard deviation for all samples [98]. All measures are in mm.* . . 120

10 *Interpattern distances associated with profile minima and peaks with high spatial frequency. $\overline{X}$ is the arithmetic mean, and σ_u is the unbiased estimate of the standard deviation for all samples [98]. All measures are in mm.* 121

List of Figures

1 *Cross-sectional anatomy of non-glabrous skin showing possible transcorneal routes of water-soluable compounds.* 7

2 *Schematic diagram of experimental apparatus.* 20

3 *Details of an electrode body and the test electrode termination.* 23

4 *Schematic of complete search electrode assembly with bridge and syringes.* 24

5 *Sandwich apparatus and detail of isolation ring.* 25

6 *Flange, lucite piston and marking jig for fiducial marks.* 31

7 *Data sheet for LF352D instrumentation amplifier. (Component values used in the 'typical' circuit above were* R_c*=160* Ω*,* C_c*=0.002* μF*,* R_g*=10* $K\Omega$ *and* R_s*=1* $M\Omega$*).* 34

8 *Top and two side views of the holed petri dish lid used to mount the model membranes.* 45

9 *Portion of chart output for potential record hs3cor.pr. The upper trace is the drift, with the experimental record below it. Vertical scale is 1.0 mV/small division, horizontal scale is 0.5 minute/large division(five small divisions).* 53

10 *Potential grids for all subjects. Certain anomalous values (circled) are discussed in the text. Sites indicated by 'nm' or 'om' were not correlated.* 55

11 *The proximity arrays associated with one group of fiducials for sample k42b. Array locations labelled 'nm' fell outside the measurement site on the skin.* 60

12 *Results of the analysis of one of the proximity arrays for sample k42b versus the potential record jkcor.pr. An 'nm' indicates that the site was not measured.* 61

13 *Plots of correlation coefficient versus electrode radius for samples h36r (upper left), h43b (lower left), h54b (upper right), and h53b (lower right).* 68

14 *Plots of correlation coefficient versus electrode radius for samples h55r (upper left), m46b (lower left), j44b (upper right), and m42r (lower right).* 69

15 *Plots of correlation coefficient versus electrode radius for samples k42b (upper left), k42r (lower left), p53r (upper right), and p54b (lower right).* 70

16 *Plots of correlation coefficient versus electrode radius for samples h41r (upper left), h44r (lower left), j43b (upper right), and k44b (lower right).* 71

17 *(a). Paths of current flow in the skin. (b). The complete circuit model (c). The simplified circuit model with one gland and one epidermal element (d) The simplified model with two glands in parallel with a single epidermal component.* 75

18 *The variation of ρ_{sc} as a function of ρ_{bar}* 80

19 *Representative plot for plots 1, 2 and 15.* 93

20 *Representative plot for plots 3 and 5.* 94

21 *Representative plot for plots 4, 6, 20, 22, 24, 26, 32, and 34.* 95

22 *Representative plot for plots 7, 9, 11, 13, and 17.* 96

23 *Representative plot for plots 8, 10, 12, 14, 16, and 18.* 97

24 *Representative plot for plots 19 and 21.* 98

25 *Representative plot for plots 23, 25, 31 and 33.* 99

26 *Representative plot for plots 27 and 29.* 100

27 *Representative plot for plots 28 and 30.* 101

28 *Representative plot for plots 35 through 38.* 102

29 *Representative plot for plots 39 through 42.* 103

30 *False overlaps (shaded area) contribute to the autocorrelation (crosshatched area) unless the image is surrounded by a frame of zeros.* 106

31 *Each bin in the radial profile represents the mean intensity per pixel at integral radius m in the 2-D image.* 108

32 *Comparison of power spectum radial profiles of complete (1024x1024) and reduced (512x512) datasets for sample h44r.* 110

33 *Comparison of autocorrelation estimate radial profiles of complete (1024x1024) and reduced (512x512) datasets for sample h44r.* 111

34 *Comparison of power spectrum profiles of an unwindowed square (solid), unwindowed pillbox (shortdashed), and a pillbox with its edge tapered by a circular Hanning window (dotted line). Note that DC and near-DC values are present in these profiles, and that only the first 30 bins are represented.* 113

35 *Effect of various windows on the power spectrum profile of a pillbox.* 115

36 *Effect of various windows on the power spectrum profile of data.* . . . 116

37 *The 'hole' maximum in the power spectrum profile.* 118

38 *Trapezoidal probability density function used to determine interpoint distances.* 126

39 *Insertion of a new point. The location at* (θ_1, r_1) *is not accepted since the new radius of exclusion intersects with an old one. A successful insertion occurs at* (θ_2, r_1). 129

40 *Visual fit of mean profiles to a data profile.* 131

41 *Power spectrum profile of data simulation.* 133

42 *Autocorrelation estimate profile of data simulation.* 134

43 *EDF plot of nearest neighbor distances for biological cells, where the dark line is data and dashed lines are upper and lower envelopes from 99 simulations of CSR (from Diggle [102]).* 135

1 Introduction

A nearly constant transdermal electrical potential can be measured across human skin. The magnitude of this voltage varies with the site of the measurement, but is usually negative with respect to the interior of the body, with typical values ranging from +30 to -50 mV [1,2,3]. The source or sources of this steady potential are not known, but the primary candidates are the eccrine glands and the structures that make up the permeability barrier of the skin [4,5]. This thesis is a characterization of the nature and spatial distribution of the skin potential and an investigation of the sources of the steady skin potential level across hairy skin. A second objective is the characterization of the distribution of eccrine gland pores on the surface of the skin in order to determine if these glands are essential determinants of the electric potentials.

1.1 Motivation

There are several reasons for looking at skin as an electrical entity. As Cole and Curtis have pointed out [6], accurate specification of the electrical characteristics of any tissue is in itself as important as any other objective measurement that can be made under given physiological or pathophysiological conditions. In addition, electrical changes related to variations in structure or function are often much greater than the associated thermal or mechanical changes [7], and electrical measurement technology is well developed. Skin is of particular interest because there is a need for non-invasive means of quantifying skin and skin diseases [5,8,9] and ways of monitoring the effectiveness and progress of dermatologic treatment.

Insight into the basis of skin electrical behavior may also lead to the development of diagnostic methods for exocrine disorders [10] and better methods of electrically facilitated transdermal drug delivery (iontophoresis [11]), as well as providing insight into fundamental skin physiology.

1.2 Potential as the variable of interest

Several considerations influenced the choice of skin potential as the variable of interest. The transdermal potential is endogenous, i.e. it originates from the skin itself, whereas the measurement of impedance or conductance involves the application of an external voltage of some set magnitude and frequency. The imposition of a voltage across the skin might easily affect its physiology and alter its electrical behavior. An additional problem with exogenous measures is that the path of current flow in a complex tissue is usually not known and may also change with time or as a function of the magnitude and frequency of the applied voltage. Finally, exogenous measurements require the passage of current through the electrode. This current affects the electrochemistry of the electrode-tissue interface [12], so that a second electrode pair must be used to measure the voltage drop across the tissue. As will be seen, this requirement would be difficult to meet with the electrodes used in these studies.

1.3 Review of the literature

Historically, interest in the skin as an electric organ has been limited (with some exceptions [13]) to psychophysiology [4,14,15], where attempts have been made to

correlate variations in skin potential (as well as skin resistance and conductance) with changes in an experimental subject's emotional state. Potential differences with respect to the skin have been measured (often with confusing results) in relation to ovulation, wound healing, and in the location of acupuncture points. Woodrough's thesis [1] contains a good review of these topics. Recent investigations of the electrical characteristics of skin have included studies of potentials associated with mechanical stress [16,17,18,19], eccrine glands [20,21], dermal pathology [5], and injury to the skin [2,3] as well as potentials associated with the normal functioning of skin [1,2,3,5]. In related investigations, Quinton and his co-workers [20,21] and Sato [22] have described a link between high sweat gland transluminal potentials and abnormal chloride permeability in cystic fibrosis, and other investigators have used potential measurements as a functional assessment of the walls of the esophagus and nasal passages [23,24,25].

Despite this interest, the origin of the steady potential difference across skin remains poorly understood. With the exception of Woodrough's research [1,5], which is not widely available, the review by Fowles [4] is the most recent attempt to specify the origins of the potential difference across skin and derive a consistent model for it. Fowles' model incorporates and extends the work of Edelberg, who later published a less detailed version of a similar model [26]. The oft-cited paper by Christie [27] adopts Fowles' model and does not add substantially to it. In this model, the steady potential difference (his term is the skin potential level or SPL) receives contributions from both a 'sweat gland component' and an 'epidermal component'. The sweat gland component consists of a potential across the dermal portion of the gland duct and a smaller contribution from the epidermal portion,

while the epidermal component is ascribed to a passive potential that exists due to an unidentified structure in the skin behaving like a semipermeable membrane. While his arguments are plausible, there is no direct experimental evidence cited in support of either hypothesis.

Woodrough [1,5] was primarily interested in applying measurements of slowly-varying electrical potential differences clinically. Consequently, he was more interested in looking for differences between normal skin and pathological or injured tissue than in identifying the sources of the potentials measured. Nevertheless, his research makes two important contributions, the first being an acknowledgement of the importance of the electrolyte employed in the measurements[1]. Many studies of skin potentials are unreliable because either the electrodes used were not capable of low-frequency measurements, or because the electrolyte strength or composition was not physiological or inappropriate for the electrode. Woodrough also stresses the need to define the state of the sweat glands during the potential measurement, a point which may seem obvious but which has usually been neglected. One important question is the state of the duct lumen under various conditions, particularly whether there is saline in it at all times.

Woodrough's model was constructed by connecting all the possible sources of potential in the skin together in a network. The result is very similar to Fowles' model, but is complicated by the addition to the circuit of hypothetical potentials associated with the pilosebaceous apparatus. Woodrough claims that the model

[1]Recognition of the importance of non-biological factors (for example, the input impedance of the amplifier used) in the measurement of DC biopotentials has been slow in coming. Investigations continue to be made with electrodes, electrolytes, amplification and signal conditioning that are unsuitable for the experimental conditions despite the widespread availability of prescriptions [27,28,29] to the contrary.

predictions of electrolyte concentration potential are quantitatively consistent with experimental measurements, but makes no attempt to substitute values for any of the variables. The benefit of this rather abstract formulation is the recognition that a liquid junction potential may exist between the sweat in the duct and the electrode electrolyte.

1.4 Outline of thesis

This thesis begins with a description of skin anatomy and physiology, and discusses relationships between skin structure and function and its non-sudorific potential (Chapter 2). The specification of the materials and methods used to measure the potential follows, along with a description of the techniques employed to quantify the distribution of pores in the measurement area. Experiments made with model systems are also described (Chapter 3). The results of the potential measurement and the gland location analysis are analyzed and discussed in Chapter 4. In Chapter 5, an equivalent circuit model of the non-sudorific electrical potential behavior of the skin is constructed and analysed. Chapter 6 is an account of the detection of a pattern in the gland locations by a Fourier spectral analysis of the spatial frequencies present within the distribution, and Chapter 7 includes a summary of the thesis research findings and the conclusions.

2 Sources of Non-Sudorific Transdermal Potential

2.1 Summary

This chapter concerns the relationship between skin structure and function and its non-sudorific electrical potential. Possible sources of spatial variations in transdermal potential are differences in skin thickness or permeability and the number of hair follicles or sweat glands in the measurement area [5,4,26,30]. Effects on the potential of regional variations in structure are discussed. Other factors that can influence the measurement, such as mechanical deformation, temperature, relative humidity, and site preparation are considered elsewhere.

2.2 The anatomy and physiology of skin

2.2.1 Overview

Skin[2] is composed of three distinct layers. The outermost layer, the stratified epithelium of the epidermis, contains the permeability barrier of the skin. Beneath this is the dermis or corium, which consists primarily of connective tissue. The epidermis and the dermis each consist of several distinct strata and contain characteristic cells, tissues and organs (Figure 1). The various skin appendages (eccrine and apocrine glands, hair follicles and sebaceous glands) traverse both layers. The third layer, beneath the dermis, is adipose tissue. Although the epidermis and

[2]Sources of additional information on skin anatomy and physiology are: Moschella and Huxley [31]; Millington and Wilkinson [30], which has a section on the mechanical, thermal and electrical properties of skin; and the series on the skin and skin diseases edited by Jarrett [32].

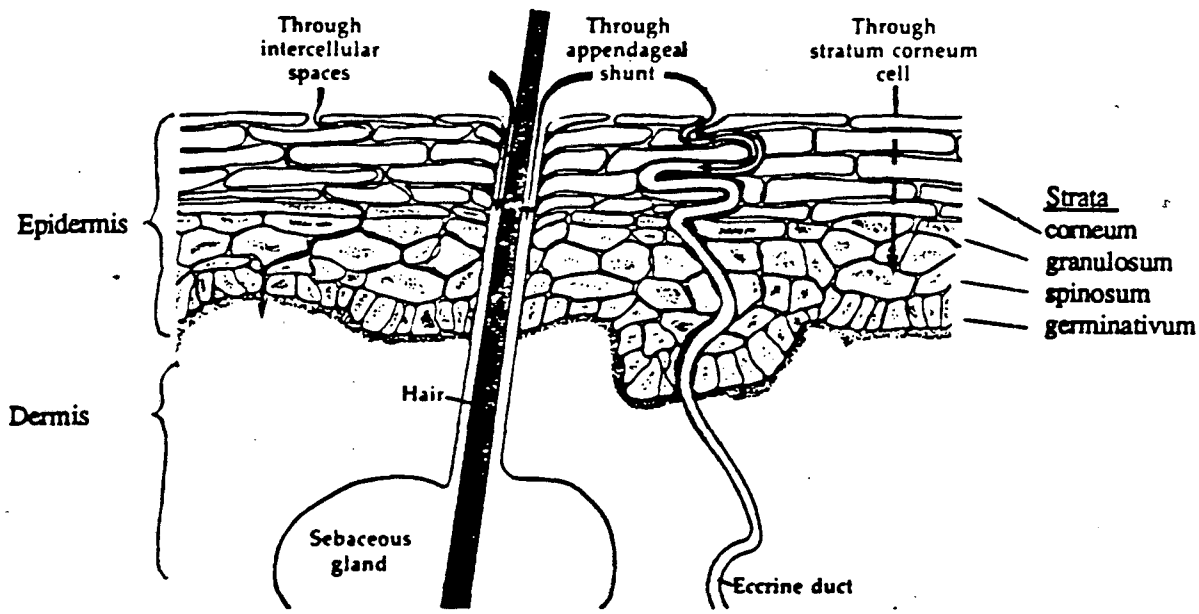

Figure 1: *Cross-sectional anatomy of non-glabrous skin showing possible transcorneal routes of water-soluable compounds.*

dermis are histologically distinct, dermal cellular and humoral factors affect the overlying epidermis, so that in some respects they behave as a single functional tissue [33].

2.2.2 Influence of skin type on potential measurements

The two basic types of skin are hirsute (hairy) skin, which covers most of the body; and glabrous (hairless) skin, which is found on the palms of the hands and the soles of the feet. The two types are very similar physiologically and structurally, but there are important differences that might affect their electrical behavior[3]:

[3]There are also differences that are unlikely to affect electrical properties, such as the dermatoglyphic patterning (eg. fingerprints) that appears only on glabrous skin.

1. Glands in glabrous skin are primarily responsive to psychic stimuli, while in hirsute skin their major function is thermoregulation. Eccrine gland activity is known to cause rapid changes in skin potential.

2. Glabrous skin has a thicker (up to 1.6 mm) epidermis than hairy skin (mean thickness = 0.1 mm). The number of cell layers may influence barrier function (Section 2.3.2).

3. Hair follicles may act as passive sources of potential (Section 2.6) [1].

The experimental measurements were made on hirsute skin because gland activity could be controlled by regulating temperature, and because the measurement technique used in this study (Section 3.2) relied upon the rapid hydration of the measurement site by the electrolyte. A thick dry layer would take longer to wet, and the extent of the conductive (wetted) area would be difficult to determine. The area of the electrode used was small enough so that the potential measurement could almost always be made without including hairs.

2.3 The epidermis and skin permeability

2.3.1 Epidermal cornification

The epidermis is divided into several strata [32] which represent successive stages in the differentiation of germinal keratinocytes to cornified keratinocytes. The lowest level of the epidermis (and the source of the overlying layers) is a single layer of keratinocytes referred to as the stratum germinativum or basal layer. As the basal keratinocytes divide, they push upwards to form the stratum spinosum, the

cells of which have a characteristic spiny appearance. The 'spines' are cytoplasmic processes which attach neighboring cells at regions of desmosomal connection [34].

The succeeding layer, the stratum granulosum, consists of flattened cells that are distinguished by keratohyalin granules and lamellar bodies in their cytoplasm. In the upper portion of this layer, contiguous plasma membranes thicken and become insoluble, and their outer surfaces are coated by neutral lipids which are discharged into the intercellular space by the lamellar bodies. The result is the formation of a barrier (described in more detail below) to the passage of water and electrolytes between the external environment and the interior of the body. The outermost layer, the stratum corneum, is composed entirely of dead anuclear cells which exfoliate as small fragments and are continually being replaced from the layers below.

2.3.2 The permeability barrier of the skin

The stratum corneum contains an efficient barrier against transcutaneous water loss, but there is disagreement as to its exact location. The predominant theory is that the entire stratum corneum is the principal barrier to absorption through the skin [35,36]. Support for this view comes from experimental evidence that transdermal penetration of various substances is impeded to approximately the same extent by both the outer and inner layers of the corneum [35]. Transcorneal movement is believed to be percellular, i.e. directly through the cell walls of the compacted corneum, rather than intercellular [37]. In accord with this concept are studies showing that the thickness of the stratum corneum is inversely proportional to its permeability [38], however other investigations have not found a relationship between the thickness of the skin and its transfer properties [39].

The opposing thesis is that there exists a gradient of barrier function in the stratum corneum, with the major permeability barrier located in its lowest level [40,41,42]. In this view, the epidermal barrier is subserved by a matrix of cells and intercellular lipids held together by strong (desmosomal) and weak (lipid) cohesive forces. Evidence for this model comes from dye and tracer [43], bio- and histochemical [40], and ultrastructural studies [44].

Formation of the barrier begins when the lamellar bodies in the keratinocytes of the uppermost granular layer move to the apical surfaces of the cells. Their limiting membranes fuse with the cell plasma membrane, and exocytosis of their lipid contents into the intercellular spaces follows. The secreted material is then rearranged in the interstices between cornified cells into many broad laminae composed primarily of neutral lipids. These laminae occlude the passage of water and provide the epidermal water barrier [40]. In other words, transport of lipid- and water-soluable compounds takes place between the cornified cells rather than through them. As the cell/lipid matrix thus formed moves towards the surface of the skin, the efficiency of the barrier is reduced due to desmosome degradation and biochemical modification of the lipids. These processes [45] ultimately result in the dyshesion and sloughing of the cells, while at the same time the barrier is constantly being renewed from below.

2.3.3 The barrier as a source of potential

Whatever its actual structure, the permeability barrier apparenly functions as a semipermeable membrane. It is generally agreed that the movement of substances

across it occurs by diffusion and is not an active process (Scheuplein in [46]). Measurements of passive potentials across synthetic membranes [47,48], simple protein films [49], membranes of polyelectrolyte composite materials [50] and lipid bilayers [51] have demonstrated that substantial (± 100 mV) voltages can be generated by permselective membranes. Although no studies of potentials across lipid-protein composites have yet been made, they almost certainly exist.

There is also evidence for a non-sudorific contribution to the transdermal potential which, while it does implicate a particular mechanism, is consistent with a permselective membrane as the generator.

- Puncture or abrasion of the skin will virtually eliminate the transdermal potential [5].

- Humans with heriditary anhidrotic ectodermal dysplasia (a genetic condition characterized by the absence of eccrine sweat glands or the presence of very few rudimentary ones) have a transdermal potential [4].

- A transdermal potential is still present in humans after sweat gland activity is abolished by sympathetic block or sympathectomy [52].

- A substantial transdermal potential is measureable after the iontophoresis of anticholinergics (such as atropine) into the skin abolishes sweat gland activity [53].

- Large transcutaneous (-28 to -30 mV) voltages have been measured in intact eccrine gland free areas (the penis and the lips) [2].

2.3.4 Sub-barrier permeability

The cell layers and tissues beneath the barrier are highly permeable. The avascular but metabolically active stratum germinativum is supplied by diffusion from the underlying dermis [33]. Moreover, subcutaneously injected tracers and dyes have been observed to percolate upward through the dermis and epidermis as far as the mid-upper stratum granulosum [54,55]. The interstitial space of the tissue layers beneath the granulosum is thus continuous with that of the underlying dermis.

2.4 Dermis and subdermis

2.4.1 Structure and function

The dermis, which is two to four mm thick, consists of comparatively non-cellular connective tissue with a variety of 'free' cells[4] scattered throughout it. The acellular components of the dermis are primarily water and collagen in a mucopolysaccharidic ground substance interspersed with elastic fibers. The dermis supports the epidermis and provides a framework for a variety of tissues and organs (such as the eccrine glands) as well as for the innervation and well-developed microcirculation that serves these structures. No blood or lymph vessels pass the dermo-epidermal boundary.

The motor innervation of skin is postganglionic autonomic sympathetic, with adrenergic components to both eccrine and apocrine sweat glands, to the smooth muscle in the walls of the arterioles, and to the arrector pili muscle of the hair. Most

[4]Macrophages, fibroblasts, mast cells, and histiocytes.

of the free (non-encapsulated) sensory nerve terminations[5] are found in the papillary layer of the dermis, but some extend into the lowest layers of the epidermis.

2.4.2 Dermal contributions to the transdermal potential

Several theories of the origin of electrodermal phenomena have suggested that dermal factors were involved. The idea that skin electrical behavior was associated with involuntary muscle activity was discredited [56] when it was shown the two did not correlate well and for lack of supportive evidence. Free nerve endings were thought to influence the skin potential, but this suggestion has been discounted since although such terminations do occasionally appear in the basal layer, generalized epidermal innervation does not occur (Sinclair in [32]). End organs in the deeper layers of the dermis are unlikely to be involved in electrodermal phenomena, since the high frequency spike potentials associated with these receptors are minute (< 50 mV) and take place in a resistive volume conductor. The same is true for potentials from the smooth muscles of the blood vessels, the myoepithelial cells of the eccrine gland secretory coil, and the piloerector muscles. Tactile receptors infiltrate the follicular canal of the hair, but there is no evidence that they can influence the skin potential difference (for example, by affecting the permeability of the canal wall) [1].

The evidence against the vascular theory, i.e. that variations in blood supply influence electrodermal phenomena, is [14] that:

- Electrodermal responses are independent of plethysmographic changes.

[5]Encapsulated organs, such as Meissner's and Pacinian corpuscles, occur only in glabrous skin.

- Engorgement of the blood vessels by a venous cuff does not result in a significant change in the skin resistance, although the changes in blood volume produced are much greater than those of vasomotor responses[6].

- Atropine iontophoresis eliminates the galvanic skin response but does not affect vasomotor responses, and vascular paralysis induced by an adrenergic blocking agent does not affect electrodermal activity.

2.5 Eccrine glands

2.5.1 Structure and function

Eccrine glands are distributed over the surface of the body (except for the oral, anal and genital surfaces) with density estimates ranging from 60 per cm^2 on the thigh to 600 per cm^2 on the soles of the feet [57,58]. The primarily function of eccrine glands in hirsute skin is the dissipation of excess heat through the evaporation of excreted water, while those on the glabrous surfaces are active in response to psychic stimuli and are not used in thermoregulation unless there is substantial thermal stress [59][7]. Thermoregulatory eccrine glands are well-developed only in the primates, but species that lack sweat glands on the general body surface and thermoregulate primarily by panting may have glands on paws or footpads.

Each gland is a single unbranched tubule which consists of two parts, a secretory coil and a reabsorptive excretory duct (only the latter is shown in Figure 1). The secretory coil is a bolus of coiled and twisted tubule 0.1-0.5 mm in diameter located

[6]This experiment was repeated by the present author measuring potential rather than resistance, with similar results.

[7]This distinction is not clear-cut, however, since the glands of the forehead and in the axillae respond to both thermal and emotional stimuli.

2-5 mm beneath the epidermis, either in the deep corium or in the subcutaneous tissue just below the corium. The secretory coil gives rise to the reabsorptive duct, which then extends through the dermis and epidermis and eventually opens onto the surface of the skin as a pore. The cells of the duct wall dedifferentiate and keratinize at the level of the stratum germinativum. The cornified duct cells can be distinguished from the rest of the stratum corneum.

Eccrine sweat glands have post-ganglionic cholinergic sympathetic innervation. Both the secretory coil and the myoepithelium are under neurogenic control[8]. Thermoregulatory sweating is controlled by the integration in the hypothalamus of afferent impulses from skin and core temperature sensors as well as input from neuromuscular components. The glands are structurally fully developed at birth, but the number of functional glands changes with influences such as climate and age.

2.5.2 Contributions to potential from non-secreting glands

Actively secreting sweat glands are known to influence the transdermal potential [4,15]. Under certain conditions, inactive glands may be sources of potential as well. The keratinized wall of the epidermal duct is impermeable to water [59] and to water-soluable tracers [Hashimoto in 46]. The duct wall in all likelihood incorporates a permeability barrier like that present elsewhere in the epidermis. A passive potential could therefore exist across the duct wall if the aqueous solutions on either side of it (for example, sweat and electrolyte) were of different concentrations. The transdermal potential difference might then bear some relation to the number of glands in the electrode area.

[8]There is some evidence for dual innervation but the reports are not consistent [59].

2.6 Hair follicles

2.6.1 Structure and function

Hair follicles are in effect pockets of epithelium that are continuous with the epidermis but extend down through the dermis into the subcutaneous tissue. The keratinaceous hair shaft is surrounded in the dermis by the external root sheath. At the surface of the skin, the root sheath is keratinized and stratified in the same fashion as the epidermis, but the outward layers thin and disappear as the sheath extends into the dermis. One to four sebaceous glands open via a short duct into the space between the root sheath and the hair. Contraction of the muscle responsible for piloerection compresses these glands and expels sebum through the duct as well as raising the hair. The oily substance secreted may have a thermoregulatory function as well as the lubrication and waterproofing of the hair and the skin.

2.6.2 Contributions to potential by the hairs

Hair follicles could contribute to the transdermal potential [2,5] in a way like that proposed for the inactive sweat glands (Section 2.5.2). The keratinized portion of the root sheath probably includes a permeability barrier, and the presence of solutions of different tonicity on either side of this barrier might generate a passive potential across it. The difficulty with this hypothesis is that the sebaceous secretions create a hydrophobic environment [60] in both the hairshaft and the glands themselves. Hair follicles are thus unlikely to affect the transdermal potential.

2.7 Additional biological sources

Additional factors which may influence the potential difference measured between the surface and the interior of the skin are

- Wounds or injuries, whether new [2,61] or in the process of healing [62].
- Warts and moles, particularly if they are associated with certain dermal carcinomas [5].
- Local deformation of the skin [16,18,19].

In the experiments described below (Section 3.6), injured skin was excluded from the sample; scars, moles and other surface features were taken into account if they were present; and the measurement technique used did not deform the skin.

2.8 The influence of regional variation in skin on electrical measurements

There is substantial regional variation in skin [34]. Even within a distinct skin area, such as the palmar surface, there are structural and functional differences; the epidermis is thick, horny and compact on the friction surfaces and is thin and pliable at the flexures. Ebling [63] has pointed out that a lack of appreciation of the extent and significance of this regional variation has led to many false generalizations, with histological or biochemical findings in one region presumed to apply to the skin as a whole. Similar assumptions have been made in dermatopharmocology and in psychophysiology with respect to the permeability and electrical behavior

of the skin, and only in recent work has the significance of regional variation been recognized (see Scheuplein in Jarrett [46], and Yamamoto [64]).

Factors that could influence the potential across healthy uninjured hirsute skin include the thickness of the epidermis (particularly the thickness of the stratum corneum and the number of cell layers in it), and the distribution of hair follicles and eccrine glands. The effects of such variables can be minimized by restricting the measurement to a small region within a superficially homogeneous area, and by testing for correlation between sweat gland (or follicle) density and the measured potential.

3 Measurement of Slowly-varying Transdermal Potentials - Materials and Methods

3.1 Summary

This chapter describes the apparatus and techniques used in these studies to measure and record transdermal potentials. Several authors have discussed the problems and techniques involved in making electrical potential measurements on the human body [12,28,61], but these are general reviews and do not specifically treat the problem of steady or slowly varying transdermal electrical potentials. Material written from the point of view of psychophysiology [4,15] does consider slow transdermal potentials but emphasizes measurements made across glabrous skin. Woodrough [1] and Foulds and Barker [3] have investigated the origin and measurement of such potentials in hirsute skin. The subjects of electrodes, instrumentation and electrical environment are considered in Cobbold [12] and in Feinberg and Fleming [28]. Ott [65] and Morrison [66] are excellent references on noise reduction and shielding techiques.

The transdermal potential measurements were made by Ag/AgCl biopotential electrodes coupled to the skin by an electrolyte isotonic with surface perspiration. One electrode was used to measure the potential at points in a grid in a small area on the back of the hand, and another monitored the variation of the potential over time at a site adjacent to the test area. The search electrode coupled to the skin through a droplet of electrolyte that was expressed at the electrode tip by a syringe micropump (Figure 2). The measurement area of this electrode was the circular

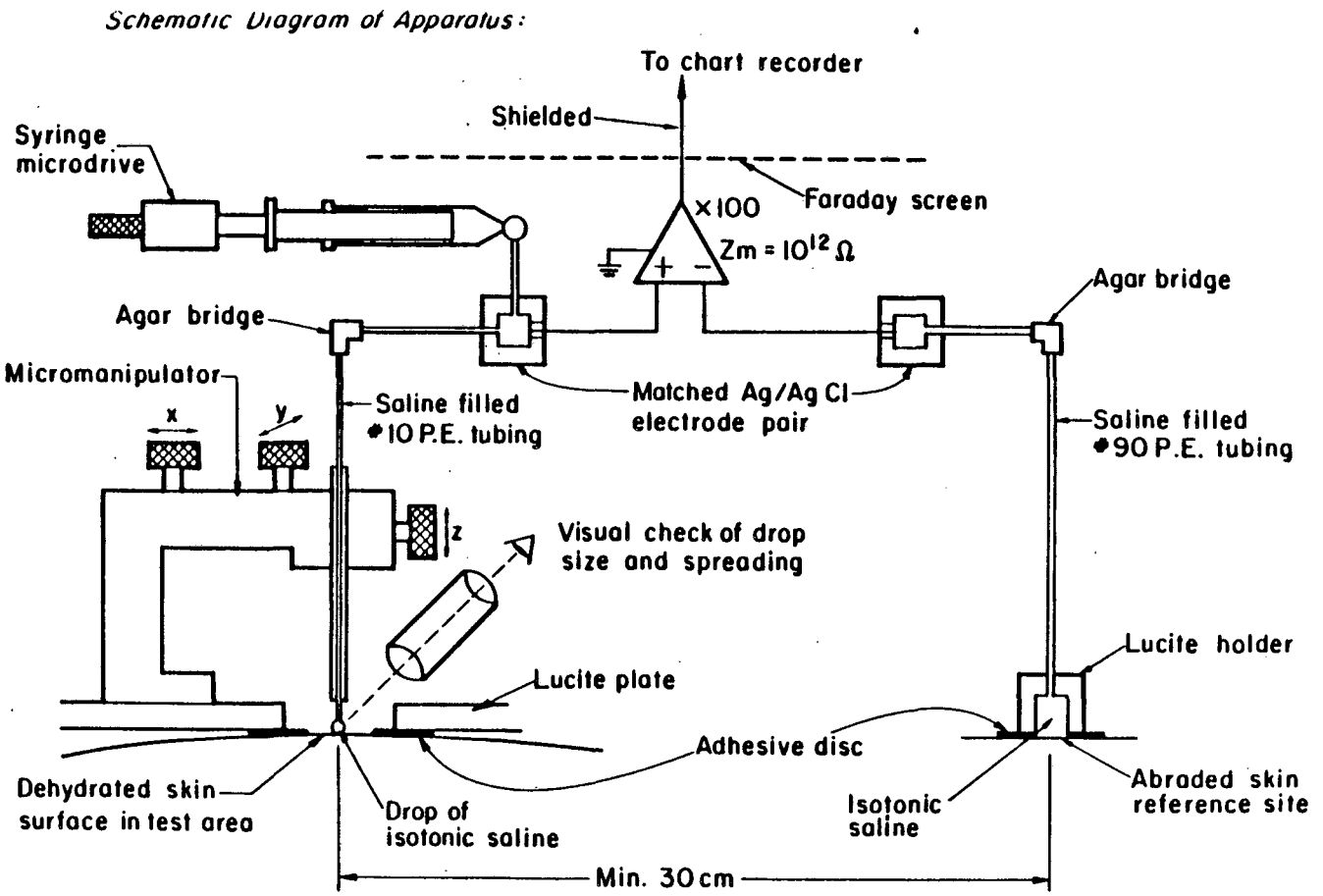

Figure 2: *Schematic diagram of experimental apparatus.*

region of hydration formed when part of the drop soaked into the dehydrated skin.

After the potential measurements were completed, pilocarpine iontophoresis was used to induce sweating, and oriented sweat gland blots were made with special paper. The gland locations were correlated with the potential measurements by means of fiducial marks. A pattern recognition program located the gland centers in a digitized image of the blot paper. In related experiments, attempts were made to eliminate emotionally-linked sweat gland activation. Cadaver skin and artificial membranes were used in these studies as models for biopotential generation.

3.2 Electrolyte, electrodes and interfaces

The electrical potential measurement apparatus (Figure 2) used a matched set of three Ag/AgCl electrodes. An agar bridge was placed between each electrode and the skin. The skin-bridge and bridge-electrode connections were made via plastic tubing filled with NaCl solution isotonic with the mean salinity of surface sweat (Section 3.2.1). Syringes on either side of each bridge were used to flush out gas bubbles. The Ag/AgCl electrodes (Section 3.2.2), differed only in the details of their connection with the skin (Sections 3.2.3 and 3.2.4) and in the addition of a syringe 'pump' to the search electrode plumbing (Section 3.2.5). The functions of the various electrodes were as follows:

- The search electrode was moved in a rectangular grid over the test area to measure the potential at each point in the grid with respect to the reference. The area of this electrode was the region hydrated by the droplet of liquid electrolyte at its tip (Section 3.2.6).

- The drift electrode measured the potential between a fixed location and the reference. This chronic record of the potential at a particular site was used to monitor for variation in the potential over time, and made it possible to distinguish mechanical artifact from such changes. (This electrode does not appear in Figure 2).

- The reference electrode provided a ground reference for the measurements.

The use of a given electrode determined the nature of its termination on the skin.

3.2.1 Electrolyte

The electrolyte used was 77 mM NaCl in water in direct contact with the skin, without a wick or an additional vehicle. Sodium chloride was used rather than KCl since it was equally compatible with the electrode material, is the major ionic component of surface perspiration [67], and because the potential arising from the different mobilities of the Na^+ and the Cl^- was much smaller than the potentials of interest. The concentration used was equivalent to the average osmolality[9] of surface perspiration. The osmolarity of each batch of electrolyte solution was tested with a freezing point depression osmometer (Fiske Model G66).

3.2.2 Fabrication and selection of electrodes

Each electrode was constructed using a waterproof high resistance epoxy (Epo-Tek 509-F, Epoxy Technology Inc; volume resistivity = 2.68×10^{14} ohm-cm) to pot a commercially sintered Ag/AgCl plug electrode (WPI type EP-2) into a lucite plug

[9]The osmolality of the post-exercise perspiration of all subjects was measured using a vapor pressure osmometer (Wescor Model 5100B). The solute content of the surface perspiration in all the individuals dropped from a high value immediately post-exercise to between 145-160 mOsm.

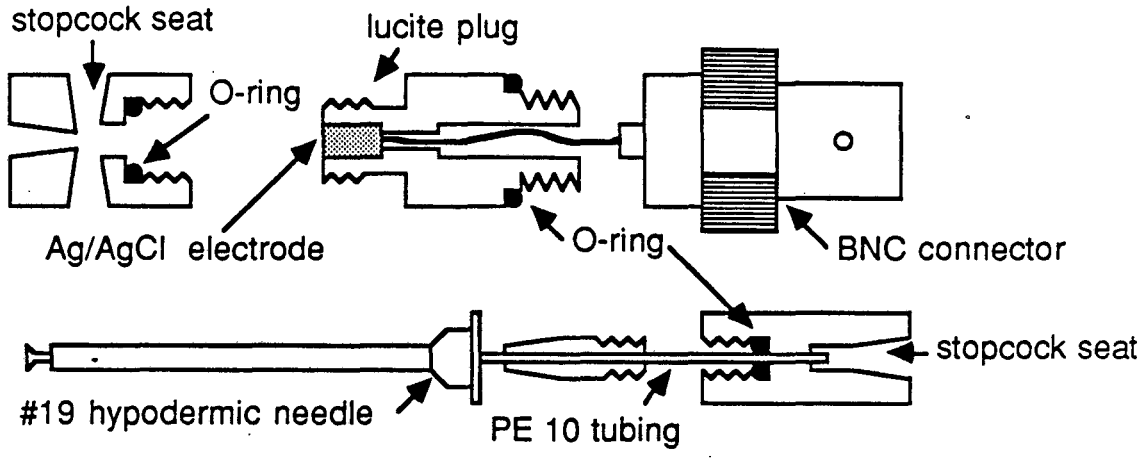

Figure 3: *Details of an electrode body and the test electrode termination.*

(Figure 3). The external electrical connection was made by a BNC male connector on the opposite end of the lucite cylinder. Ten such electrodes were constructed, and three of these that had long-term drifts of less than three mV (with no spontaneous potential changes) and offset potentials within 0.1 mV of each other were selected for use.

3.2.3 Connections from electrode to skin

The connection between an electrode and the skin was made via low-compliance plastic tubing filled with 77 mM NaCl, with a pressure-resistant agar/saline bridge (3% agar in 77 mM NaCl) inserted midway to protect the Ag/AgCl electrode from contamination. The measured bridge/electrolyte potential was stable and less than 0.1 mV in all cases.

One disadvantage of using a liquid electrolyte was that gas bubbles in the tubing changed the hydraulic capacitance of the system and interfered with the control

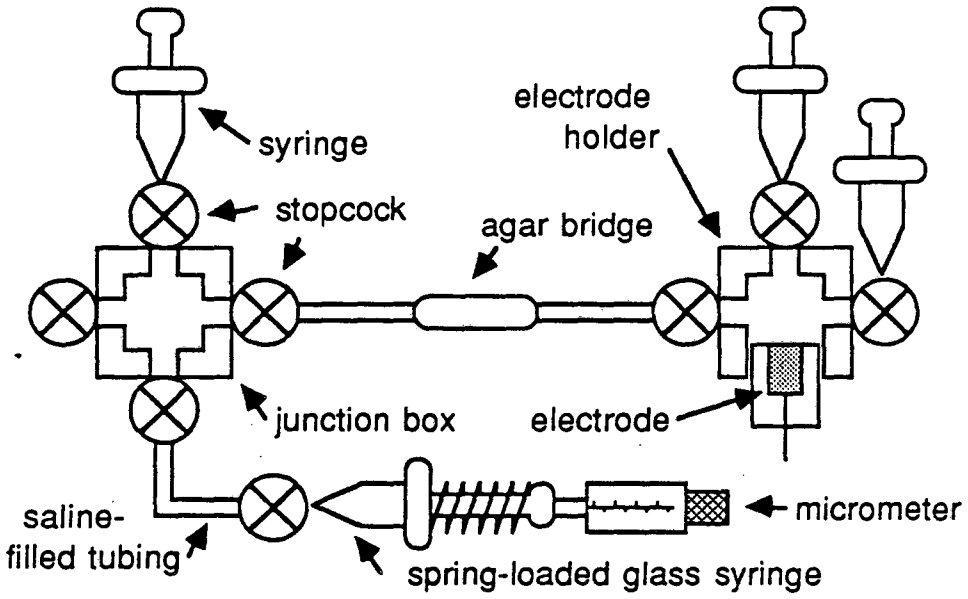

Figure 4: *Schematic of complete search electrode assembly with bridge and syringes.*

of droplet delivery size. Bubbles could also substantially increase the electrical impedance of the system by breaking electrolyte continuity. An arrangement of syringes and stopcocks on either side of the bridge was used to fill the system and flush bubbles from it (Figure 4).

3.2.4 Electrode terminations

The reference electrode tubing attached to a small lucite 'hat' which was sealed to the skin with a Beckman adhesive disc (#650454). The drift electrode line was attached to the top sandwich plate (Figure 5) at a point next to the test area. Electrical contact with the skin was established by filling the hole/hat with electrolyte and attaching the tube.

The search electrode had a more complex termination (Figure 3). The large

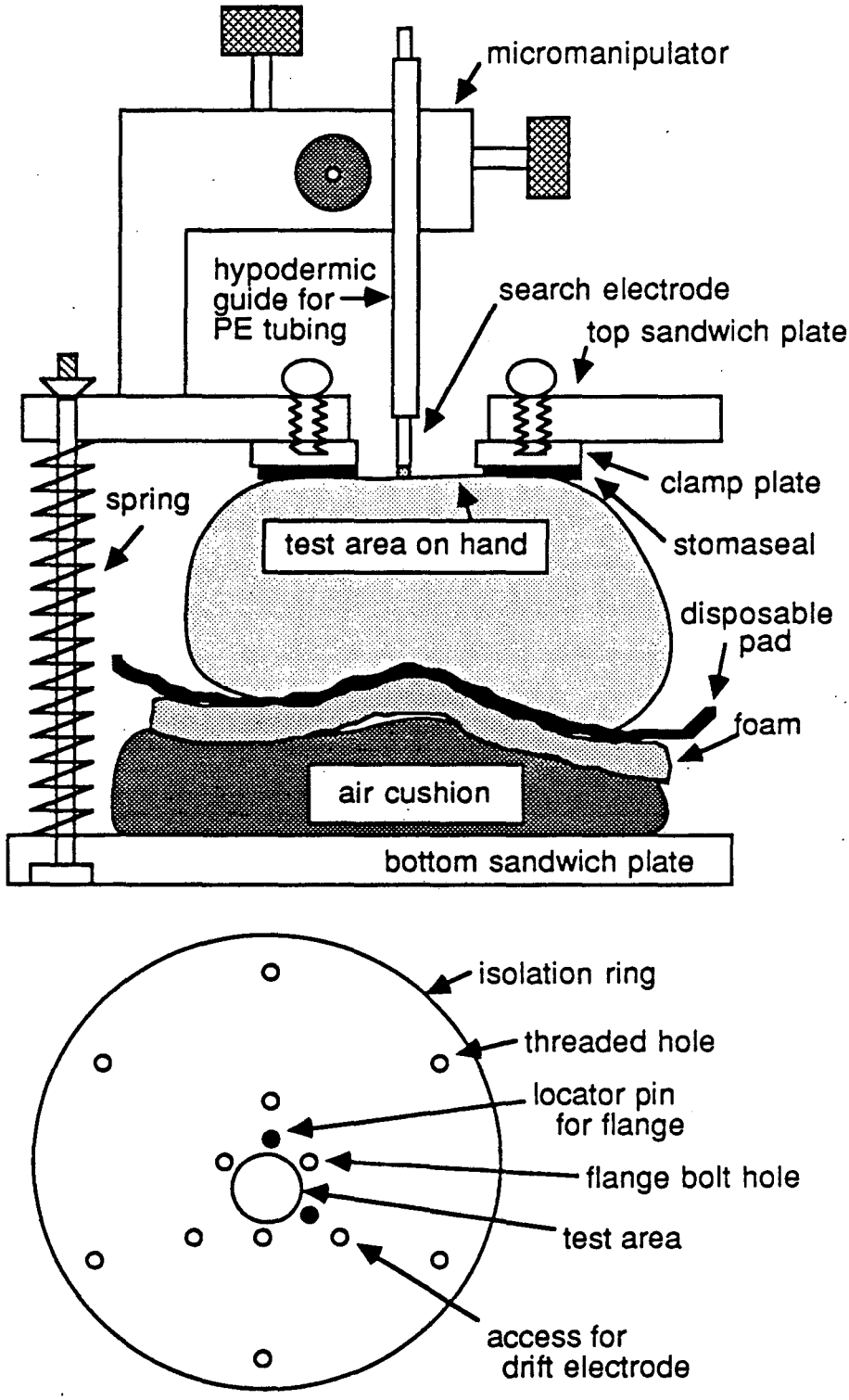

Figure 5: *Sandwich apparatus and detail of isolation ring.*

bore tubing coming from the bridge was connected to a length of PE10 tubing (id=0.279 mm, od=0.610 mm, Intramedic), with skin contact taking place at the end of the PE10. The PE 10 line was stabilized by threading it through a flat-tipped #19 hypodermic needle. Electrical contact was made with the skin through a droplet of electrolyte elaborated at its end (Figure 5). This end of the tubing was carefully heat-flared so that it resembled an inverted cup; the shape ensured that the droplet would remain at the end of the tube rather than climbing up its side.

3.2.5 Syringe micropump for search electrode

A syringe micropump was used to form electrolyte droplets of reproducible volume at the tip of the search electrode. The spring-loaded plunger of a glass[10] syringe (1/2 cc tuberculin, B-D #2002) was driven by a micrometer head (1/2" drive, 0.001"/division, Mitutogo) mounted in the same rigid frame. This arrangement was used to meter the size of the drop delivered at the tip of the PE10 tubing, and thus to control the effective area of the electrode.

3.2.6 Measurement of electrode area in the dehydrated skin

The effective area of the search electrode was the circular area hydrated by the electrolyte droplet, which was readily distinguished as a dark region in the whitened dehydrated skin. This area was quantified in two ways. The reticule in a binocular microscope was used to determine the diameter of the circular area hydrated by saline droplets (of the same size used in the experiments) which were allowed to soak

[10]The syringe must be glass. The barrel of a plastic syringe tapers slightly, so that the droplet size for a given micrometer advance is not constant, being smaller at the end of the plunger's travel than at its start. The same is not true for the fitted ground glass plunger travelling in its cylindrical bore.

into alcohol-dehydrated skin. The results from these measurements were compared to the diameters of fluorescein-water droplets of the same volume measured using the reticule and a UV source (UVSL-25 Mineralight, Ultra-violet Products). The average diameter in both cases was 2.0±0.1 mm, with an intersubject variation of approximately ±0.1 mm.

This technique relies upon the observation that after the initial spread of the electrolyte droplet into the skin, the size of the hydrated area changes very slowly (unless additional electrolyte is added to it). Even so, total measurement time at any one point was limited to 30 seconds to minimize the effect of any such lateral diffusion. If the measurement was repeated, the area was first dehydrated again. To prevent coupling between adjacent hydrated areas, drop separation was kept to three mm.

Initial tests established that the electrolyte droplet had to have a volume of approximately 2 μl to establish a stable connection; smaller droplets would adsorb quickly into the skin and break the connection at the tip. If the droplet was too large (greater than about 9 μl), it could slip over the skin surface away from the electrode tip, and the tip would not be at the center of the hydrated area. A volume of 5 μl, which corresponded to 0.0762 mm of syringe plunger travel (i.e. three divisions on the micrometer scale), was chosen to make the measurements.

3.2.7 Stabilization of interfaces

The charge double layer at the surface of any electrode behaves as a capacitance, and a mechanical disturbance of this layer changes the measured potential. The saline-filled tubes of this apparatus were susceptible to 'catheter whip', rapid

high pressure transients that occur if a tube is rapidly moved in a direction normal to its long axis. The possibility of catheter whip was minimized by securing the electrode assemblies in a rigid frame which in turn was clamped to the apparatus holding the test area in place. Motion of the search electrode tip within the electrolyte drop did not have a measureable effect on the potential unless the tip touched the skin surface; nor did the reduction of drop size as it soaked into the skin until just prior to complete loss of contact. A binocular microscope was used to check the size of the expressed search electrolyte drop, the extent of its spread on the skin surface, and the relation of the tip to the skin during the experiment. The drift and reference electrodes used sealed interfaces, and were not subject to similar problems.

3.2.8 Maintenance of electrodes and electrode apparatus

Between experiments, the three electrodes were shorted together and their saline line terminations were sealed in a jar filled with 77 mM saline. Electrode offsets were recorded at the start of each experiment, and drift was checked biweekly. Electrodes which developed unacceptable offsets (>0.5 mV) or large drifts (>3 mV/24 hrs) were cleaned or replaced. The saline filled lines leading to the skin were flushed after each experiment, and the saline in the storage jar changed weekly.

3.3 Spatial positioning references

Since the search electrode was not attached to the skin, it was essential that it remain fixed in the same frame of reference as the test area so that any (x, y) point could be reproducibly located during an experiment (Section 3.3.1). There

also had to be a means to register the locations of the measured potentials with the locations of sweat glands, hair follicles etc. in order to correlate one with the other (Section 3.3.2).

3.3.1 Establishment of a common fixed reference frame

As discussed in Section 3.9, the region chosen for measurement was an area on the back of the hand which was held in place by sandwiching it between two lucite plates (Figure 5). A large adhesive ring (Stomaseal hypoallergenic adhesive discs #1500, hole diameter=3.18 cm, outer diameter=10 cm, 3M) held the skin around the test area to the isolation ring, a disc of lucite (od=18.6 cm, id=3.6 cm off-center) that attached under the top sandwich plate. A micromanipulator (MW, X= -1 to +26 mm, Y= -3 to +23 mm, Z= 0 to +42 mm) that held the search electrode was attached to the top plate as well. The search electrode and the test area were thus in the same fixed reference frame and the electrode tip could be reproducibly positioned at any point on the skin. The subject's hand was supported by an inflatable cushion. Also attached to the top plate but not shown in Figure 5 were the binocular microscope and the electrode assembly.

3.3.2 Establishing correspondence between measures in the same area

Three ink fiducial marks were used to establish the relation between the map of the transdermal potential and the locations of sweat gland pores. The locations of the marks were determined by holes in a lucite piston that was oriented with respect to the skin by a key and slot arrangement. A matching set of holes in a slotted jig was used to locate the marks on special eccrine gland imaging paper so

that the marks on the paper were in the same locations as those on the skin.

Figure 6 illustrates the apparatus used to do this. A slotted stainless steel flange (B) was snapped over two locating pins on the isolation ring (A) and bolted down. When the key of the lucite piston (D) was correctly oriented, the piston slipped down inside the flange so that its bottom rested on the surface of the skin. With the key in the slot, the piston was prevented from rotating in place. A fine-point marker pen was then inserted in each of three vertical holes in the piston to mark the skin surface. The flange and the piston were removed, and the location of the ink marks on the skin was determined with the tip of the search electrode. The locations of visible anatomic features (moles, scars, etc.) were noted at the same time.

Eccrine gland imaging is discussed in Section 3.5. Briefly, a surface sweat droplet blotted onto special paper made a colored dot that thereby located the secreting gland. For the gland images to register with the potentials measured in the region, the fiducial marks on the imaging paper had to match those on the skin. To accomplish this, a bezel ring (C) was used to clip a disc of the special blotting paper to the skin side of the three-holed lucite piston (D). The piston with the paper clipped to it was then inserted into a jig (E) that consisted of a duplicate of flange (B) and a lucite rod with three holes through it that exactly matched those in the piston. These holes guided the pen to mark the front (skin side) of the paper with a mirror image of the fiducial marks on the skin. When the lucite piston (D) was inserted into the flange (B), the marks on the face of the paper registered with those on the skin.

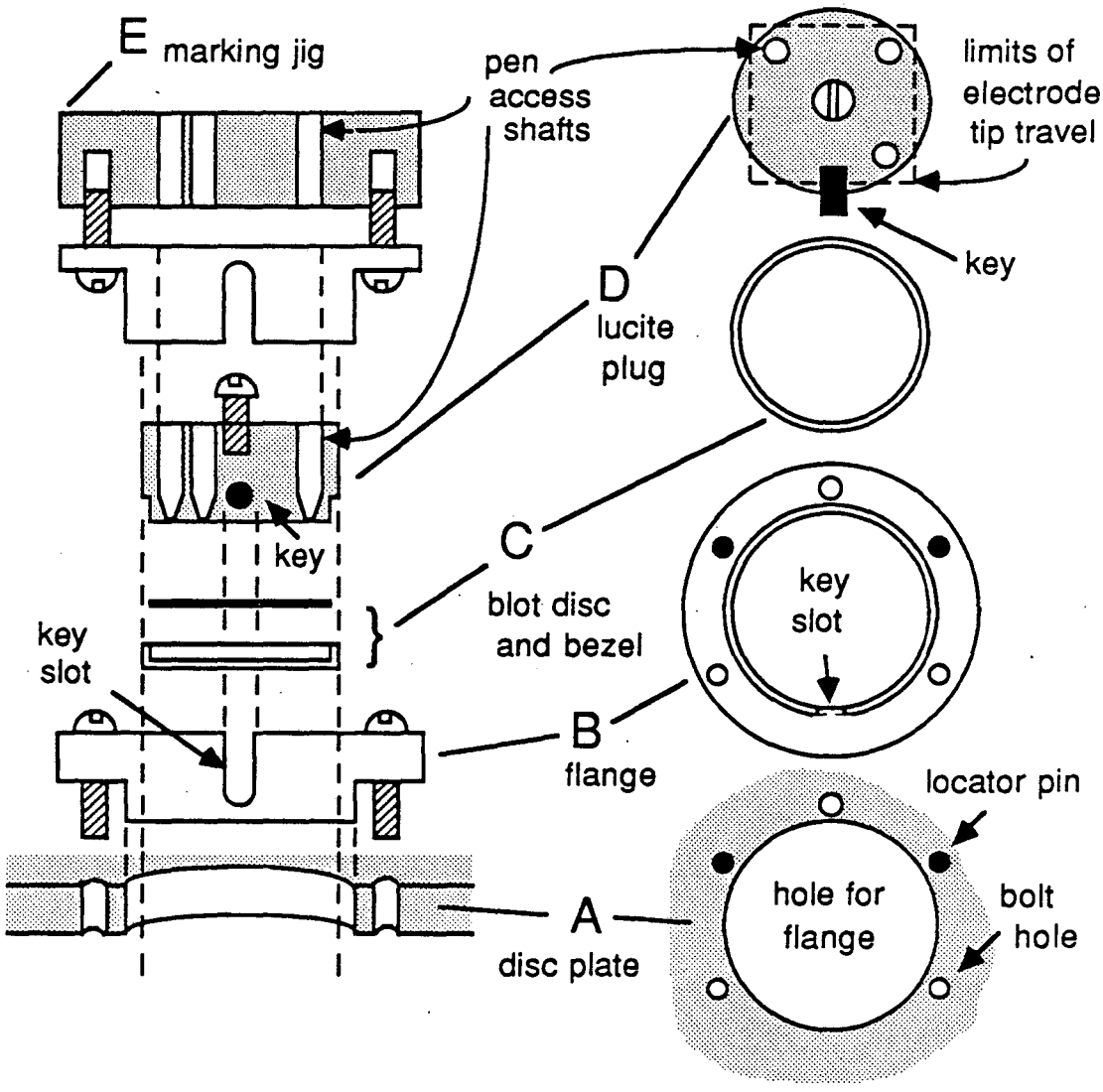

Figure 6: *Flange, lucite piston and marking jig for fiducial marks.*

3.4 Amplification, recording and electrical environment

The high impedance of the electrode assembly (Section 3.4.1) required the use of a pre-amplifier with a very high input impedance (Section 3.4.2). A chart recorder outside the shield was used to make a permanent output record (Section 3.4.3). Electromagnetic interference present in the unmodified experimental chamber was reduced by moving and shielding sources, but the voltage sensitivity of the electrode apparatus made the construction of a Faraday shield necessary (Section 3.4.4). A signal ground was established with a ground rod, and a low-frequency ground tree was constructed (Section 3.4.5).

3.4.1 Determination of source resistance

The resistance of hydrated skin is in the range 20-40 KΩ, and Ag/AgCl electrode impedance at low frequencies is an order of magnitude lower. The high volume resistivity of 77 mM NaCl (125 Ω-cm) and the distance between the Ag/AgCl electrode and the skin meant that the major contribution to circuit impedance came from the electrolyte-filled lines. A calculation of the search electrode resistance showed that the small diameter PE 10 tubing contributed approximately 2.24 MΩ while the polyvinyl tubing in the rest of the system (which is five times longer, but has a bore ten times larger) added 0.15 MΩ for a total of 2.39 MΩ. The measured DC resistance of the search electrode was 2.5 MΩ, while thta of the large-bore line between the drift and reference electrodes was 0.5-0.7 MΩ.

3.4.2 Preamplifier circuit

Drift and search preamplification circuits were identical. Each used a National Semiconductor LF352D FET instrumentation amplifier (input impedance $Z = 2x10^{12}\Omega$) configured in its 'typical' circuit (Figure 7) for a gain of 100x. The high input impedance minimized gain error and current flow through the electrode. A large input offset voltage temperature coefficient (10 μV/°C) indicated temperature sensitivity, but after the circuit enclosure was sealed and insulated, a heat gun directed at the box did not affect the measured potential. A PNP transistor was connected across the output (as shown in Figure 7) to suppress switching transients. Power for the preamplifier was provided by a series-parallel arrangement of mercury cells (Everyready E146X, 8.4 V/cell) that provided ±16.8 V (maximum supply voltage = ±18 V). Wire runs and component leads in the circuit were kept as short as possible.

3.4.3 Signal flow, final amplification and recording

Amplified drift and search potentials were carried through the Faraday cage to the chart recorder by shielded BNC cables. A two channel ink pen recorder with 0.1 inch/mV resolution (HP 7100B Strip Chart Recorder, with Model 17501A plug-in amplifiers) was used to record the potentials. The recorder was visible through a small lucite window in the Faraday cage wall, and was operated from inside the chamber by mechanical linkages through the window.

The intrinsic noise of the system in the shielded environment with the inputs shorted was less than 10μV in the range 0-100 Hz. Noise in a test configuration, with search and reference electrodes shorted in the saline phantom, was less than

Instrumentation Amplifiers

LF152/LF252/LF352 FET input instrumentation amplifier

general description

The LF152 series is the first monolithic JFET input instrumentation amplifier. The well-matched high voltage JFET input devices provide very high input impedance and extremely low bias currents, making the LF152 ideal in applications where high source impedances are encountered.

The LF152 very accurately amplifies a differential input signal and rejects common-mode signal and noise. It is not an op amp, but operates with an internal closed loop gain connection which allows good linearity with no external feedback. The LF152 eliminates the need for extremely precise resistor matching to obtain high common-mode rejection (CMR) and provides high input impedance as compared to the use of conventional op amps connected as a difference amplifier.

The LF152 utilizes internal differential current feedback eliminating the need for precision external feedback components. The amplifier gain can be easily adjusted from 1 to 1000 by changing the value of a single resistor. The transfer function for the LF152 is highly accurate because it has a very low initial gain error and non-linearity. The bandwidth and slew rate are externally controlled and the sense input and device output are pinned out separately for added versatility.

features

- JFET inputs
- High input impedance — $2 \times 10^{12}\Omega$
- Low bias currents — 3 pA
- Low noise currents — 0.01 pA rms
- Low gain nonlinearity — 0.02%
- High common-mode rejection ratio (G = 100) — 110 dB min
- Single resistor gain adjust
- External compensation for extended gain and frequency ranges
- Both input and output offset adjust capability to allow a change of gain without rezeroing
- Low supply current — 1 mA

connection diagram

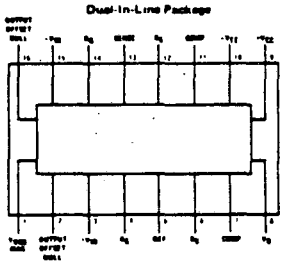

Order Number LF152D, LF252D or LF352D
See Package 26

simplified schematic

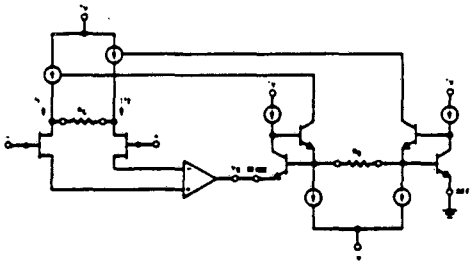

FIGURE 1

typical circuit

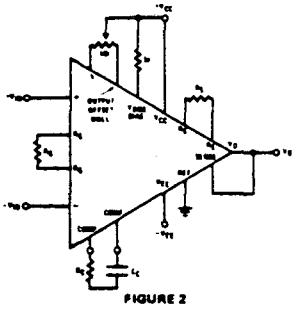

FIGURE 2

Figure 7: *Data sheet for LF352D instrumentation amplifier. (Component values used in the 'typical' circuit above were R_c=160 Ω, C_c=0.002 μF, R_g=10 KΩ and R_s=1 MΩ).*

Reprinted with permission of National Semiconductor Corporation.

0.3 mV peak-to-peak. Since the 3dB point for the recorder was approximately 20 Hz, additional output filtering was unneccessary.

3.4.4 Reduction of noise and interference

Unshielded high impedances and irreducible loop areas in the electrode plumbing made the construction of an electrostatic shield (a Faraday cage) necessary to avoid saturating the amplifier. The cage was constructed of copper screen (#30 mesh, square weave, commercially pure copper) connected at seams, edges and discontinuities with rosin core solder. When the shield was grounded, ambient RF was greatly reduced and the 60 Hz almost entirely disappeared[11]. Illumination inside the cage was provided by DC lamps.

3.4.5 Establishment of earth ground

The local AC power ground carried 20 mV with respect to true ground and was thus unacceptable as a signal ground. A copper ground rod surrounded with copper sulfate and sand was used to establish an electrically quiet contact to the earth outside the laboratory. The end of a 3-cm wide ground strap soldered to the rod was the base of the signal ground tree. The Faraday cage, signal ground and chart recorder were connected at this point with braided shield.

[11]The frequency f_c at which a rectangular waveguide becomes an attenuator is $f_c(Hz) = 1.5 \cdot 10^{10}/l$, where l is the largest dimension of the waveguide cross-section in cm [65]. The diagonal measure of #30 mesh is 0.09 cm, and thus this shield had a predicted $f_c = 1.67 \cdot 10^{11}$ Hz. The two signal cables were led out through a copper pipe (14 cm long, inner diameter 2.54 cm) soldered to the wall screen. For a round waveguide, $f_c(Hz) = 1.75 \cdot 10^{10}/d$, where d is the diameter in cm, so that $f_c = 6.9 \cdot 10^9$ Hz for the waveguide.

3.5 Eccrine gland imaging

3.5.1 Print method of pore location

The method used to locate eccrine gland pores on the skin surface was a modification of the starch-iodine technique developed by Dole and Thaysen [68]. Paper with a thin layer of iodine on its surface adsorbs water and shows the wetted area by a sharply defined blue dot. The dot is formed because certain types of paper are impregnated with starch during their manufacture, and when the watery sweat solubilizes the starch, a starch-iodine reaction takes place. The technique requires a paper of uniform texture that adsorbs iodine evenly across its surface. Iodine was applied to white 20# bond by vacuum sublimation until the paper was a light brown (large variations in the amount of iodine deposited do not affect the sensitivity of the method [68]). Circular discs (diameter = 3.0 cm) were punched from this sheet and stored in an airtight jar.

To make an eccrine gland image, a disc of this paper was clipped by the bezel ring ('C' in Figure 6) to the end of the lucite piston and marked with fiducials as described in Section 3.3.2. The test area (which had been treated with pilocarpine to induce sweating, Section 3.5.2) was wiped dry, and the piston was inserted into the slotted flange in the isolation ring and pressed onto the skin. Once the gland print was formed, the piston was withdrawn and the imprinted disc was removed and labelled. The slot and key arrangement ensured that each disc was oriented in the same way relative to the skin. Prints were made until four complete and clear images had been obtained. Successive prints from the same area had 96% of their gland images in common. Those gland images that were in one image and not

the other appeared to be uniformly distributed over the surface of the blots. After the gland imaging was completed, the unreacted iodine was allowed to evaporate, leaving blue dots on a cream-colored field.

3.5.2 Pilocarpine iontophoresis

Pilocarpine, a parasympathomimetic that is particularly effective on eccrine sweat glands, was used to induce non-thermal sweating in the test area prior to the gland imaging[12]. Iontophoresis was used rather than injection because it applied the drug uniformly over the area. Stainless steel EKG disc electrodes (diameter = 1 inch) were connected to a constant current source with a saline-soaked gauze between the indifferent electrode and the skin. The subject adjusted the current to a comfortable level between 2.4 and 4.9 mA, and the procedure lasted five minutes.

3.5.3 Location of gland centers

Digitized images of gland prints 512 pixels square were made using a Hamamatsu C1000 video scanning system, with the camera aperture adjusted for maximum image dynamic range. Each array line represented the average of 10 scans. The calibration image (made at the same time) was of a sheet of graph paper.

The analysis of each such image took place as follows. The coordinates of the fiducial marks in the digitized image were established using a bitpad (Summagraphics Bitpad 1). Gland centers in that image were then located with a memory-conservative boundary continuation algorithm [70]. After a narrow window was

[12]The maximum dose applied was 10.0 mg as 5.0 cc of 0.2% water solution on a gauze pad, where the dose recommended for sweat induction is 10 to 15 mg [69]. The protocol for this procedure was adapted from that used by Children's Hospital, Oakland, in the sweat test for cystic fibrosis.

applied to the image to establish sharp object edges, the analysis proceeded one scan line at a time, using information from the previous scan line to determine whether an object (i.e. a pair of edges) was continuing, terminating, merging with another object, or being created[13]. A running account was kept of the perimeter (P), area (A), and location ('center of mass') of each object. Object i was considered to be non-circular if the ratio P_i^2/A_i was greater than 4π. The algorithm was implemented in Fortran[14] on a PDP 11/44 with 1792 Kbytes memory. A DeAnza Systems model ID2000 was used for display.

The results of this processing were evaluated with a second set of routines. The digitized image was re-displayed and the objects detected by the initial analysis were marked as circular (green) or non-circular (red). The bitpad was used to separate merged glands and other non-circular objects and to locate those glands that had been windowed out of the image in the initial analysis. The criterion used

[13]For example, (referring to the diagram below)

$$\begin{array}{lccccc} scanline(k-1) & x_{R_{j-1}} & x_{L_j} & x_{R_j} & x_{L_{j+1}} \\ & & \downarrow & \downarrow & \\ scanline(k) & x_{R_{i-1}} & x_{L_i} & x_{R_i} & x_{L_{i+1}} \end{array}$$

if the ith pair of edges on scan line k are $x_{L_i}(k)$ and $x_{R_i}(k)$, then for the left boundary at $x_{L_j}(k-1)$ to continue to $x_{L_i}(k)$, it must satisfy the conditions

$$x_{R_{i-1}}(k) < x_{L_j}(k-1) < x_{R_i}(k)$$

$$x_{R_{j-1}}(k-1) < x_{L_i}(k) < x_{R_j}(k-1)$$

Similarly, for the right boundary,

$$x_{L_i}(k) < x_{R_j}(k-1) < x_{L_{i+1}}(k)$$

$$x_{L_j}(k-1) < x_{R_i}(k) < x_{L_{j+1}}(k-1)$$

[14]The pattern-recognition subroutine used was a modification of a colony-counting program obtained from Michael Yezzi of Lawrence Berkeley Laboratory.

to distinguish two adjacent gland blots from a single large blot was a minimum center-to-center separation of 0.166 mm (three pixels). The procedure of separation and identification was aided by the examination of the original blot disc with a binocular microscope. When all gland centers had been identified, the number of glands within a particular radius of each potential measurement site could be determined.

3.6 Summary of study protocols

3.6.1 Selection of subjects

Experimental subjects were selected from a group of 17 volunteers. Participation was determined on the basis of

- A short medical history which focused on physical conditions, medications and habits that might affect skin electrical potential.
- An examination for angle closure glaucoma[15].
- Their performance in a trial of the procedures used.
- Their willingness to participate after undergoing a screening interview and the experimental trial.

Eight volunteers were excused from the study because of difficulty (such as excessively dry skin or a drug reaction) with one or more of the experimental procedures. Sixteen sets of useable data (out of a total of 36 studies attempted) were obtained

[15]Individuals with this condition were at risk for a dangerous rise in intraocular pressure if an experimental procedure involving the transdermal ionphoresis of atropine sulfate was performed [69]. The condition was absent in all subjects.

from six subjects. An informed consent (approved by the appropriate Human Use Committees) and an update of the medical history were obtained before each study.

3.6.2 Preparation of skin for in-vivo potential measurement

Standard psychophysiological protocols were used in the preparation of the skin for measurement [56]. A reference site was chosen at least 10 cm from the test area so that no current path between it and the drift or search electrode was possible. Test and reference areas were cleaned with soap and water, and the reference area was shaved (the test area had been shaved not less than ten days prior to the study date). Isopropyl alcohol (100%) was applied to both areas to remove surface debris, dehydrate the stratum corneum, and prevent infection at the reference site. A 3/16" diameter bleb of skin at the reference site was abraded with #600 carbide paper [71] until the subject reported a prickling sensation, indicating that an innervated layer had been reached[16]. The 'hat' of the reference termination was centered over the abraded area and attached to the skin by an adhesive ring (see Section 3.2.4).

The isolation ring with its adhesive ring were applied to the test area with the slotted flange in place (see Figure 3.3.2). The fiducial locating piston (sans blotting paper) was inserted into the flange and the fiducial marks were made on the skin surface. The flange was removed and the subject seated inside the Faraday cage. The isolation ring was then bolted into place beneath the top sandwich plate (Figure 5) and the drift and reference electrode lines were attached as previously described (Section 3.2.4).

[16]The equivalence of this reference to one made by inserting a saline-filled hypodermic needle through the skin [1] was verified separately.

3.6.3 Potential measurement and gland location

A study began with a calibration check of the chart recorder and preamplifier. Bubbles were flushed from the electrode plumbing, and the electrode drift, offset and impedance were recorded. After the subject was in place, the x, y coordinates of the fiducial marks (and other visible features such as moles, scars, etc.) were established with the dry tip of the search electrode. The first row of measurements in the search grid was used as a test row to verify equipment operation and to evaluate movement and other artifacts.

The procedure for the measurement of each row was as follows:

- The entire test area was swabbed with alcohol and allowed to dry.
- The micromanipulator moved the search electrode tip to the desired location, and the tip was lowered to just above the skin.
- An electrolyte droplet was expressed at the tip by the syringe pump. Droplet formation and coupling to the skin were observed with a dissecting microscope.
- The (x, y) location of the drop was recorded and the stable potential level measured for for 15 to 20 seconds. The drift potential was measured at the same time.
- The tip of the electrode was moved up and away from the skin, and the remaining electrolyte was removed with a Q-tip.

The interpoint and inter-row separation in the measurement grid was 3 mm. Since the skin occluded by the adhesive ring that held the test area in place rehydrated

rapidly, no measurement was made less than one mm away from the edge of the ring.

At the conclusion of the potential measurements, the drift and reference saline lines were removed, and the isolation ring and reference 'hat' were left in place on the skin. Photographs of the test area, its location on the hand, and the location of the reference 'hat' on the forearm were made with a Polaroid copy camera (MP-4) equipped with macro (50 mm) and standard (105 mm) lenses. A disc of lucite was bolted to the isolation ring to flatten the skin in the test area, and a Wratten #4 filter was used to increase contrast. Pilocarpine iontophoresis was followed by gland printing, and electrode drift and offset were recorded to complete the study.

3.7 Attempts to constrain the in-vivo system

Despite the habituation of the subjects to the experimental procedures, several studies were terminated prematurely when time variation of the drift potential indicated psychologically-related gland activity in the subject. Several techniques were used to eliminate the involvement of the sweat glands:

- The subject's hand was chilled in an ice water bath prior to the measurement. This procedure was discarded because of the discomfort to the subjects involved.

- Iontophoresis of the anticholinergic atropine was used to inactivate the sweat glands[17] in the test area. The skin there became reddened, wet and hot, and subjects reported dryness of mouth and a rapid heart rate. This procedure was

[17]The maximum dose was 0.5 mg, as 5.0 cc of 0.01% solution. The average clinical dose is 0.4 to 0.6 mg [69].

abandoned because of concern about the side effects as well as the possibility of damage to the skin secondary to the iontophoretic current.

- A solution of aluminum chloride[18], a powerful antiperspirant [72,73], was applied in an occlusive dressing to the prospective measurement area overnight [74]. The antiperspirant effect takes place because the chemical diffuses into the sweat gland duct and forms an obstructive hydroxide gel *in situ*. The treated area became dry and leathery and remained so for up to two weeks, during which time thermal sweating could not be induced. Potential measurements in the region were difficult to make because of the extreme dryness of the stratum corneum; 25 to 40 μl of electrolyte could soak into the surface at a given point before a stable connection was formed. In addition, lateral diffusion was visibly anisotropic and the effective electrode area differed from one point to the next. In other words, while the application of antiperspirant was effective in the blockage of the sweat glands, it led to a condition that interfered with this particular potential measurement technique. The magnitude of the transdermal potential was about one-third that of the unperturbed skin, which suggested that aluminum complex sorbed to the stratum corneum [75] may also have affected the measurement.

[18]Aluminum chloride hexahydrate, 20% in anhydrous ethyl alcohol, tradename Drysol, Person and Covey, Inc.

3.8 Physical and biological model systems for skin electrical behavior

3.8.1 In-vitro human skin as a model membrane

Full thickness sections of autopsy skin were obtained from the chest area of fresh cadavers[19]:

- The skin was soaked with Betadine, shaved, rinsed and dried.
- The area to be harvested was dehydrated with alcohol and a lucite washer (id=2.5 cm, o.d.=3.5 cm, thickness=3 mm) was attached to it with an adhesive ring to prevent the sample from shrinking and curling after detachment.
- The skin (thickness 4-12 mm) under the washer was removed.
- The sample was rinsed twice with saline and put into a labelled jar filled with sterile skin culture medium[20].

The jar was refrigerated, and the sample was used within four hours of acquisition.

The skin sample was maintained under tissue culture conditions during the potential measurement procedures. A second adhesive washer mounted the sample ring under a hole in the cover of X-ray sterilized petri dish (Figure 8). With the bottom of the sample immersed in culture medium, the sample was warmed to 37°C and the dish was set into a temperature-controlled water bath under the top

[19]Skin samples were obtained through the courtesy of the Autopsy Unit, Pacific Medical Center/Presbyterian Hospital, San Francisco. The procurement procedure was adapted from the Skin Unit protocol of the Northern California Transplant Bank.

[20]Dulbecco's modified Eagle medium, with *l*-glutamine, HEPES buffer, *d*-Glucose, sodium pyruvate, penicillin (250 units/ml) and streptomycin (250 μgms/ml) added.

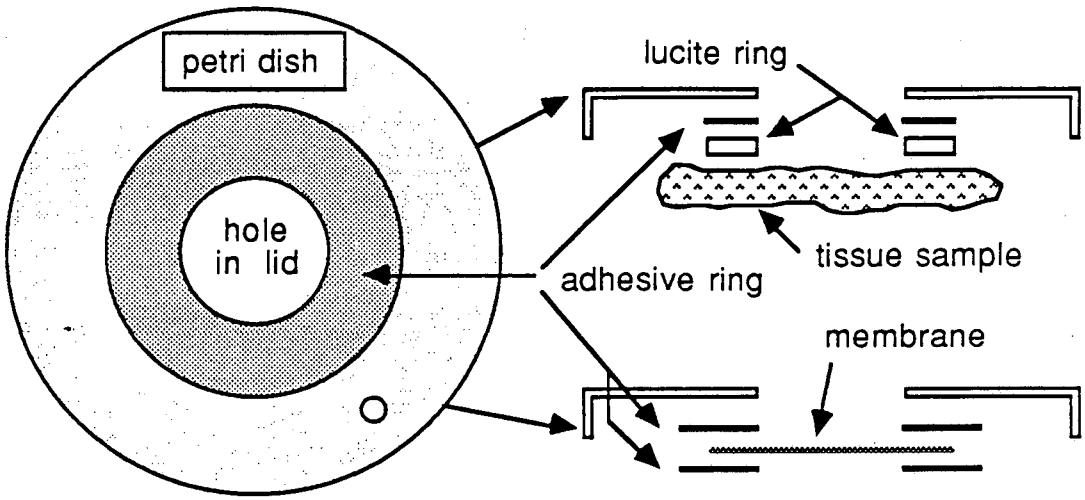

Figure 8: *Top and two side views of the holed petri dish lid used to mount the model membranes.*

sandwich plate. The electrical connection and use of the search electrode were the same as for the in-vivo case. An agar/saline bridge between the culture medium and the reference electrode line completed the circuit (there was no drift electrode).

The electrical potential of this preparation was unstable in all cases, with a rate of potential change of up to 5 mV/minute. Measured potentials ranged from -25 to -47 mV, and were subject to sudden jumps as well as slow fluctuations. Changing the thickness of subcutaneous fat removed with the sample and the depth of medium in the dish had no apparent effect on the variations, and they persisted in well-equilibrated preparations. The medium was stirred to prevent formation of concentration gradients and their associated diffusion potentials.

Possible sources of this instability were

- Potentials due to tissue trauma, i.e. 'injury potentials' [61].
- A skin 'battery' driving a current that may be involved in wound healing in-vivo [3,62,76].
- Changes in current paths as the ionic medium diffuses through the tissue.

While adjacent points could have different potentials, the instability of the measurements made it impossible to reliably distinguish spatial variation within the temporal variation.

Split skin samples[21] were also evaluated as a potential model, again without satisfactory results. Samples of dermatomed skin (dimensions = 4 cm x 10 cm x 0.3 mm) on a nylon mesh backing were thawed, warmed and rinsed in saline to remove traces of mineral oil and glycerol. A four centimeter square section was mounted on a lucite washer and set into a petri dish filled with liquid culture medium just as the full thickness skin had been. However, when the medium came into contact with the sample, it immediately leaked through small holes (probably follicle openings) distributed over the surface of the preparation. The potential measured was thus the saline/medium junction potential and was not influenced directly by the structure of the skin.

3.8.2 Artificial membrane models

Dialysis tubing (flat width 7.62 mm, average pore radius 24 Å) and dried pig bladder (diameter = 3", Carolina Biological Supply) were used to test whether the thickness of a semipermeable membrane could influence the potential. Both were

[21]Split skin samples were obtained courtesy of Howard Maibach, M.D., of the Dermatology Department, UCSF.

prepared in the same way: a 7.0 cm square segment of presoaked[22] membrane was mounted in a holed petri dish lid in a manner similar to the attachment of the whole skin samples (Figure 8). In this case the membrane was fixed directly to the lid itself with a wide adhesive ring, and a second ring was applied beneath the membrane so that it was sandwiched in place with the upper surface exposed through the hole in the lid and the lower surface in contact with the bathing solution. The electrodes were attached and the potential measured as for the skin samples.

Membrane thickness for the dialysis tubing was the number of layers of tubing sandwiched together, while the pig bladder thickness varied substantially within the sample. The transmembrane potential was found to change as a function of the bathing solution, but was not affected by the thickness of the membrane. Bathing solutions used were 144 mM NaCl by itself and 144 mM NaCl with 200 mM of Dextran blue, a large branched polysaccaride that could not pass through either membrane. The potential in every case was within ± 0.2 mV of the liquid junction potential as calculated by Henderson's equation. Stirring the solution in the dish did not affect the potential.

3.9 Measurement requirements

3.9.1 Limitations on size of test area

Spatial variation in the steady transdermal potential are thought to be due to local changes in eccrine sweat gland density and/or to local variations in a non-sudorific 'epidermal' source that includes the barrier layer and the stratum corneum.

[22]Membranes were soaked for 72 hours in five liters of 77 mM NaCl with a small amount of EDTA so that their ionic strength would be approximately that of the measuring electrolyte.

While gland locations can be quantified, these other factors are not accessible. Permeability studies [46] suggest that these factors will vary little if at all within an small area, provided that this area is in a functionally similar and superficially homogeneous region of the skin (an area subject to the formation of callus, for example, would have a thicker stratum corneum than some adjacent region; and areas differing in pigmentation might also differ in electrical properties). In terms of potential measurements within such a restricted area, the smaller the electrode, the larger the number of non-overlapping measurement sites there will be. Furthermore, if the potential is affected by the number of glands within the electrode area, then the potential change per additional gland occluded is likely to be greater for a small electrode[23].

3.9.2 Choice of electrodes and electrolyte

These criteria led to the development of an electrode apparatus with a sensitive area (approximately 3 mm^2) smaller than that of any available standard miniature skin electrode (20 mm^2). This apparatus coupled the electrodes to the skin by liquid electrolyte-filled tubing and so resembles an arrangement used to measure transepithelia potentials in the nasal septum and the esophagus [23,25]. While bare metal electrodes would have been much easier to work with, they cannot be used for low frequency measurements since their polarization impedance makes them behave as high-pass filters. Miniature wick and agar gel systems were found to be susceptible to dehydration which led to instability in the measured potentials.

[23]In other words, $n + 1$ is more easily distinguished from n if n is small.

Saline isotonic with surface perspiration was used because it was a physiological electrolyte, as opposed to commercial electrolyte pastes whose hypertonicity and abrasive qualities can damage the skin). The electrolyte was used without containment (such as an adhesive ring applied on the skin) since the occlusion of the skin by such rings leads to the rapid hydration of the stratum corneum underneath the ring, and thus the effective shorting of this area to the actual measurement area.

3.9.3 Location of test area

The location of the measurement area used in these studies was determined by its accessibility, the comfort of the subject during the measurement, and the fact that the area had to be relatively flat for the gland imaging technique to work well. In addition, any path between electrodes could not include the heart. The region chosen as the test area for all subjects was the area on the back of the hand bounded by the wrist and the bases of the thumb and forefinger.

4 Experimental Results and Statistical Analysis

4.1 Summary

This chapter gives the electric potential measurement results, and then presents the outcome of the gland location analysis. A description of the method used to relate the potential grid to the gland locations follows. The grid of potential measurements on the back of the hand made up a nine by nine element array (Section 4.2). The mean potential for the eight subjects studied was 24.86±8.16 mV. Marks made on a disc of blotting paper by secreting glands were identified in a digitized image to form an array of gland locations (Section 3.5.3). The mean gland count over all the records for an electrode radius of 1 mm was 9.09±3.55 glands. Since the electrode area was not well defined, arrays were generated for a range of radii close to the mean electrode area radius (Section 4.4). The correlation (Section 4.5) between each such array and the appropriate potential grid was calculated and plotted (Section 4.6). In general, the measured potential was independent of the gland count at the measurement site. In those cases where some correlation was observed, it was probably due to experimental error. Care was taken to ensure that both distributions were adequately sampled.

4.2 Results of potential measurements

The mean potential over all the records was 24.86 mV, with a variance of ±8.16 mV. This result is comparable to measurements made with similar protocols and equipment by other investigators. Barker and his co-workers [2] surveyed the transcutaneous potentials on an unspecified area on the back of the hand, and found

values of 34 ± 3 mV for one subject and 45 ± 4 mV for another. In their study of 'human skin battery' potentials, Foulds and Barker [3] found a mean transdermal potential of 23 ± 9 mV, however this represents an average over the entire body[24]. Table 1 summarizes the results of the potential measurements and gland number estimates for all subjects. The mean number of glands within a radius of one mm of the measurement site is given as well. The mean of this average (that is, the mean of all the estimates with $r = 1$ mm) was 9.09 ± 3.55 glands.

Figure 9 shows a portion of the chart output for one experiment. As noted in Section 3.6, the stable potential was measured for at least 15 to 20 seconds at each site in the grid. The initial shoulder in each drift trace (the output reads from right to left) was due to the capacitance of electrolyte double layers in the circuit and the high resistance of the electrode lines. The slower rise of the measurement trace reflects the time required for the the electrolyte to percolate into the dehydrated stratum corneum. The shape is not the same for each trace in part because of small delays between the time that the electrolyte droplet was placed on the skin and the point at which the amplifier was turned on.

Figure 10 contains the potential records for all subjects. Points in the square grid pattern that were outside the circular measurement area on the skin are indicated by 'nm', while 'om' designates a measurement that was excluded from the record. Measurements were omitted from the record if they were too near the edge of the blot disc (i.e. if there was not enough gland location data in the vicinity of the probe location); if the probe location coincided with a visible anatomic feature that might affect the potential (such as a mole); or if the measured potential was

[24]In fact, the values in both accounts may be too high since it is not clear if the bridge offset potentials were compensated for.

Reference			Results of potential measurements				
Exp. #	Sample name	Potential record	# of sites	$\overline{X}_\psi$ of sample	σ of ψ	$\overline{X}_{glands}$ for r = 1 mm	σ of glands
1	h41r	hs1cor	61	18.85	4.48	9.58	0.28
1	h36r	hs1cor	61	18.85	4.48	8.62	0.11
2	h44r	hs2cor	71	29.89	3.80	10.26	0.34
2	h43b	hs2cor	71	29.89	3.80	9.66	0.23
3	h54b	hs3cor	61	32.14	4.08	8.53	0.15
3	h53b	hs3cor	61	32.14	4.08	8.21	0.17
3	h55r	hs3cor	61	32.14	4.08	9.32	0.16
4	m46b	pmcor	62	19.52	3.55	8.20	0.09
5	j43b	jecor	58	35.44	5.49	9.59	0.21
5	j44b	jecor	58	35.44	5.49	9.08	0.11
6	k42b	jkcor	57	14.72	4.65	10.80	0.16
6	k42r	jkcor	57	14.72	4.65	10.86	0.25
6	k44b	jkcor	57	14.72	4.65	11.04	0.10
7	p53r	hpcor	59	18.98	3.67	6.41	0.08
7	p54b	hpcor	59	18.98	3.67	6.46	0.06
8	m42r	jmcor	58	28.43	3.18	8.71	0.01

Table 1: *Summary of potential measurements, including mean estimated number of glands for an electrode radius of one mm. The mean $\overline{X}_\psi$ and sample variance σ of the potentials are in mV.*

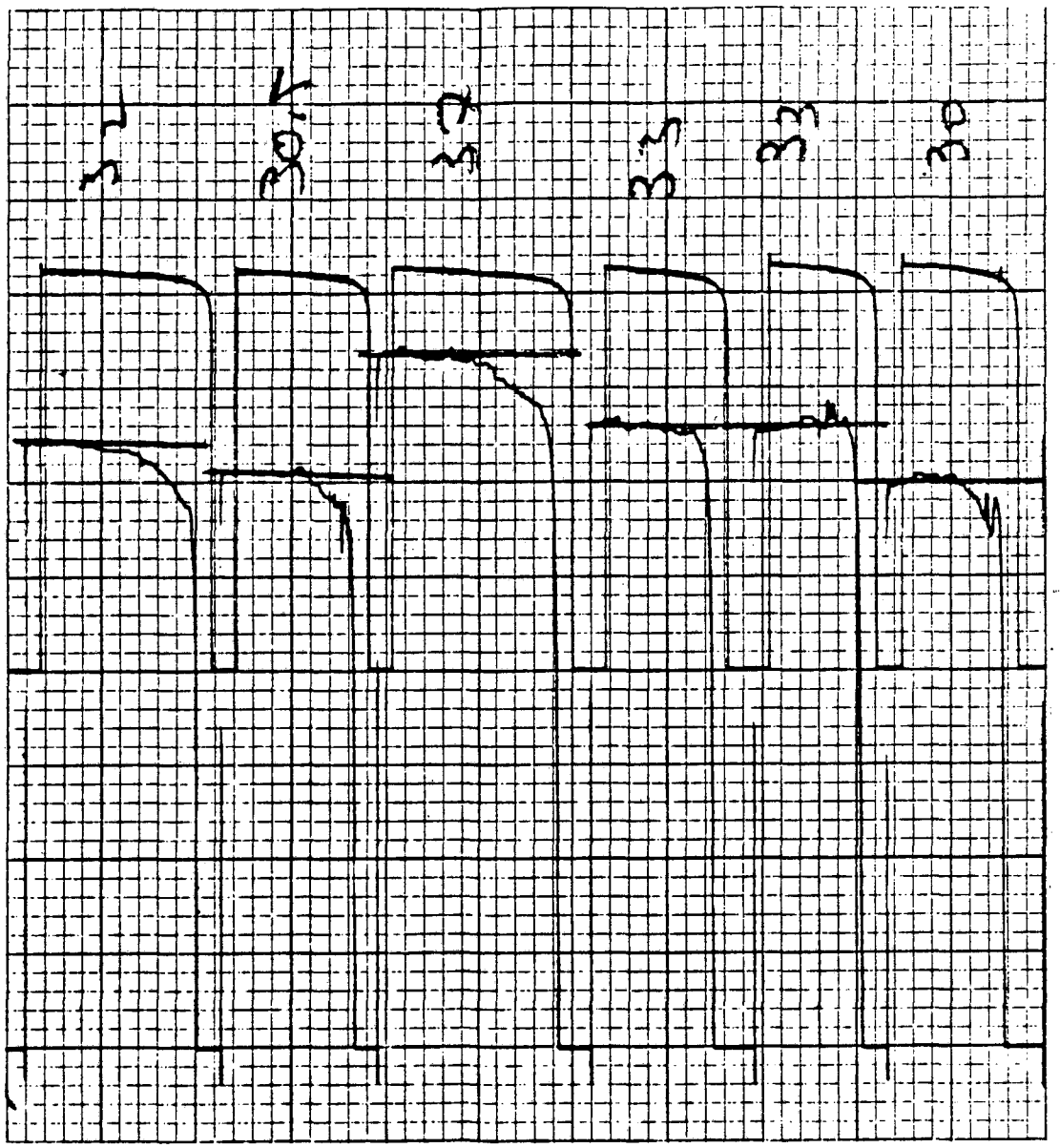

Figure 9: *Portion of chart output for potential record hs3cor.pr. The upper trace is the drift, with the experimental record below it. Vertical scale is 1.0 mV/small division, horizontal scale is 0.5 minute/large division(five small divisions).*

not stable. Note that the chart output in Figure 9 (reading from right to left) is part of the third row of record hs3cor.pr in Figure 10.

4.2.1 Potential contributions from hair follicles and other sources

As noted in Section 2.6, some investigators have suggested that hair follicles may influence the potential. These experiments found no evidence in support of this proposition. When the electrode was on or very near to a follicle, as it occasionally was, the measured potential was not noticeably or consistently different from the potential at sites surrounding that location. In two instances the potential over a follicle varied during the measurement when the hair was acting as a wick for the electrolyte and disturbed its interface with the skin. In both cases, the addition of more electrolyte stabilized the trace.

The skin of some volunteers was so dry after alcohol dehydration that a stable measurement could not be obtained without using four to five times the normal amount of electrolyte per measure. These individuals did not participate in the study. When the electrode droplet was on a mole (and in one instance, when it covered a small, bright-red area), the potential could be several millivolts higher than for the surrounding measures, but this was not a consistent finding. Measurements which took place on a hair follicle or a surface feature that was visibly different from the skin around it (such as a mole) were omitted from the potential grid in every instance. Skin that had a wound or scab was not examined.

Potentials significantly higher or lower than those surrounding them, but that were not associated with any visible surface feature were found in some of the records (the circled values in Figure 10). In two cases (records jkcor.pr and jmcor.pr), a

POTENTIAL RECORD: HS1COR.PR

nm	nm	nm	21.	22.	29.	24.	nm	nm
nm	22.	25.	23.	23.	23.	23.	25.	nm
nm	20.	25.	24.	27.	23.	21.	22.	22.
22.	om	24.	23.	om	21.	16.	16.	16.
19.	22.	16.	23.	19.	20.	19.	12.	12.
19.	26.	19.	om	20.	18.	14.	10.	13.
nm	14.	14.	12.	16.	20.	15.	15.	9.
nm	16.	21.	17.	12.	17.	10.	nm	nm
nm	nm	nm	19.	18.	18.	14.	nm	nm

POTENTIAL RECORD: HS2COR.PR

nm	34.	34.	34.	38.	35.	37.	33.	nm
nm	35.	35.	35.	35.	33.	30.	35.	nm
31.	34.	35.	31.	30.	30.	23.	34.	nm
30.	30.	33.	26.	30.	26.	32.	33.	34.
32.	31.	29.	32.	31.	24.	26.	30.	29.
32.	om	31.	26.	26.	27.	25.	28.	31.
34.	27.	28.	31.	24.	26.	28.	30.	25.
nm	23.	24.	24.	27.	25.	33.	31.	31.
nm	nm	24.	25.	28.	28.	31.	34.	nm

POTENTIAL RECORD: HS3COR.PR

nm	nm	nm	33.	30.	37.	40.	nm	nm
nm	nm	31.	30.	31.	34.	35.	nm	nm
nm	nm	33.	30.	33.	33.	37.	31.	32.
29.	31.	25.	32.	30.	31.	32.	34.	34.
32.	30.	31.	33.	34.	32.	33.	32.	34.
nm	13.	34.	36.	30.	34.	28.	30.	32.
nm	18.	37.	34.	35.	33.	31.	33.	31.
nm	33.	37.	33.	37.	37.	32.	34.	nm
nm	nm	nm	37.	36.	33.	32.	nm	nm

POTENTIAL RECORD: JECOR.PR

nm	nm	nm	nm	31.	21.	25.	nm	nm
nm	29.	34.	31.	32.	33.	34.	nm	nm
nm	32.	nm	31.	31.	22.	35.	32.	32.
35.	om	33.	34.	33.	37.	35.	37.	35.
31.	om	39.	37.	48.	40.	43.	33.	29.
35.	37.	40.	47.	32.	om	40.	35.	39.
nm	37.	43.	43.	44.	40.	37.	35.	31.
nm	40.	41.	44.	40.	37.	om	28.	nm
nm	nm	nm	40.	39.	40.	40.	nm	nm

POTENTIAL RECORD: JKCOR.PR

nm	nm	nm	nm	nm	nm	nm	nm	nm
nm	15.	4.	16.	13.	11.	15.	12.	nm
nm	15.	15.	18.	12.	8.	23.	16.	23.
14.	11.	14.	16.	9.	15.	20.	22.	21.
20.	16.	1.	17.	15.	18.	20.	21.	19.
6.	6.	14.	15.	om	om	17.	18.	19.
nm	13.	17.	15.	14.	15.	20.	14.	nm
nm	5.	15.	15.	15.	17.	8.	nm	nm
nm	nm	om	15.	20.	14.	17.	nm	nm

POTENTIAL RECORD: PMCOR.PR

nm	nm	nm	25.	22.	23.	23.	nm	nm
nm	18.	21.	23.	20.	10.	15.	13.	nm
nm	25.	18.	15.	16.	14.	15.	14.	14.
nm	22.	20.	11.	16.	17.	17.	17.	17.
19.	18.	22.	17.	19.	19.	19.	23.	19.
24.	21.	18.	22.	17.	22.	23.	24.	25.
nm	21.	21.	22.	18.	24.	19.	21.	25.
nm	19.	21.	22.	20.	24.	om	23.	nm
nm	nm	om	24.	om	22.	20.	nm	nm

POTENTIAL RECORD: HPCOR.PR

nm	nm	nm	18.	20.	19.	23.	nm	nm
nm	15.	15.	15.	20.	21.	20.	22.	nm
nm	11.	12.	19.	25.	20.	18.	18.	nm
16.	16.	15.	10.	13.	15.	24.	24.	24.
22.	23.	21.	19.	21.	19.	19.	23.	22.
20.	19.	13.	18.	19.	25.	16.	23.	22.
nm	20.	17.	19.	19.	19.	23.	23.	21.
nm	21.	17.	23.	19.	24.	11.	nm	nm
nm	nm	nm	nm	nm	nm	nm	nm	nm

POTENTIAL RECORD: JMCOR.PR

nm	nm	nm	29.	om	24.	42.	nm	nm
nm	26.	28.	28.	31.	30.	33.	nm	nm
nm	29.	24.	28.	30.	29.	30.	32.	32.
29.	25.	28.	30.	om	28.	32.	30.	28.
26.	28.	31.	29.	33.	27.	30.	om	31.
23.	27.	om	23.	28.	29.	26.	22.	26.
nm	33.	29.	27.	27.	29.	29.	om	30.
nm	33.	28.	30.	29.	29.	26.	22.	nm
nm	nm	nm	28.	25.	30.	nm	nm	nm

Figure 10: *Potential grids for all subjects. Certain anomalous values (circled) are discussed in the text. Sites indicated by 'nm' or 'om' were not correlated.*

second measurement later in the experiment at the same location confirmed the anomalous value. Anomalous potentials of this sort were also seen in some of the preliminary experiments, and seemed to occur at the same approximate location in measurements made at different times. This latter finding was not replicated in the present study. No explanation for these unusual values is offered, other than to note that there are claims that electrical potentials at acupuncture points are consistently higher [77] or lower [78] than at surrounding spots.

4.3 Results of gland location analysis

The blot discs were initially digitized (as described in Section 3.5) as 256x256 images. This pixel size did not adequately resolve very small gland blots, and so the discs were redigitized with a resolution of 512x512 and the analysis software rewritten to accomodate the larger arrays. Several of these large digitized images could not be analyzed because a substantial number of the individual gland blots did not have well-defined centers. Large sweat droplets had resulted in large and often ellipsoidal blots, so that there was as much as ± 3 pixels uncertainty in the location of their pore centers.

The pattern recognition software identified about 65% of the gland centers in any given image, and the remainder were located manually with the bidpad, most often through the separation of merged glands. Total glands per disc ranged from 1273 to 2068, or approximately 200 to 330 glands per cm^2, which is in good agreement with literature values [57,58]. Table 2 includes the total gland counts for all the discs. It should be pointed out that the blotting technique samples the glands rather than counting them, so that no single disc shows all the active glands

within the area. Questions relating to sampling are considered in Section 4.6 below.

4.4 Registering the potential grid with the gland locations

The triplet of fiducial marks established a correspondence between the probe locations and the gland locations. Once the potential measurement sites were assigned coordinates in the gland location matrix, then the number of pore centers within a given radius of each measurement site could be determined. The pore counts for all sites in the potential grid formed a 'proximity array' for that radius. Because the electrode area (the area hydrated by the electrolyte, Section 3.2.6) was not well defined, pore counts were also made for radii smaller and larger than 1.0 mm, the measured radius of the electrode area. The nine radii used[25] generated nine proximity arrays.

Small discrepancies between the locations of skin fiducials and disc fiducials were discovered during the course of the data analysis. These differences were due to a lack of accuracy in the technique used to locate the marks on the skin (the occlusion of the ink mark with the electrode tip, Section 3.3.2). Since the fiducial template placed the marks at the vertices of a right isosceles triangle of known dimensions, it was possible to detect and partially compensate for these errors. Each pair of fiducial locations was used to calculate the expected position of the third. The degree of agreement between the original fiducial locations and these 'derived' sets is a measure of how accurately the marks were located[26].

[25]Each radial value R used in the program was chosen so that the area it defined in the digitized image was approximately equal to πR^2. For example, $R = 1.15$ mm has an 'analog area' of 1360 pixels, but a 'digital area' of 1353 pixels. In this instance, an $R = 1.151$ mm which had a digital area of 1361 pixels was used instead.

[26]This relationship between the fiducials was also used to test the location of the fiducials in the

Reference			Gland location results	
Expt. #	Sample name	Potential record	Blot disk	Total pores
1	h41r	hs1cor	hs03314	1751
1	h36r	hs1cor	hs03316	1747
2	h44r	hs2cor	hs04214	2006
2	h43b	hs2cor	hs04213	1905
3	h54b	hs3cor	hs05094	1666
3	h53b	hs3cor	hs05093	1572
3	h55r	hs3cor	hs05095	1853
4	m46b	pmcor	pm04156	1688
5	j43b	jecor	je04253	1765
5	j44b	jecor	je04254	1621
6	k42b	jkcor	jk04162b	1999
6	k42r	jkcor	jk04162r	2053
6	k44b	jkcor	jk04164	2068
7	p53r	hpcor	hp05123	1287
7	p54b	hpcor	hp05124	1273
8	m42r	jmcor	jm04263	1674

Table 2: *Summary of gland location results.*

Three groups of such derived fiducials were generated for each sample by this method, with each group based on two fiducials from the original set. Since there were thus three possible grid placements (one for each group of derived fiducials) and nine proximity arrays for each such placement (one for each radius), there were a total of 27 proximity arrays generated for each sample. Each of these arrays was tested for correlation with the measured potentials. Figure 11 shows the nine proximity arrays for one group of derived fiducials in sample k42b.

4.5 Choice of analysis and formulas used

Sample correlation coefficients were calculated to assess whether the number of inactive glands in the electrode area was related to the transdermal electrical potential. The existence of such a relationship was suggested by consideration of the statistical analysis of the proximity arrays (Figure 12), which showed that between 5 and 15 glands were located within 0.8 to 1.2 mm of a potential measurement site, and the equivalent circuit model (Chapter 5) which predicted a nearly linear relationship between potential and the number of glands in this range. The quantity r (the estimator of the correlation coefficient ρ) was calculated and evaluated for significance at the 5% or 1% level to test the null hypothesis ($\rho = 0$) that potential and gland counts did not correlate. The number of degrees of freedom was equal to $n - 2$, where n is the number of measurement sites correlated.

The formulas used were:

digitized image. Fiducial coordinates that did not have the right geometry or the correct interpoint distances were not accepted by the location program.

For radius = 1.200:

nm	nm	nm	nm	13	15	nm	nm	nm
nm	nm	nm	11	14	17	15	nm	nm
nm	17	15	15	11	16	18	14	nm
nm	11	15	12	15	18	18	14	14
nm	14	16	13	17	15	13	16	15
nm	15	11	13	12	17	12	15	16
nm	14	13	13	13	12	15	16	nm
nm	nm	16	14	17	16	10	nm	nm
nm	nm	nm	12	12	14	nm	nm	nm

For radius = 1.150:

nm	nm	nm	nm	13	15	nm	nm	nm
nm	nm	nm	10	13	16	14	nm	nm
nm	17	15	14	11	15	17	13	nm
nm	11	15	11	15	18	16	13	14
nm	13	15	12	16	14	13	16	15
nm	14	11	11	12	16	11	15	15
nm	12	13	13	12	12	14	15	nm
nm	nm	15	14	17	15	10	nm	nm
nm	nm	nm	11	12	14	nm	nm	nm

For radius = 1.100:

nm	nm	nm	nm	11	14	nm	nm	nm
nm	nm	nm	9	13	13	13	nm	nm
nm	15	13	13	11	14	16	12	nm
nm	10	14	9	14	17	15	13	14
nm	11	13	12	13	12	12	14	13
nm	13	9	11	12	16	11	14	13
nm	11	13	12	12	12	14	13	nm
nm	nm	13	12	16	15	9	nm	nm
nm	nm	nm	11	10	14	nm	nm	nm

For radius = 1.050:

nm	nm	nm	nm	10	14	nm	nm	nm
nm	nm	nm	9	13	13	13	nm	nm
nm	14	13	12	11	13	14	11	nm
nm	10	12	9	12	16	15	11	13
nm	11	12	12	11	11	11	12	12
nm	11	7	10	10	14	11	12	12
nm	10	12	11	11	11	13	11	nm
nm	nm	13	11	13	14	9	nm	nm
nm	nm	nm	11	10	13	nm	nm	nm

For radius = 1.000:

nm	nm	nm	nm	9	12	nm	nm	nm
nm	nm	nm	9	11	11	12	nm	nm
nm	11	11	10	11	11	11	10	nm
nm	8	11	9	12	15	15	11	12
nm	11	11	12	10	11	11	12	10
nm	11	6	9	10	12	11	11	9
nm	9	12	10	10	10	12	11	nm
nm	nm	12	10	11	12	9	nm	nm
nm	nm	nm	10	10	12	nm	nm	nm

For radius = 0.950:

nm	nm	nm	nm	8	9	nm	nm	nm
nm	nm	nm	9	11	9	11	nm	nm
nm	10	10	10	8	9	10	9	nm
nm	7	10	7	11	12	11	10	9
nm	10	10	11	10	10	10	12	9
nm	10	6	8	10	11	11	11	8
nm	9	10	10	8	9	12	11	nm
nm	nm	11	9	11	11	8	nm	nm
nm	nm	nm	9	8	10	nm	nm	nm

For radius = 0.900:

nm	nm	nm	nm	7	8	nm	nm	nm
nm	nm	nm	8	10	9	11	nm	nm
nm	9	10	9	7	8	9	8	nm
nm	7	8	6	10	10	11	10	8
nm	9	10	10	8	9	9	11	8
nm	9	6	6	10	11	10	8	7
nm	9	9	9	8	7	12	11	nm
nm	nm	9	9	11	10	6	nm	nm
nm	nm	nm	9	8	8	nm	nm	nm

For radius = 0.850:

nm	nm	nm	nm	7	8	nm	nm	nm
nm	nm	nm	8	9	8	8	nm	nm
nm	8	9	8	6	8	8	8	nm
nm	6	8	5	7	9	11	10	8
nm	8	8	9	6	8	8	8	8
nm	7	6	6	9	10	8	7	7
nm	8	7	8	8	6	9	10	nm
nm	nm	8	8	10	8	6	nm	nm
nm	nm	nm	8	8	7	nm	nm	nm

For radius = 0.800:

nm	nm	nm	nm	7	7	nm	nm	nm
nm	nm	nm	7	8	8	8	nm	nm
nm	8	9	8	6	7	7	6	nm
nm	6	8	5	6	9	11	9	7
nm	7	6	7	6	8	6	8	7
nm	7	6	5	9	9	6	7	7
nm	8	6	7	7	6	9	9	nm
nm	nm	7	6	7	4	4	nm	nm
nm	nm	nm	7	6	6	nm	nm	nm

PROXIMITY ARRAYS WITH RESPECT TO
FIDUCIAL MARKS LOCATED AT:

97 406
419 407

GLAND COUNTS FROM ANALYSIS FILE:
SS2K42B.DIA

Figure 11: *The proximity arrays associated with one group of fiducials for sample k42b. Array locations labelled 'nm' fell outside the measurement site on the skin.*

Correlation of potential with eccrine gland counts
for a range of electrolyte droplet sizes

Potential record: JKCOR.PR
Gland counts as f(radius): SS2K42B.DIA
Correlation (this file): SS2K42B.CCF

rad	Mp	Mg	Vp	Vg	cov	r
1.200	15.10	14.33	16.95	4.14	0.90	0.108
1.150	15.10	13.71	16.95	4.00	0.92	0.112
1.100	15.10	12.63	16.95	3.43	1.28	0.168
1.050	15.10	11.71	16.95	2.68	1.08	0.161
1.000	15.10	10.75	16.95	2.28	1.01	0.162
0.950	15.10	9.69	16.95	1.84	0.97	0.174
0.900	15.10	8.81	16.95	2.11	0.92	0.154
0.850	15.10	7.81	16.95	1.43	1.43	0.291
0.800	15.10	6.98	16.95	1.81	1.53	0.277

Total number of measurement sites correlated = 48

rad = radius of electrolyte droplet (mm)
Mp = mean of all potentials over the region (mV)
Mg = mean number of eccrine glands within a given radius
Vp,Vg = variance of potentials, and of gland counts
cov = covariance of potentials and gland counts
r = correlation coefficient, gland count vs potential

Figure 12: *Results of the analysis of one of the proximity arrays for sample k42b versus the potential record jkcor.pr. An 'nm' indicates that the site was not measured.*

for the sample mean $\overline{X}$

$$\overline{X} = \frac{\Sigma X}{n},$$

where ΣX is the sum of all data values and n is the number of data points;

for the variance σ

$$\sigma = \frac{\Sigma(X - \overline{X})^2}{n - 1};$$

and for r, the estimator of the correlation coefficient ρ,

$$r = \frac{\Sigma x_1 x_2}{\sqrt{(\Sigma x_1^2)(\Sigma x_2^2)}},$$

where $x_1 = (X_1 - \overline{X}_1)$ and $x_2 = (X_2 - \overline{X}_2)$, and $\Sigma x_1 x_2$ is the covariance . Values of r near 1 denote a positive correlation, values near -1 indicate negative correlation, and $r = 0$ indicates that there is no correlation between the two variables.

4.6 Results of statistical analysis

The correlation between each of the gland proximity arrays and the appropriate grid of potentials was calculated. Most of the values obtained were not significant at the 1% and 5% levels, indicating that the potential was independent of the number of pores under the electrode. The cases in which the potential and gland count appeared to correlate were probably due to experimental error. While potential and pore distributions were adequately sampled, and the method of locating one array with respect to the other could be improved, a better method of locating the fiducials would probably not increase the correlation. Plots of correlation versus electrode droplet radius showed that the three sets of derived fiducials were similar in fourteen out of sixteen samples. Furthermore, the lines were close together (which

showed that the fiducials had been located with adequate accuracy) and there were no local maxima of correlation as a function of displacement. In other words, the correlation did not change substantially as a function of either the derived set or with the number of glands under the electrode, and thus some error in locating the fiducials would not affect the outcome.

4.6.1 Sampling considerations

Several assumptions are made about the sampled populations:

1. That there is uniform delivery of pilocarpine over the surface of the skin. Unequal delivery could occur if the electrical resistance to the flow of the ionized drug differed across the test area. The resistance of wet skin is small enough to be neglected [4] and in any event is unlikely to vary substantially within the area. By positioning the iontophoresis electrode near to and parallel with to the skin surface, and by making sure that the electrode pad stayed wet throughout the procedure, unequal current division along paths from the electrode to the skin was avoided.

2. That all glands in the measurement area are equally activated by the drug. The procedure used was adapted from the protocol used by Children's Hospital, Oakland, in the sweat test for cystic fibrosis. This diagnostic assay relies upon the collection of a large volume of sweat, and is designed to 'turn on' all the glands and so maximize their output. Experimentally, none of the gland blots made showed evidence of differential activation (such as a gradient across the disc in the size of individual gland blots).

3. That the eccrine gland blots sample the gland population evenly across the entire area. Consecutive prints made in the same area for the same length of time (for example, discs hs03314/hs03316 and hp05123/hp05124 in Table 2) had approximately the same number of gland centers and had 96% of their gland images in common. The glands that were in one image but not the other appeared to be evenly distributed across the blot disc.

4. That the potential map is representative of the distribution of potential in the area. Preliminary studies found that the potential distribution was independent of the direction or order of the measurements. In addition, sites that were re-measured some time later had potentials that were within ± 1.5 mV of the original value. Since the potential across some unique anatomic feature (such as a mole) would be unrepresentative of the skin as a whole, any site that happened to fall on a visible nonuniformity in the skin (such as a mole or fiducial mark) was omitted from the grid. Because the measurements are not simultaneous, the grid would not approximate a 'snapshot' of the potential distribution if the potentials varied in time during the course of the experiment. As noted above (Section 3.7), if such time variation was detected by the drift electrode, the experiment was abandoned.

5. That the measured potential values are independent, i.e. that adjacent potentials are not affected by each other. This concern was addressed by the repeated dehydration of the area and by the separation of the measurement sites.

6. That the electrode area is constant for each measurement in the grid. In other words, that the spread of an electrolyte droplet of fixed size over the dry skin of a given individual is unlikely to vary greatly from one site to the next. As noted in Section 3.2.6, the mean diameter of the area hydrated by the electrolyte was 2.0 ± 0.1 mm.

4.6.2 Statistical analysis

One value for r was calculated for each of the nine proximity arrays associated with a particular derived fiducial set (Figure 12) and the nine values so obtained were plotted versus droplet radius (Figures 13 through 16). Each broken line in a plot represents a different derived fiducial set. No correlation was found for all such lines in plots for half the samples (Figures 13 and 14). Of the remaining samples, four (Figure 15) had at least one line with one or more r-values significant at the 5% level. The last four samples (Figure 16) each contained at least one line with one or more r-values above the 1% level. Plots in which these lines are very close together had skin fiducials that were located with relative accuracy. Table 3 summarizes the results of the study. Note that the correlation values in Figure 12 are plotted as the dotted line of the plot on the upper left of Figure 15.

4.6.3 Discussion

These results suggest that the potential does not correlate with pore count. This interpretation is strengthened if we recall that the measured radius of the electrode area was 1.0 ± 0.05 mm. If only the five central radii ($0.9 - 1.1$ mm) in each plot are considered, then just three samples out of sixteen remain significant (at the

Reference			Statistical results				
Expt. #	Sample name	Potential record	Sites corr.	RLN[1] of plot lines NR[2]	5%	1%	Fig. #
1	h41r	hs1cor	50	0	0	3	16
1	h36r	hs1cor	52	3	0	0	13
2	h44r	hs2cor	54	0	0(1)	3(2)	16
2	h43b	hs2cor	53	3	0	0	13
3	h54b	hs3cor	52	3	0	0	13
3	h53b	hs3cor	53	3	0	0	13
3	h55r	hs3cor	56	3	0	0	14
4	m46b	pmcor	52	3	0	0	14
5	j43b	jecor	47	1(3)	1(0)	1(0)	16
5	j44b	jecor	45	3	0	0	14
6	k42b	jkcor	48	2(3)	1(0)	0	15
6	k42r	jkcor	48	2(3)	1(0)	0	15
6	k44b	jkcor	47	0(1)	0(1)	3(1)	16
7	p53r	hpcor	46	2(3)	1(0)	0	15
7	p54b	hpcor	45	2(3)	1(0)	0	15
8	m42r	jmcor	46	3	0	0	14

Table 3: *Summary of statistical results. Numbers in () indicate counts if only the central five radii (0.9 to 1.1 mm) are considered.* [1]*Rejection Level of Null hypothesis,* [2]*Not Rejected.*

1% level). In addition, the first seven samples are from three separate experiments with the same subject, and for five of these seven, $r = 0$. Finally, there are three cases in which the analyses of samples from the same experiment (Experiments 1, 2 and 5 in Table 3) contradict each other, with one result suggesting correlation while the other does not. Since all disc fiducials were located with better than 1% accuracy and each pair used the same set of derived fiducials, this suggests that the apparent correlation in these cases may be due to chance or to an undetected experimental error. In other words, the conclusion of the statistical analysis is that the non-sudorific potential is not influenced by inactive eccrine glands.

The techniques used to determine the grid of potentials and to locate the pores on the skin provided adequate samples of both distributions, but the method used to establish the correspondence between the gland location array and the array of potentials is clearly in need of improvement. However, since the effective area of the electrode is not well defined and may in fact vary from one site to the next, the number obtained by this method for the glands in each electrode area would still be an approximation even if the array registration were perfect.

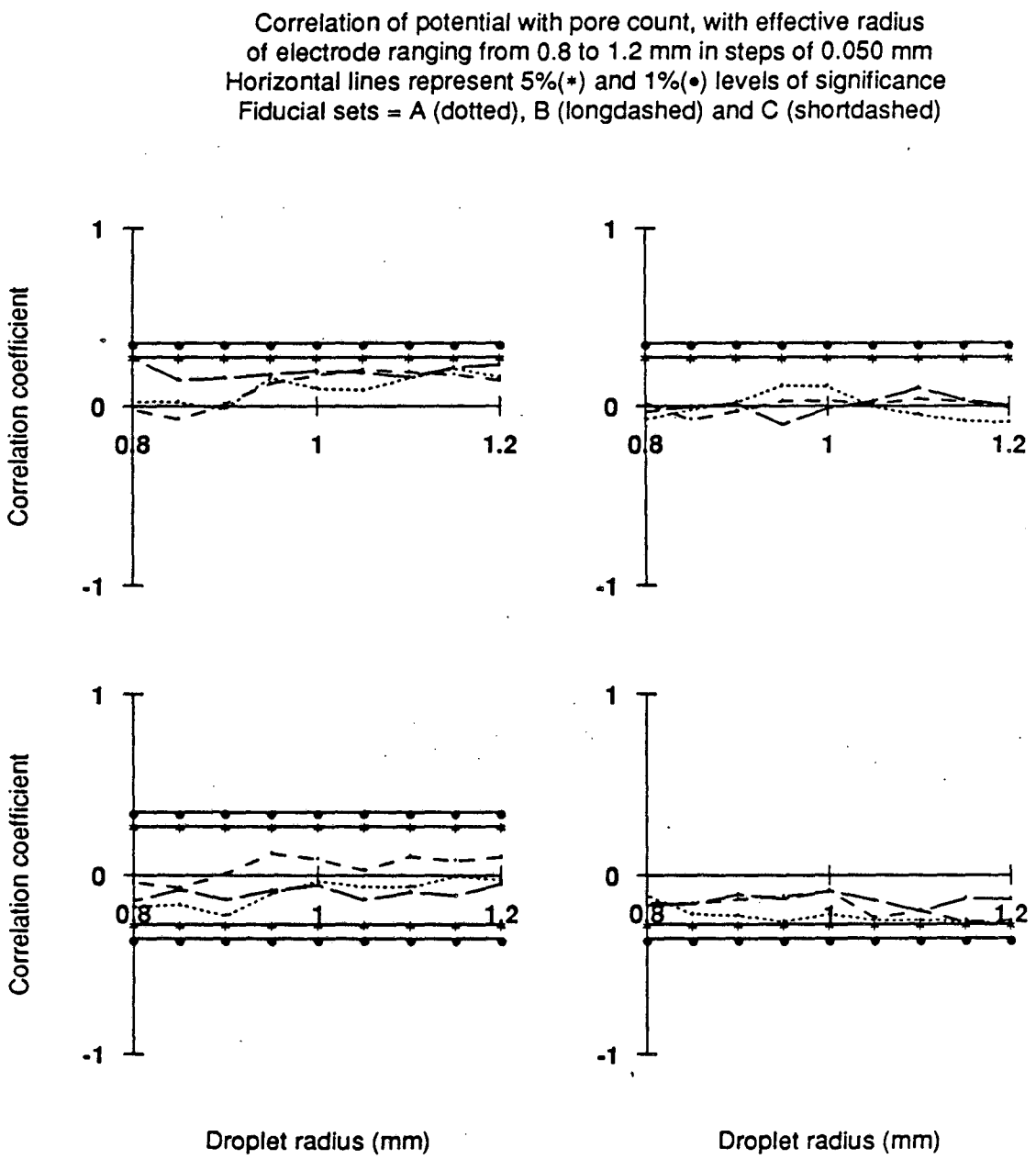

Figure 13: *Plots of correlation coefficient versus electrode radius for samples h36r (upper left), h43b (lower left), h54b (upper right), and h53b (lower right).*

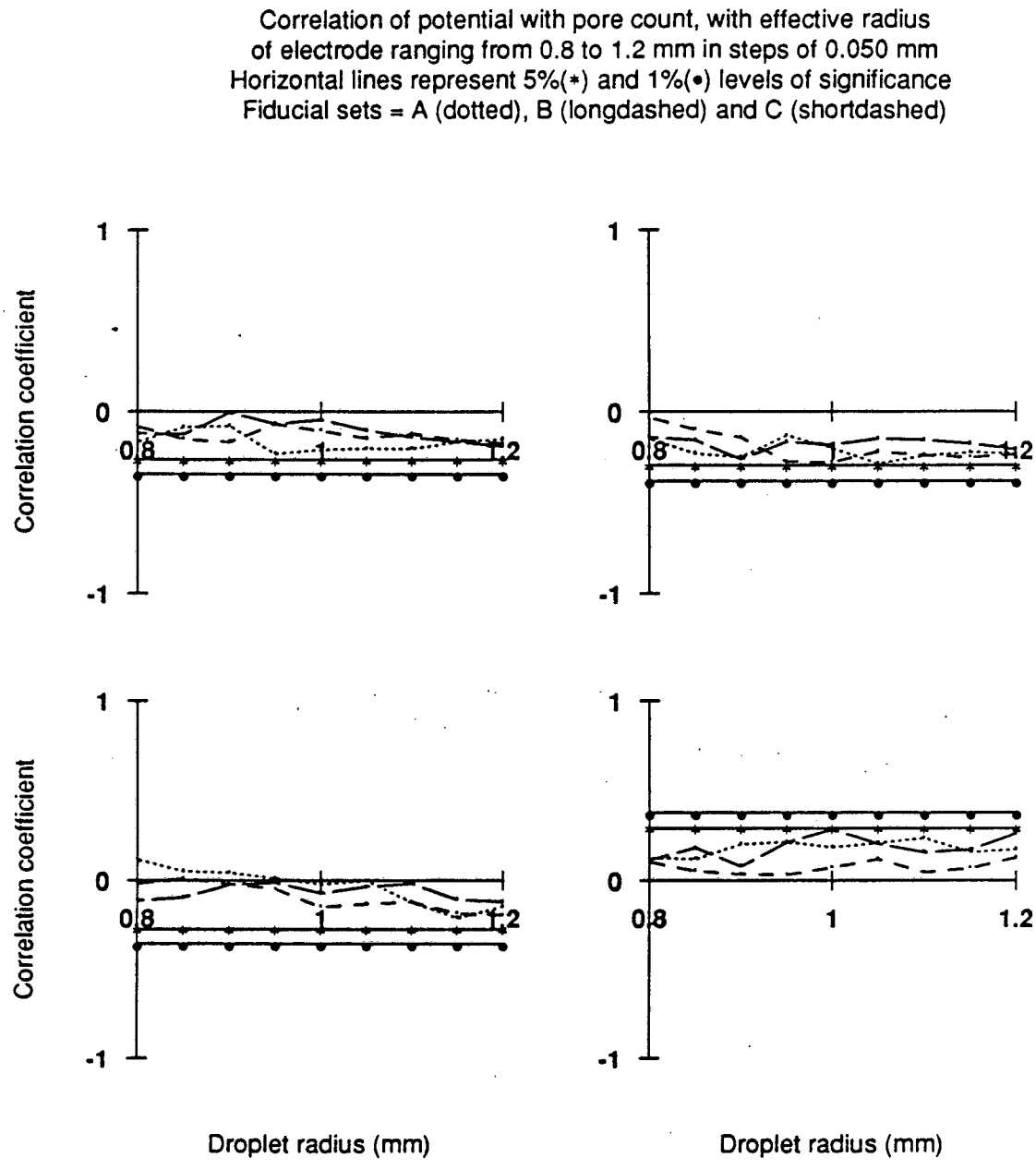

Figure 14: *Plots of correlation coefficient versus electrode radius for samples h55r (upper left), m46b (lower left), j44b (upper right), and m42r (lower right).*

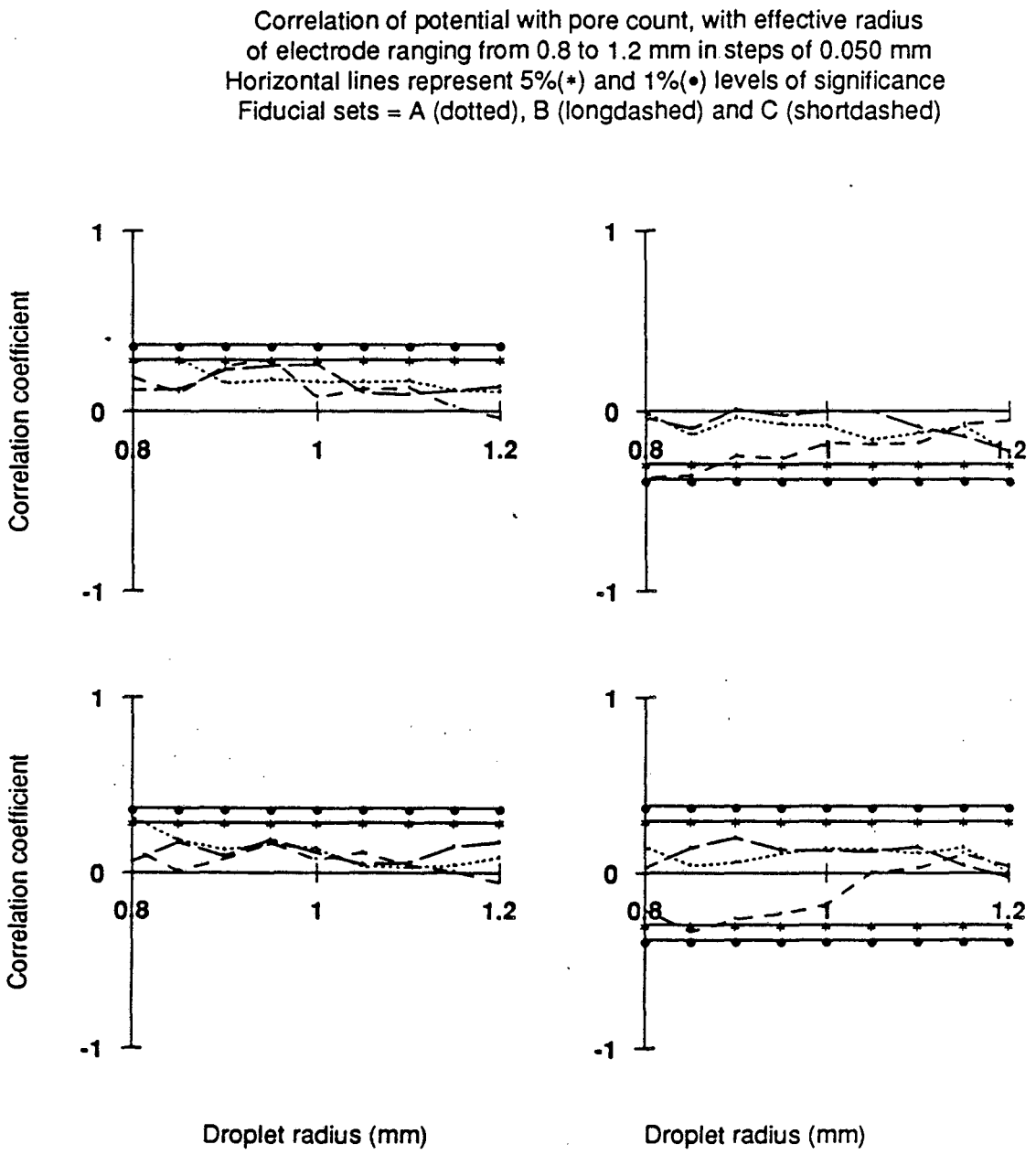

Figure 15: *Plots of correlation coefficient versus electrode radius for samples k42b (upper left), k42r (lower left), p53r (upper right), and p54b (lower right).*

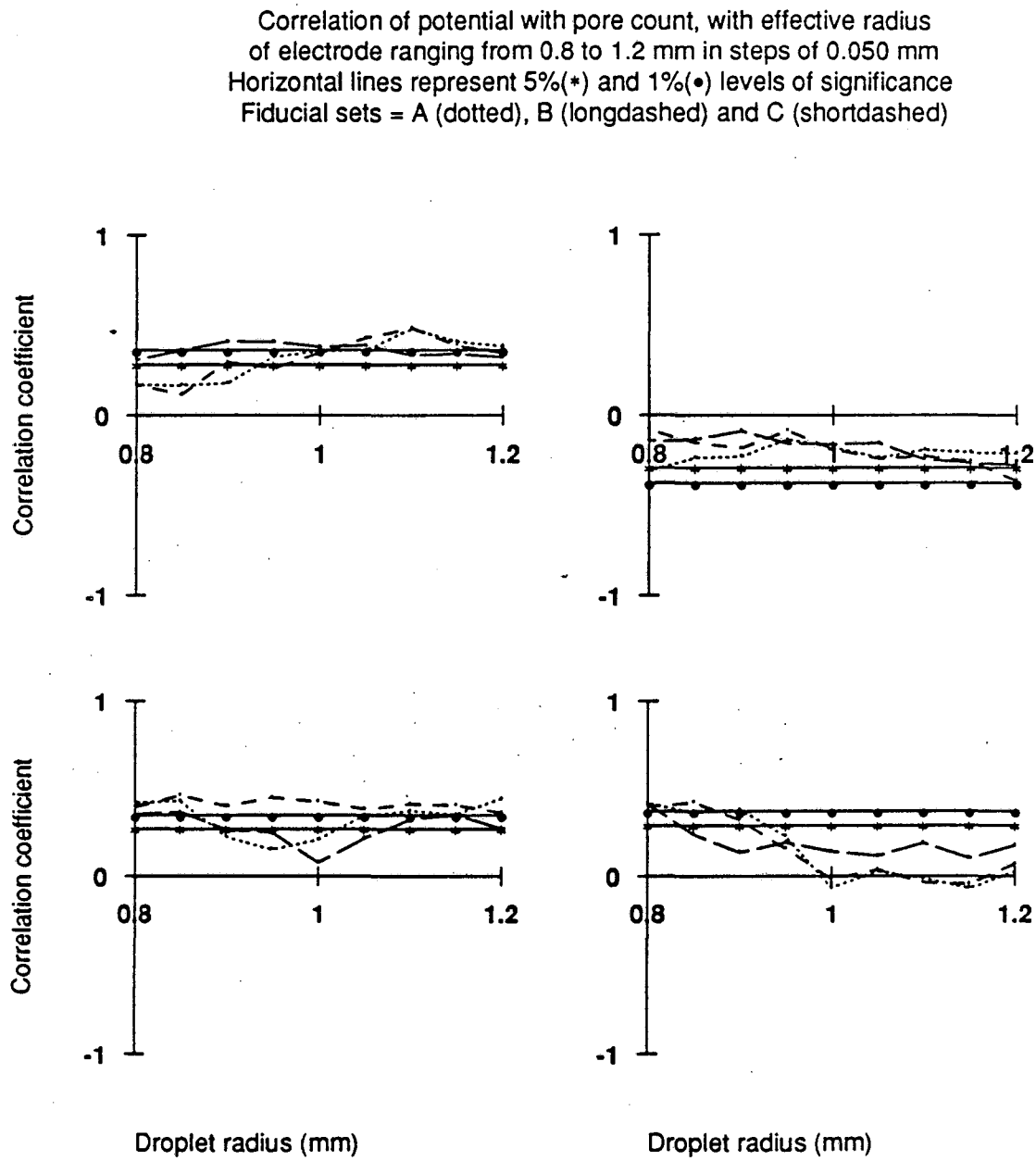

Figure 16: *Plots of correlation coefficient versus electrode radius for samples h41r (upper left), h44r (lower left), j43b (upper right), and k44b (lower right).*

5 Modelling Non-sudorific Electrical Potential Behavior of the Skin

5.1 Overview

The electrical properties of skin are usually described in terms of equivalent electric circuits [4,5,26]. Circuit modelling assumes that the electrical behavior of the modelled system can be represented by lumped elements connected in a particular manner[27]. In the case of the skin, these element values and current paths are poorly defined, and the value of modelling is not so much prediction as to point out areas in need of investigation.

The circuit model below is similar to those of Fowles [4] and Woodrough [5] but differs from them in that eccrine glands are considered only in terms of their passive contribution to the potential. The model predicts a dependence of potential on either the number of glands (behaving as passive sources) under the electrode or the magnitude of the potential across the permeabilty barrier (or a combination of these). As shown in Chapter 4, measurements of gland density did not correlate with potential. This model thus points to the barrier as the major source of transdermal potential variation. The permeabilty barrier probably behaves like a permselective membrane, thus changes in the potential across it could be due to either variations in the permselectivity of the membrane with respect to a particular ion (i.e. the specific ionic conductance) or to some local change in the competence of the barrier that affected its permselectivity for all ionic species.

[27]Models of skin electrical behavior based on solid-state physics exist [8,79] but are not widely accepted.

5.2 A circuit model for skin

5.2.1 Simplifying assumptions

The non-sudorific or 'resting' electrical behavior of non-glabrous skin is modelled with an equivalent electrical circuit by making certain simplifying assumptions:

1. All circuit elements are passive (including the sweat glands, which are not actively secreting). The lack of evidence for active transport in the barrier layer or the stratum corneum supports this assumption.

2. The passive electrical behavior of hair follicles is similar to that of inactive sweat glands [80].

3. Measurement protocols are such that contributions to the potential due to the apparatus and from the reference site are negligible, and that surface shunts between the measuring electrodes do not take place (Section 3.6).

4. Within a small region having homogeneous surface features (see Section 2.8) we assume a normal distribution of sweat gland sizes and densities and at most gradual minor variations in the dimensions of other skin structures (such as the thickness of the stratum corneum).

5.2.2 Paths of current flow in the skin

Current paths are shown in Figure 17. Paths one through three involve the epidermal portion of the sweat glands duct, which may be partially filled with electrode electrolyte, and path 4 goes directly through the hydrated stratum corneum. Resistive elements to current flow include the stratum corneum (R_e), the barrier

layer (R_b), both the epidermal (R_d) and dermal (R_t) duct walls, and the conductivity of the solution in the epidermal duct (R_s). Passive potentials may occur across the epidermal duct wall (E_d), the dermal duct wall (E_k), and the barrier layer (E_b). A junction potential (E_j) can exist between the electrolyte and any sweat remaining in the duct.

The resistance of the dermal portion of the duct is likely to be very high since it is unlikely that the electrolyte will fill the dehydrated duct to the depth of the dermis. Furthermore, if the subject is calm and relaxed, and the measurement environment is kept cool, duct filling from the bottom by secretory activity is unlikely to occur. The circuit can then be simplified by omitting the path through the dermal duct and duct wall (removing R_t and E_k).

The reduced model has sixteen variables. Of these, nine are known or can be estimated; four more are functions of these five; and the remaining three values are approximated (see below). Precise values for resistivities and potentials are difficult to determine since they are influenced by several factors, including site [5], mechanical deformation [17,19], the subject's state of arousal [15], temperature and relative humidity [26], as well as the method of measurement and the preparation of the site.

5.3 Analysis of the circuit model

A general model involving parallel paths through the skin is derived below. The behavior of the model is investigated after estimating values for each of its components. Expressions for the currents in a circuit consisting of one sweat gland in parallel with the epidermal component (Figure 17) were obtained by mesh analysis

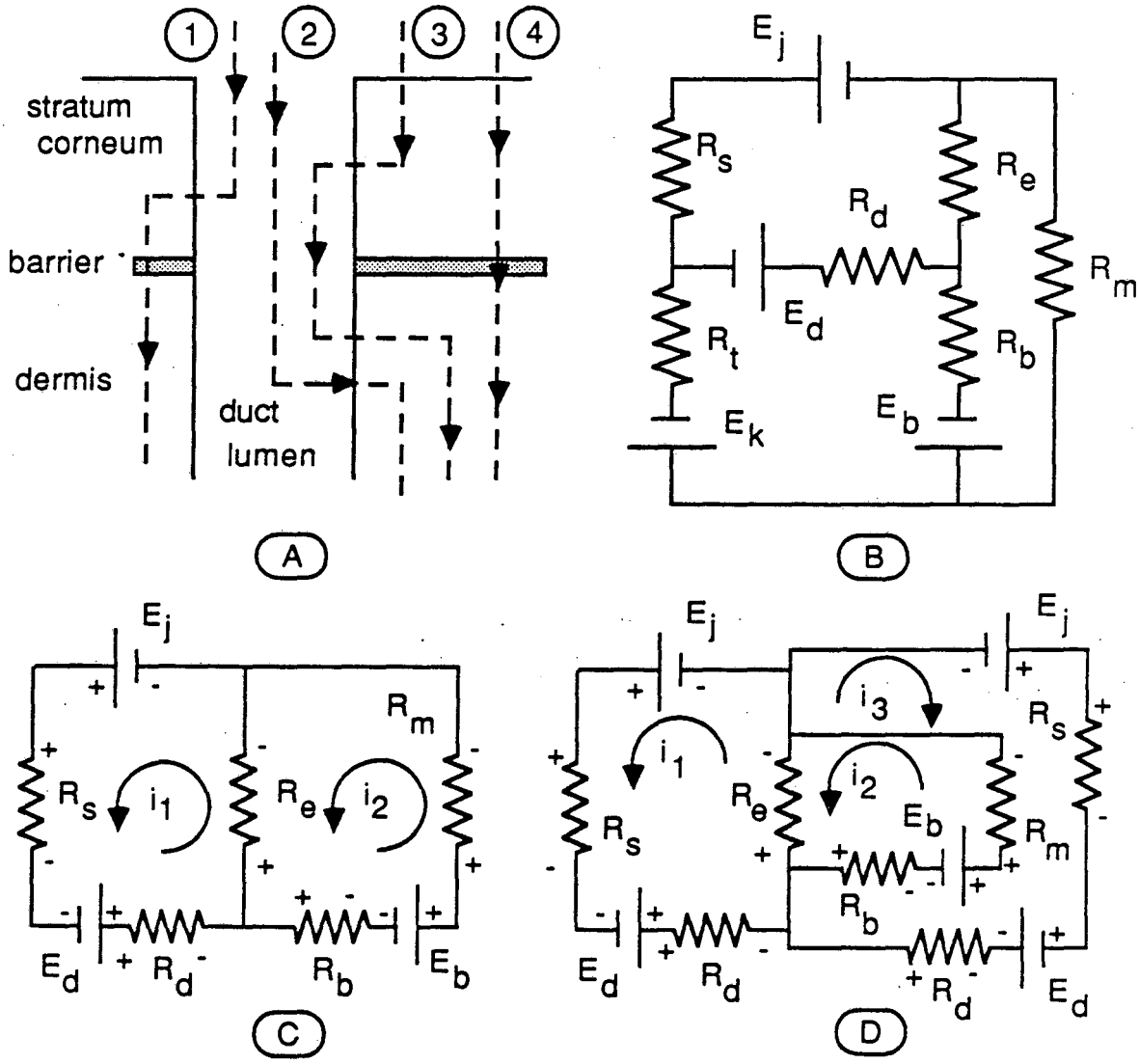

Figure 17: *(a). Paths of current flow in the skin. (b). The complete circuit model (c). The simplified circuit model with one gland and one epidermal element (d) The simplified model with two glands in parallel with a single epidermal component.*

[81]. Recalling that current flowing out of a node is positive, then Kirchhoff's Current Law at node (1) is:

$$i_1 - i_2 - i_3 = 0$$

By Ohm's Law, the voltage across a resistor is $E = iR$. The sum of the potential drops around mesh (1) is thus

$$R_d i_1 + R_e(i_1 - i_2) - E_j - E_d = 0.$$

Rearranging, we have Kirchhoff's Voltage Law (KVL) for mesh (1):

$$R_s i_1 + R_d i_1 + R_e(i_1 - i_2) = E_j + E_d.$$

Similarly, KVL for mesh (2) is:

$$R_m i_2 + R_e(i_2 - i_1) + R_b i_2 = E_b.$$

The two expressions of KVL are simultaneous equations that can be used to derive an expression for either current in terms of the circuit sources and resistances. To solve for i_2, the equations are expressed in terms of i_1 and i_2 and each is multiplied by a factor such that the i_1 terms cancel out when they are added together:

$$\begin{aligned}(R_e)[i_1(R_s + R_d + R_e) - i_2(R_e)] &= [E_j + E_d](R_e) \\ (R_s + R_d + R_e)[-i_1(R_e) + i_2(R_m + R_e + R_b)] &= [E_b](R_s + R_d + R_e)\end{aligned}$$

Solving for i_2,

$$i_2 = \frac{E_b(R_s + R_d + R_e) + (E_j + E_d)R_e}{(R_m + R_e + R_b)(R_s + R_d + R_e) - R_e^2}$$

Since the current i_2 travels through the electrometer resistance (R_m), the voltage across the skin is $V_n = R_m i_2$.

For two glands in parallel (Figure 17) with one epidermal component

mesh 1:

$$R_s i_1 + R_d i_1 + R_e(i_1 + i_3 - i_2) = E_j + E_d$$

mesh 2:

$$R_m i_2 + R_b i_2 + R_e(i_2 - i_1 - i_3) = E_b$$

mesh 3:

$$R_s i_3 + R_d i_3 + R_e(i_1 + i_3 - i_2) = E_j + E_d$$

where every element in the second gland loop is assumed to have the same value as the analogous element in the first loop ($R_{s_1} = R_{s_2} = R_s$, etc.). Solving for V_2,

$$V_2 = i_2 R_m = \frac{R_m[E_b(R_s + R_d) + 2R_e(E_j + E_d + E_b)]}{(R_m + R_b + R_e)(R_s + R_d) + 2R_e(R_m + R_b)}$$

The general form[28] for n glands is:

$$V_n = R_m i_2 = \frac{R_m[E_b(R_s + R_d) + nR_e(E_j + E_d + E_b)]}{(R_m + R_e + R_b)(R_s + R_d) + nR_e(R_m + R_b)} \tag{1}$$

where n is the number of sweat glands. Note that as in the case for two glands, the same elements in different circuit loops are assumed to have the same value. The behavior of the model is analyzed by the substitution of potentials and resistances whose values are estimated below.

5.4 Determination of circuit element values

5.4.1 Estimating resistances

Estimates of circuit resistances were made using approximations of specific resistances and dimensions for skin structures, the general form for the calculation

[28]The general form was derived with the symbolic manipulation program VAXIMA.

of resistance being

$$R_x = (\rho_x t_x)/A_x \tag{2}$$

where ρ_x is the specific resistivity in ohm-m, t_x is the thickness (in meters), and A_x is the area (in m^2) of the structure.

5.4.2 Estimation of resistivities for the barrier layer and stratum corneum

The specific resistivity of human forearm epidermis ρ_{epi} is 0.77 to 1.7x10^6 ohm-m [82,83], but independent resistivities for the stratum corneum and the barrier layer are not known. To estimate them, assume that (in the absence of sweat gland activity),

$$R_{epi} = R_{sc} + R_{bar}$$

where R_{sc} is the resistance of the stratum corneum, and R_{bar} that of the barrier. Then, by Equation 2,

$$\frac{\rho_{epi} t_{epi}}{A_{epi}} = \frac{\rho_{sc} t_{sc}}{A_{sc}} + \frac{\rho_{bar} t_{bar}}{A_{bar}}$$

Since $A_{epi} \cong A_{bar} \cong A_{sc} \cong areae$, the area of the electrode,

$$\rho_{sc} = \frac{\rho_{epi} t_{epi} - \rho_{bar} t_{bar}}{t_{sc}} \tag{3}$$

and

$$\rho_{bar} = \frac{\rho_{epi} t_{epi} - \rho_{sc} t_{sc}}{t_{bar}}$$

The resistivities ρ_{bar} and ρ_{sc} are thus determined by the relative thicknesses of the epidermis, the permeability barrier and the rest of the stratum corneum. The range of thickness of the epidermis was known, and the thickness of the stratum corneum t_{sc} was taken as the difference between it and the estimated barrier thickness, i.e. $t_{sc} = t_{epi} - t_{bar}$.

t_{bar} in μm)		ρ_{bar} (MΩ-m)					ρ_{sc} (MΩ-m)				
$\rho_{bar} > \rho_{sc}$	4.0	4.4	6.2	8.0	9.8	11.6	0.9	0.7	0.5	0.3	0.1
$\rho_{bar} > \rho_{sc}$	10.0	2.3	2.9	3.5	4.1	4.7	0.9	0.7	0.5	0.3	0.1
$\rho_{bar} = \rho_{sc}$	B	.77	1.02	1.27	1.52	1.77	.77	1.02	1.27	1.52	1.77

Table 4: *Variable values for ρ_{bar} and ρ_{sc}. ρ_{sc} is a function of t_{epi}, t_{bar}, t_{sc} and ρ_{epi}, and varies with them. The middle column of ρ_{bar} (8.0, 3.5 and 1.27) are base values. 'B' denotes 'both'.*

The relation of ρ_{bar} and ρ_{sc} was also constrained by the gradient of permeability in the epidermis. If barrier function is uniformly distributed throughout the stratum corneum [37,80], then ρ_{sc} equals ρ_{bar}. If instead the primary permeability barrier is located near the dermo-epidermal junction [40,41,43], then ρ_{bar} must be greater than ρ_{sc}. Equation 3 was used to plot ρ_{sc} versus ρ_{bar} (Figure 18) for the two values of t_{bar}, using structural dimensions estimated below (see Section 5.4.5). The midpoint coordinates were used for the base resistivity in each case. The base values and ranges of variation of ρ_{bar} and ρ_{sc} for the two values of t_{bar} are tabulated in Table 4.

5.4.3 Constraints on the resistivity of the epidermal duct wall

The electrical resistivity of the duct wall is not known but is probably high. The duct, which cornifies at the same level as the rest of the skin, maintains its integrity under pressure in miliaria crystallina, a dermatologic condition in which superficial obstruction of the duct traps sweat in the stratum corneum [72,73]. Physical blockage of the epidermal duct by the action of antiperspirants creates a

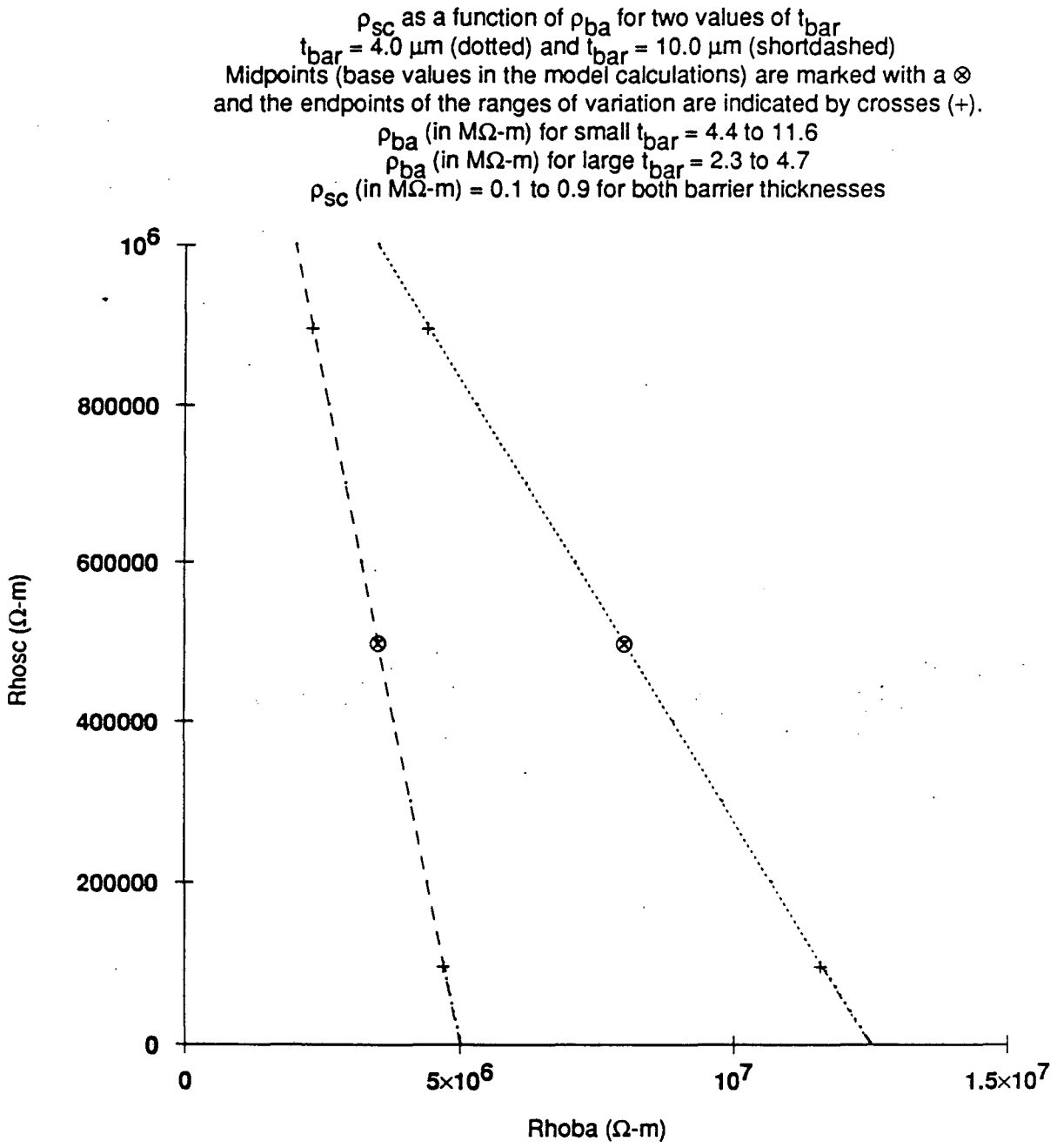

Figure 18: *The variation of ρ_{sc} as a function of ρ_{bar}*

similar condition [74,84]. This impermeability to water implies a barrier to ionic mobility. Finally, iontophoretically driven dye travels down past the epidermal duct lumen and out through the dermal duct wall [85]. On the basis of this evidence, the resistivity of the dermal duct wall ρ_{du} was chosen so that the calculated duct wall resistance R_d was of the same order of magnitude as the total epidermal resistance $(R_e + R_b)$ and at least a factor of 100 times that of the electrolyte R_s. This condition held for all the data sets represented, with the base value of ρ_{du} set at 50.0 KΩ-m and its range of variability 3.0 to 7.0 KΩ-m.

5.4.4 Formulas for the resistances of skin structures

The formulae for model resistances are:

for the resistance of the stratum corneum

$$R_e(in\ \Omega) = \frac{\rho_{sc} t_{sc}}{areae}$$

for the resistance of the barrier layer

$$R_b(in\ \Omega) = \frac{\rho_{bar} t_{bar}}{areae}$$

for the resistance of the epidermal duct wall

$$R_d(in\ \Omega) = \frac{\rho_{du} t_{duct}}{\pi d_{duct} t_{sc}(rlf)}$$

and for the resistance of the fluid in the duct

$$R_s(in\ \Omega) = \frac{\rho_{el} t_{sc}(rlf)}{\pi (d_{duct}/2)^2}$$

where $areae$ is the area of the electrode, t_{duct} is the thickness of the epidermal duct wall, d_{duct} is the average diameter of epidermal duct, and rlf is a 'real length factor'

to compensate for the epidermal duct not being a straight tube. The resistivity of 0.77 mM NaCl, the electrolyte used in all measurements, was ρ_{el} = 1.25 ohm-m [86]. As discussed in Section 5.4.2, ρ_{sc} was a function of ρ_{bar}.

5.4.5 Structural dimensions

The values used for the dimensions of skin structures, along with their range of variation, are:

1. The thickness of the epidermis (t_{epi}) used by Yamamoto and Yamamoto in their determination of ρ_{epi} was 40 μm [82,83], a value also cited by Schaefer with reference to permeability studies [80]. The range of variation used in the model was 30 to 50 μm.

2. Two estimates for the thickness of the barrier layer (t_{bar1} and t_{bar2}) were obtained from studies on pig skin, which has a corneal structure and a permeability similar to that of human skin [87]. The physical thickness of a permeability barrier isolated from trypsinized pig ear (corneal thickness 42-45 μm) was approximately 4.0 μm [41]. The barrier as visualized by the limits of horseradish peroxidase (HRPO) permeation in pig belly (corneal thickness 69$\pm$4 μm) was 16$\pm$1 μm thick [43]. Since the ratio of the mean permeability constants measured for HRPO and water was 1.5 or greater [43], the barrier thickness with respect to small ions was estimated as 10 μm. Both estimates were used in the model.

3. The base diameter of the epidermal duct was 25 μm, with a range of 15-35 μm) [88].

4. The thickness of the epidermal duct wall was estimated from electron micrographs [89] to be about 3 μm (1-5 μm).

5. The area of the electrode is the measured diameter (3.0 mm^2, 2.5-4.5 mm^2) of the area wetted in alcohol-dehydrated skin by an electrolyte droplet of the volume used in the experiment.

6. The 'real length' factor = 2.5 (1-5) is a multiplicative constant to take into account that the duct is probably not a simple vertical tube through the stratum corneum.

5.4.6 Choice of values for voltage sources

Henderson's equation was used to estimate the maximum value (approximately 7.0 mV) for the junction potential (E_j) between the sweat and the electrolyte. The potential across the epidermal duct wall (E_d) was not known, but if the epidermal duct wall acts as a semipermeable barrier, then under the conditions of the experiment any potential across the duct wall will be less than or equal to E_j. Since the potentials E_d and E_j appear only as a sum in the denominator of Equation 1, they are lumped together as the potential E_t = 14 mV. The range used for E_t was -2 to +14 mV.

A potential of E_b = -40 mV (range -40 to -60 mV) was assigned to the barrier layer on the following basis:

- The skin potential level in an individual with a unilateral sympathectomy was -35 mV on the deinnervated side and -45 mV across 'normal' skin [53].

t_{bar1}	t_{bar2}	$areae$	t_{epi}	rlf	t_{duct}	d_{duct}	ρ_{du}	E_b	E_t
μm	μm	mm^2	μm	-	μm	μm	$K\Omega$-m	mV	mV
6.0	11.0	4.5	30.0	1.00	5.0	15.0	70.0	20.0	-2.0
5.0	10.0*	4.0	35.0	1.25	4.0	20.0	60.0	30.0	2.0
4.0*	9.0	3.5*	40.0*	1.50*	3.0*	25.0*	50.0*	40.0*	6.0
3.0	8.0	3.0	45.0	1.75	2.0	30.0	40.0	50.0	10.0
2.0	7.0	3.5	50.0	2.00	1.0	35.0	30.0	60.0	14.0*

Table 5: *Variable values. (*) denotes a base value.*

- After sweat gland activity is eliminated by pharmacological means, the transdermal potential is in the range of -20 to -40 mV [56].
- The skin potential level in a habituated subject (when gland activity is absent) ranges between -30 and -50 mV [90].

5.5 Behavior of the model

5.5.1 Potential as a function of the number of glands

The behavior of the model is illustrated by plots of potential versus number of glands (Figures 19 through 29). Each plot represents the result of varying one parameter with all others set at a base value. Since there are two barrier thicknesses and two possible relations of ρ_{bar} and ρ_{sc}, there are four plots for every parameter except t_{bar} and t_{sc} (which have two apiece), and ρ_{bar} and ρ_{sc} (which each have one). All plots have the form $1 - e^{-\gamma n}$ where n is the number of eccrine glands, with the

potential showing an exponential dependence on the number of glands 'seen' by the electrode. The change in potential per gland is greatest when the number of glands is small, and decreases rapidly as the number of glands increases. The absolute value of the potential is represented rather than its actual (negative) value. The values substituted into the potential equation (Equation 1) for all parameters are tabulated in Table 5.

The plots fell into two groups: (1) potential changes due to variations in source values (represented by Figures 28 and 29); and (2) potential changes due to variation of dimensional factors (Figures 19 through 27). The interpretation of the first group is straightforward: changes in E_b act as an offset and shift the curves vertically; and changes in E_t change the slope of the exponential curve as well as its asymptotic value. The second group can be divided into three catagories:

- In the first category (Figures 21, 24, and 25), potential increased as the parameter (ρ_{epi}, t_{epi}, rlf, or d_{duct}) increased.

- In the second, the potential decreased as the parameter (ρ_{duct}, t_{duct}, areae, t_{bar}, and ρ_{bar}) increased (Figures 19, 22, 23, 26, and 27).

- In the third (Figure 20), the variation of ρ_{epi} with $\rho_{bar} > \rho_{sc}$, the potential stayed the same as the parameter varied. This is a degenerate case that occurs due to the coupling of ρ_{bar} and ρ_{sc}[29].

[29]Since ρ_{bar} is fixed, changes in ρ_{epi} change ρ_{sc} linearly (Equation 3). However, the only model resistance that has ρ_{sc} as a factor is R_e. V_n thus becomes a linear function of a single variable (ρ_{sc}). The same is not true for t_{epi}, t_{bar} and ρ_{bar}, the other factors in Equation 3: Since both t_{epi} and t_{bar} appear in the denominator as well as the numerator, the variation is nonlinear; and if ρ_{sc} varies with ρ_{bar}, then both R_e and R_b are affected.

Plot #	Factor varied	ρ_{bar} vs ρ_{sc}	t_{bar}	9-pt Slope (mV/gland)	Spread (mV)	ψ	Representative plot
1	ρ_{bar1}	>	t	.267 - .368	6.19	↘	Figure 19
2	ρ_{bar2}	>	T	.260 - .367	6.50	↘	Figure 19
3	ρ_{epi}	>	t	.339*	0	≡	Figure 20
4	" "	=	t	.174 - .288	1.08	↗	Figure 21
5	" "	>	T	.354*	0	≡	Figure 20
6	" "	=	T	.198 - .312	1.25	↗	Figure 21
7	ρ_{du}	>	t	.278 - .363	1.86	↘	Figure 22
8	" "	=	t	.153 - .266	0.96	↘	Figure 23
9	" "	>	T	.303 - .368	2.06	↘	Figure 22
10	" "	=	T	.175 - .291	1.11	↘	Figure 23
11	*areae*	>	t	.320 - .366	1.43	↘	Figure 22
12	" "	=	t	.194 - .276	0.79	↘	Figure 23
13	" "	>	T	.339 - .368	1.59	↘	Figure 22
14	" "	=	T	.219 - .300	0.89	↘	Figure 23
15	t_{bar1}	>	V	.203 - .368	8.15	↘	Figure 19
16	" "	=	V	.211 - .226	0.13	↘	Figure 23

Table 6: *Nine-point range and spread of modelling plots. Barrier thicknesses are 'T' = 10.0 μm, 't' = 4.0 μm, and 'V' if t_{bar} varies. Potential (ψ) increased (↗), decreased (↘), or stayed the same (≡) as the parameter increased. Starred (*) values did not change.*

Plot #	Factor varied	ρ_{bar} vs ρ_{sc}	t_{bar}	9-pt Slope (mV/gland)	Spread (mV)	ψ	Representative plot
17	t_{bar2}	>	V	.299 - .367	1.90	↘	Figure 22
18	" "	=	V	.231 - .249	0.17	↘	Figure 23
19	t_{epi}	>	t	.244 - .368	5.95	↗	Figure 24
20	" "	=	t	.158 - .303	1.40	↗	Figure 21
21	" "	>	T	.193 - .362	8.34	↗	Figure 24
22	" "	=	T	.175 - .334	1.82	↗	Figure 21
23	*rlf*	>	t	.308 - .366	1.65	↗	Figure 25
24	" "	=	t	.180 - .275	0.87	↗	Figure 21
25	" "	>	T	.329 - .368	1.81	↗	Figure 25
26	" "	=	T	.204 - .300	1.01	↗	Figure 21
27	t_{duct}	>	t	.197 - .368	3.15	↘	Figure 26
28	" "	=	t	.095 - .290	1.60	↘	Figure 27
29	" "	>	T	.222 - .367	3.50	↘	Figure 26
30	" "	=	T	.111 - .313	1.85	↘	Figure 27

Table 7: *Nine-point range and spread of modelling plots (continued) . Barrier thicknesses are 'T' = 10.0 μm, 't' = 4.0 μm, and 'V' if t_{bar} varies. Potential (ψ) increased (↗), decreased (↘), or stayed the same (≡) as the parameter increased. Starred (*) values did not change.*

The mean number of glands subtended by 3.0 mm^2 (the electrode area) was $\overline{X}$ = 9.09375, so the slope of a curve at this 'nine-point' was a measure of the sensitivity of the potential to a particular parameter value. The maximum nine-point slope, $d\psi/d(gland)_{n=9}$ = 0.368 mV/gland, occurred during the variation of eight out of the nine dimensional parameters (see Tables 6, 7, and 8). The spreading of a particular curve family (where spread was the amount of line separation at n = 20 glands), was an additional measure of sensitivity; a wide spread (such as in Figure 24, where spread = 8.34 mV) indicated that the particular parameter was strongly affective, whereas closely-spaced lines (for example, Figure 23, with spread = 0.96 mV) demonstrated that the effect of the factor was small. Each of the curve shapes is illustrated by a representative plot (Figures 19 through 29) and the ranges of nine-point slopes and the spreads of the various curve families are tabulated in Tables 6, 7, and 8.

5.5.2 Potential as a function of barrier properties

As discussed in Chapter 2, the other source of potential is probably the epidermal permeability barrier. The model provides two arguments in favor of this hypothesis. The first is that in the plots of potential versus number of glands the most sensitive parameters in terms of spread (excluding E_b and E_t) were ρ_{bar1}, ρ_{bar2}, t_{bar1}, and t_{epi}, with $\rho_{bar} > \rho_{sc}$ in all cases (Tables 6 and 7). All these factors are associated with the barrier layer. Secondly, if all current paths through glands are omitted from the model circuit (Figure 17) so that only Path 4 (which goes directly through the hydrated stratum corneum) is left, then the general expression for the

Plot L #	Factor varied	ρ_{bar} vs ρ_{sc}	t_{bar}	9-pt Slope (mV/gland)	Spread (mV)	ψ	Representative plot
31	d_{duct}	>	t	.301 - .368	2.08	↗	Figure 25
32	" "	=	t	.173 - .290	1.11	↗	Figure 21
33	" "	>	T	.323 - .367	2.28	↗	Figure 25
34	" "	=	T	.197 - .314	1.28	↗	Figure 21
35	E_b	>	t	.339*	40.0	↗	Figure 28
36	" "	=	t	.218*	40.0	↗	Figure 28
37	" "	>	T	.355*	40.0	↗	Figure 28
38	" "	=	T	.244*	40.0	↗	Figure 28
39	E_t	>	t	-.048 - .339	12.63	↗	Figure 29
40	" "	=	t	-.031 - .218	14.48	↗	Figure 29
42	" "	>	T	-.056 - .355	12.12	↗	Figure 29
42	" "	=	T	-.035 - .244	14.21	↗	Figure 29

Table 8: *Nine-point range and spread of modelling plots (continued). Barrier thicknesses are 'T' = 10.0 μm, 't' = 4.0 μm, and 'V' if t_{bar} varies. Potential (ψ) increased (↗), decreased (↘), or stayed the same (≡) as the parameter increased. Starred (*) values did not change.*

potential (Equation 1) reduces to

$$V_n = R_m i_2 = \frac{R_m[E_b]}{R_m + R_e + R_b}.$$

Since $R_m \gg R_e + R_b$, $V_n \cong E_b$. In the absence of gland contributions, the transdermal potential is equal to potential generated across the barrier.

In the model, E_b is an 'ideal battery', i.e. it is a source of potential without resistance, capacitance, and so on. In fact, the 'real' E_b probably exists because of the semipermeability of the barrier, and is thus a function of such factors as the specific conductances and equilibrium potentials of the ionic species on either side of the barrier[30]. Significant potentials can in fact be generated across artificial permselective membranes [29,47] and have been used to characterize the charge and transport properties of biomaterials in their natural state [50]. In conclusion, while there is at present no direct experimental evidence that the barrier is the source of potential variation, this could quite plausibly be so.

5.6 Summary of modelling results

The model is not useful for specific predictions, such as the identification of a particular source of potential variation. It does however provide an indication of which structures are important and how many contributing elements are likely to have an influence on the potential. In terms of particular structures, the mean standard deviation of gland counts (for an electrode area of 3 mm^2) was $\overline{\sigma_{gc}} = 3.55$,

[30]For example, the potential difference $\Delta\psi_m$ due to diffusion of HCl across a homogeneous permselective membrane is

$$\Delta\psi_m = \frac{E_{H^+} g_{H^+} + E_{Cl^-} g_{Cl^-}}{g_{H^+} + g_{Cl^-}}$$

where g_i is the specific conductance and E_i is the equilibrium potential [91].

and the maximum nine-point slope (the plot slope when the number of glands was equal to nine) was 0.368 mV/gland. The maximum potential variability predicted by the model is thus ± 1.31 mV, much less than the mean of the measured potential variability $\overline{\sigma_\psi} = 17.41$ mV. In fact, actual gland counts did not correlate with the experimentally measured potential.

If the model is generally correct (and the values substituted are the correct order of magnitude), this suggests that there is little if any contribution from the glands and that there is at least one other source of potential variability. The most likely candidate is the permeability barrier of the skin. If the barrier behaves like a permselective membrane, then changes in the potential across it could be due to regional variations in membrane permselectivity with respect to one or more ionic species. Experimental measurements of diffusion potentials across model systems such as keratinizing cell cultures or 'nude' mouse skin might be a first step in testing this hypothesis.

5.7 Discussion of model

More information about the path of current flow in the skin, the ionic species that constitute the flow, and the permeabilities or resistivities of skin structures (particularily the barrier layer) to various ionic species is necessary to construct a better model. Even so, it would be difficult to avoid simplifying assumptions similar to those made here. Since there is a range of size and functional capacity for the eccrine glands in a given area, the requirement that all gland-associated values are the same is not a good one, but it is hard to avoid without the model circuit becoming unmanageable. Nevertheless, approximations that ignore such

considerations must be made or the advantage of making a model in the first place is lost.

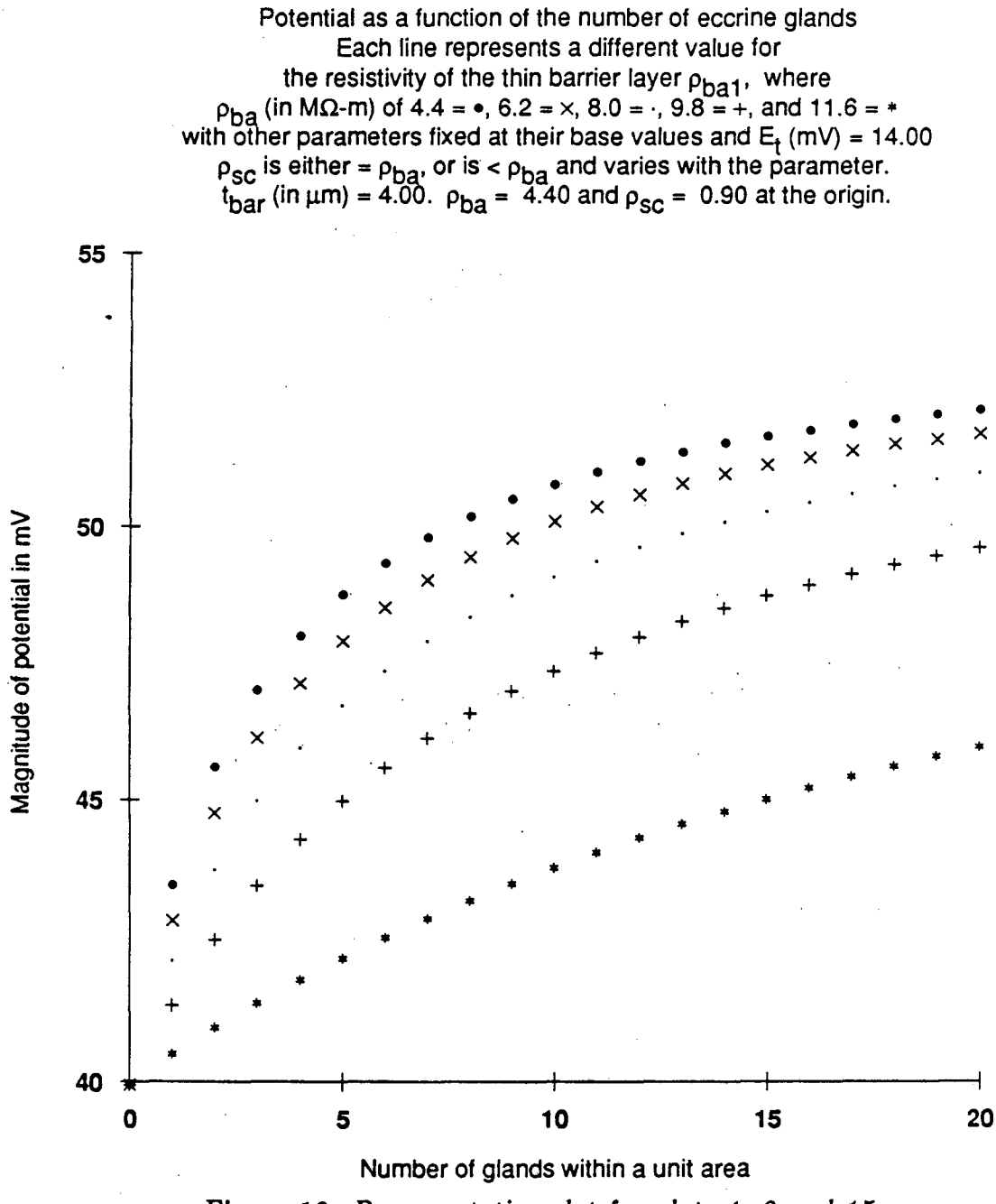

Figure 19: *Representative plot for plots 1, 2 and 15.*

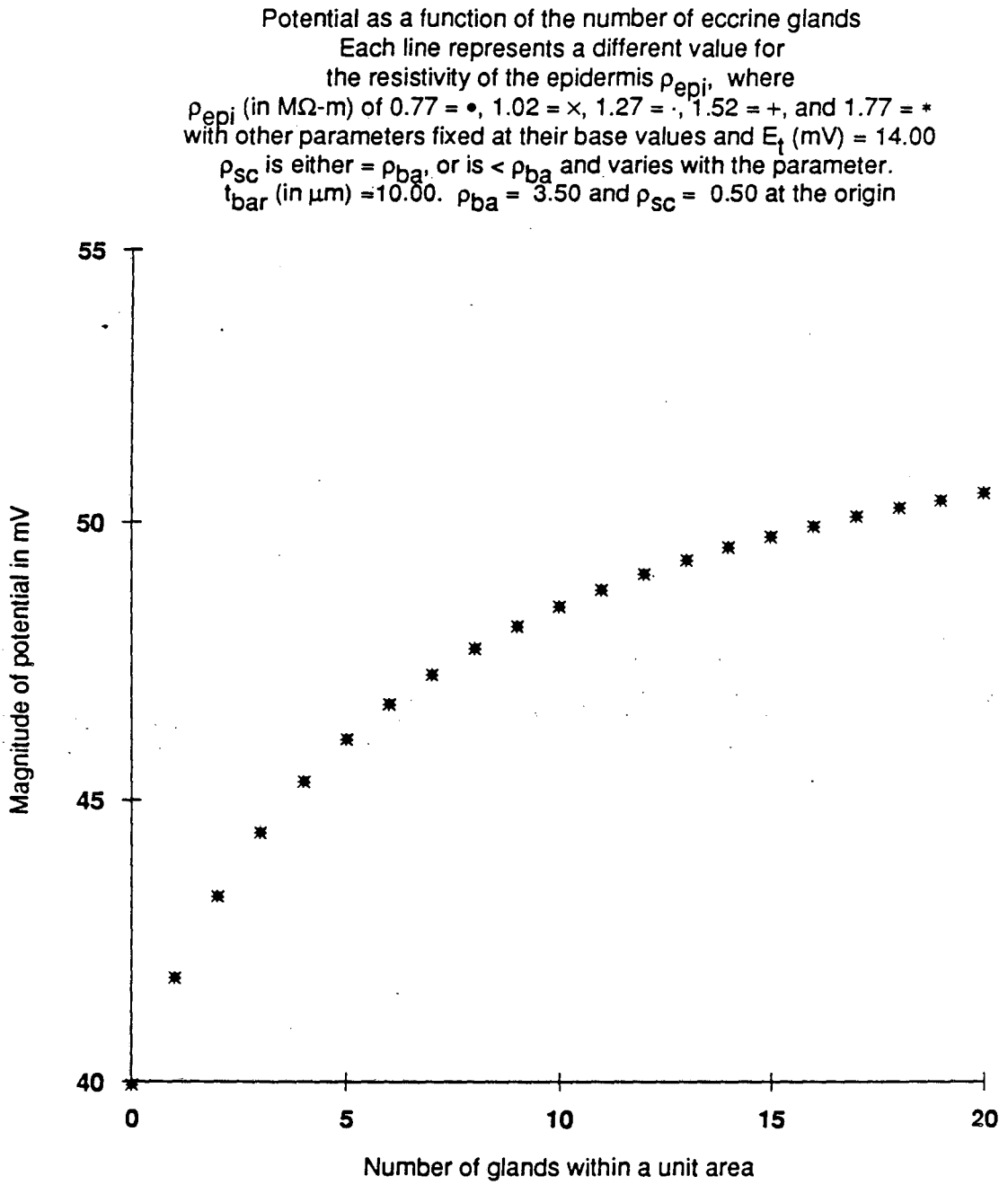

Figure 20: *Representative plot for plots 3 and 5.*

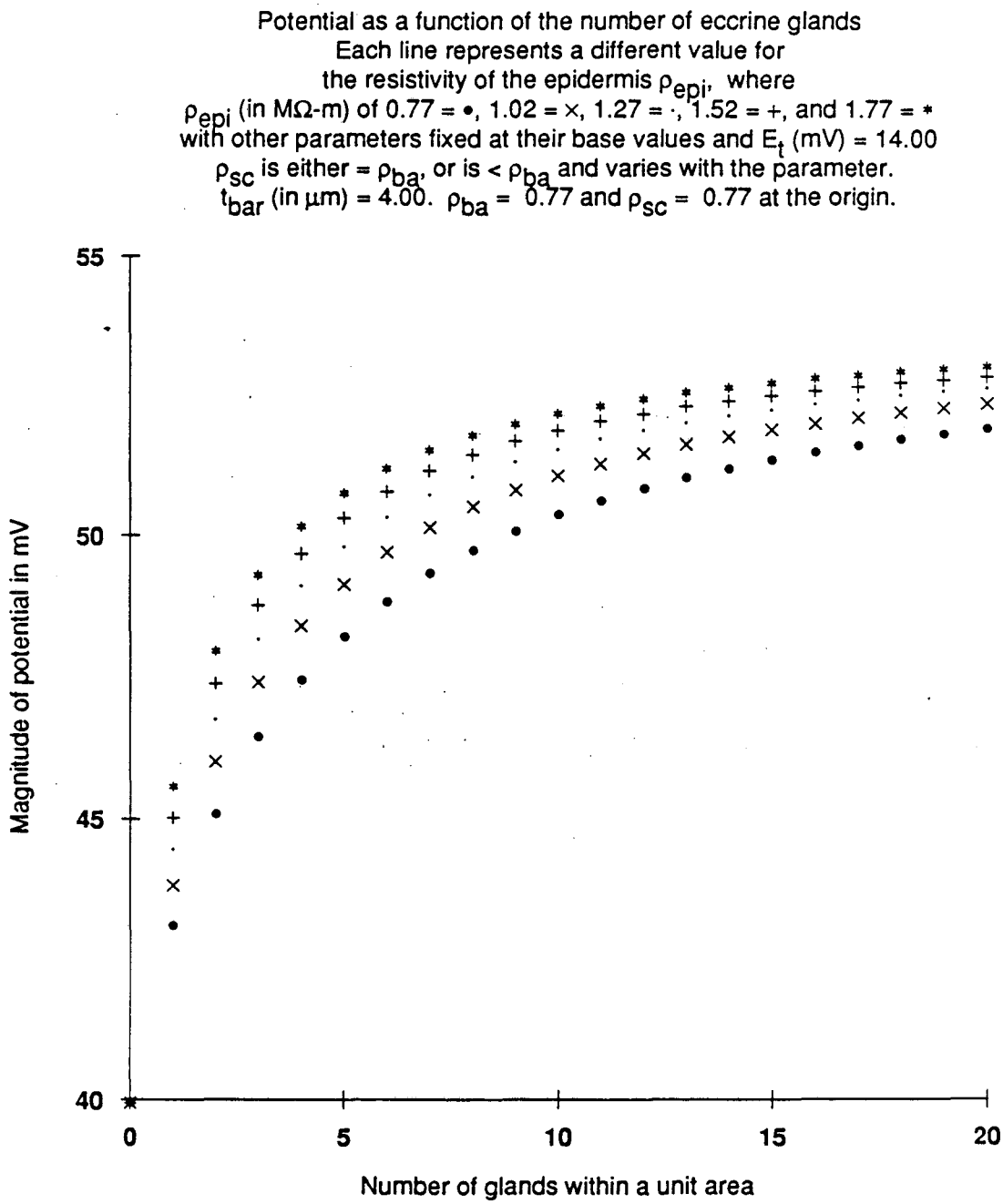

Figure 21: *Representative plot for plots 4, 6, 20, 22, 24, 26, 32, and 34.*

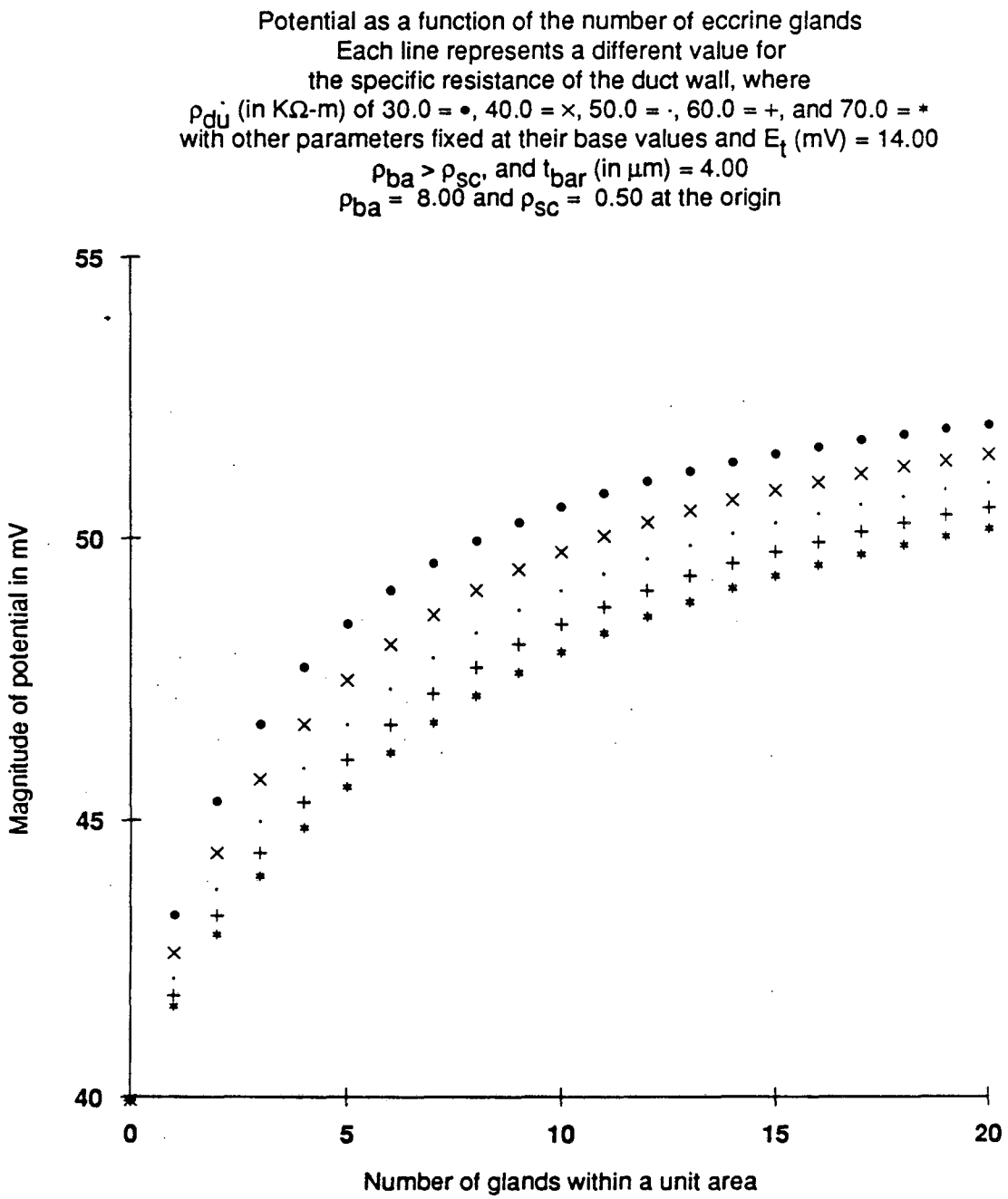

Figure 22: *Representative plot for plots 7, 9, 11, 13, and 17.*

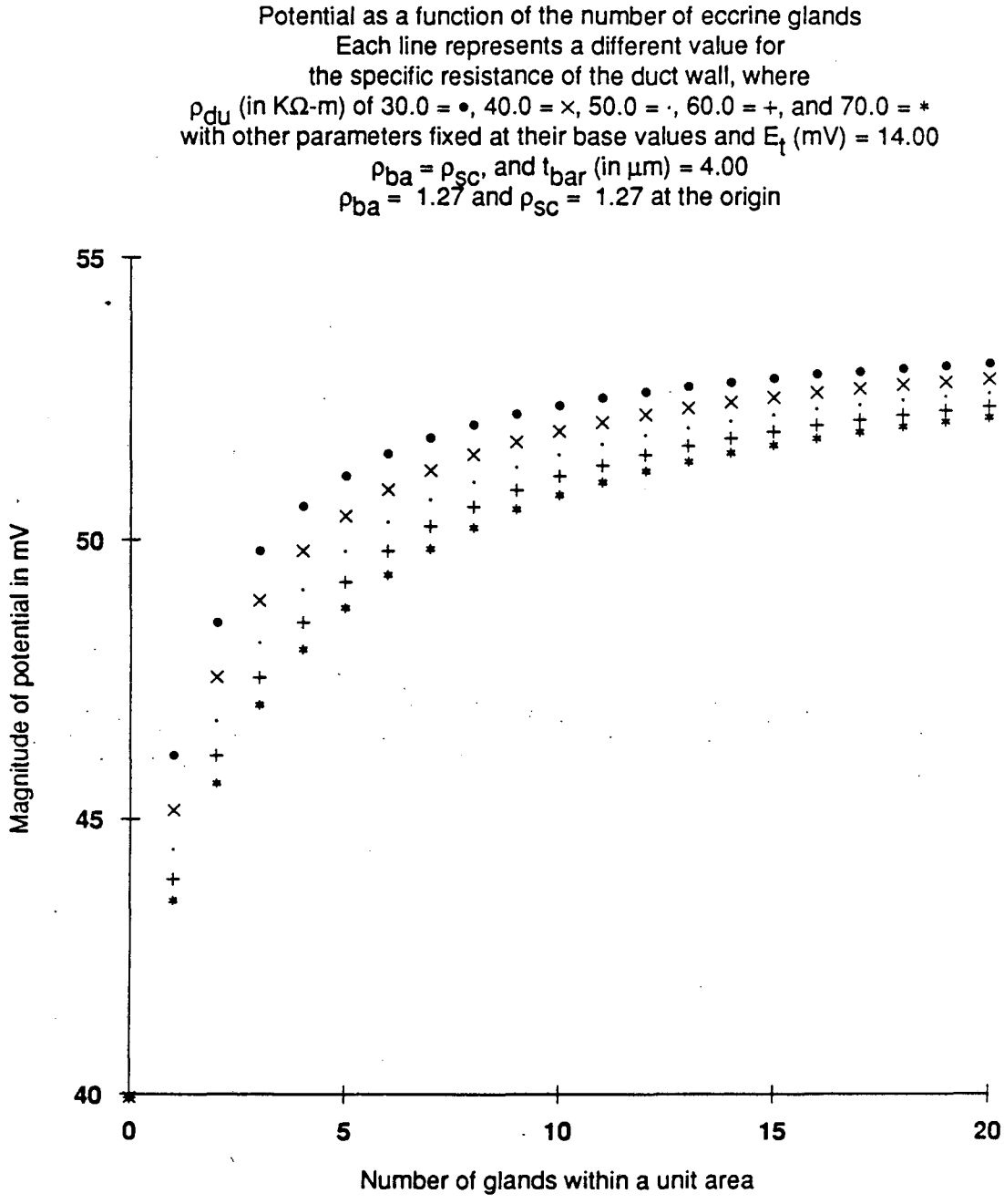

Figure 23: *Representative plot for plots 8, 10, 12, 14, 16, and 18.*

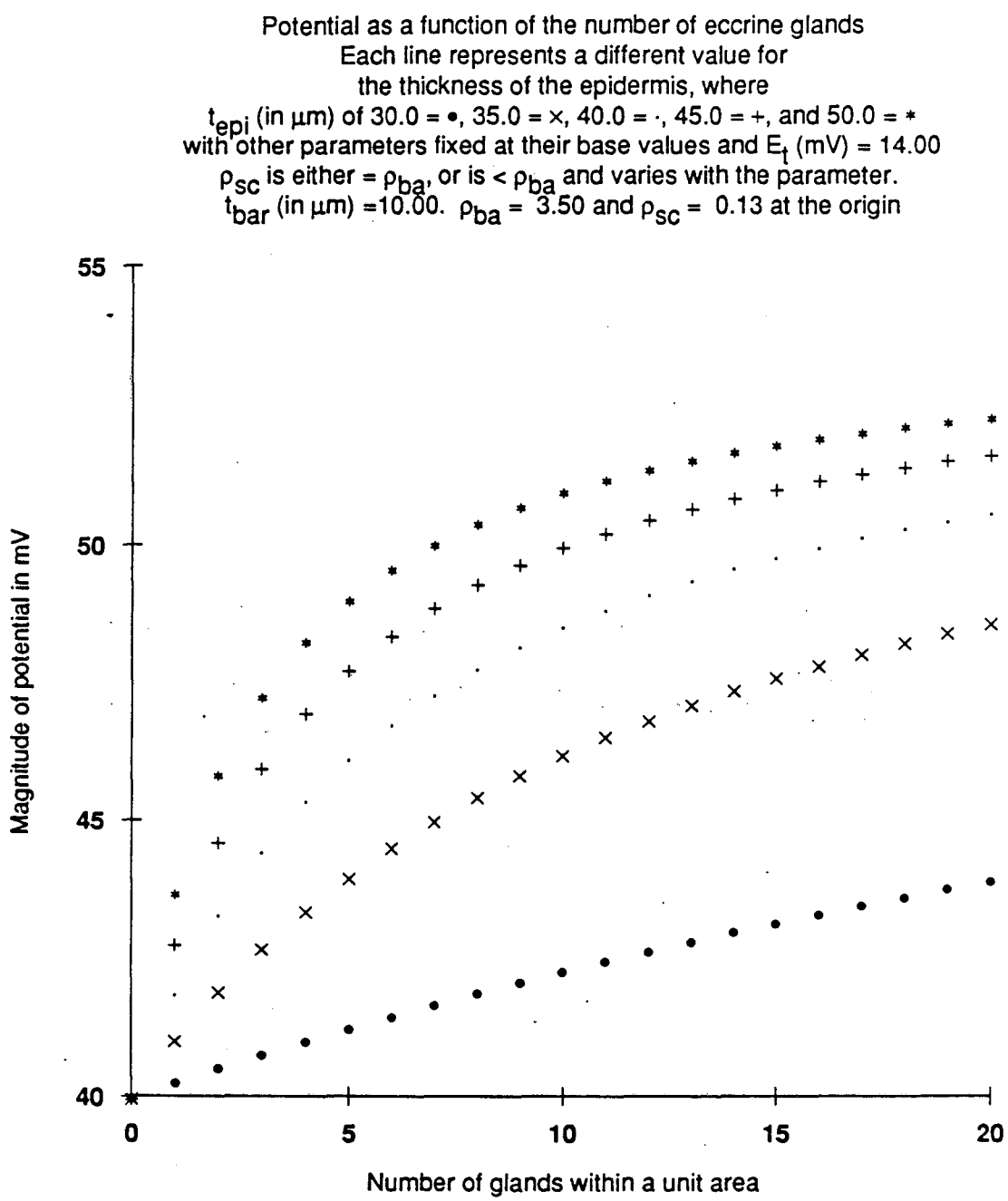

Figure 24: *Representative plot for plots 19 and 21.*

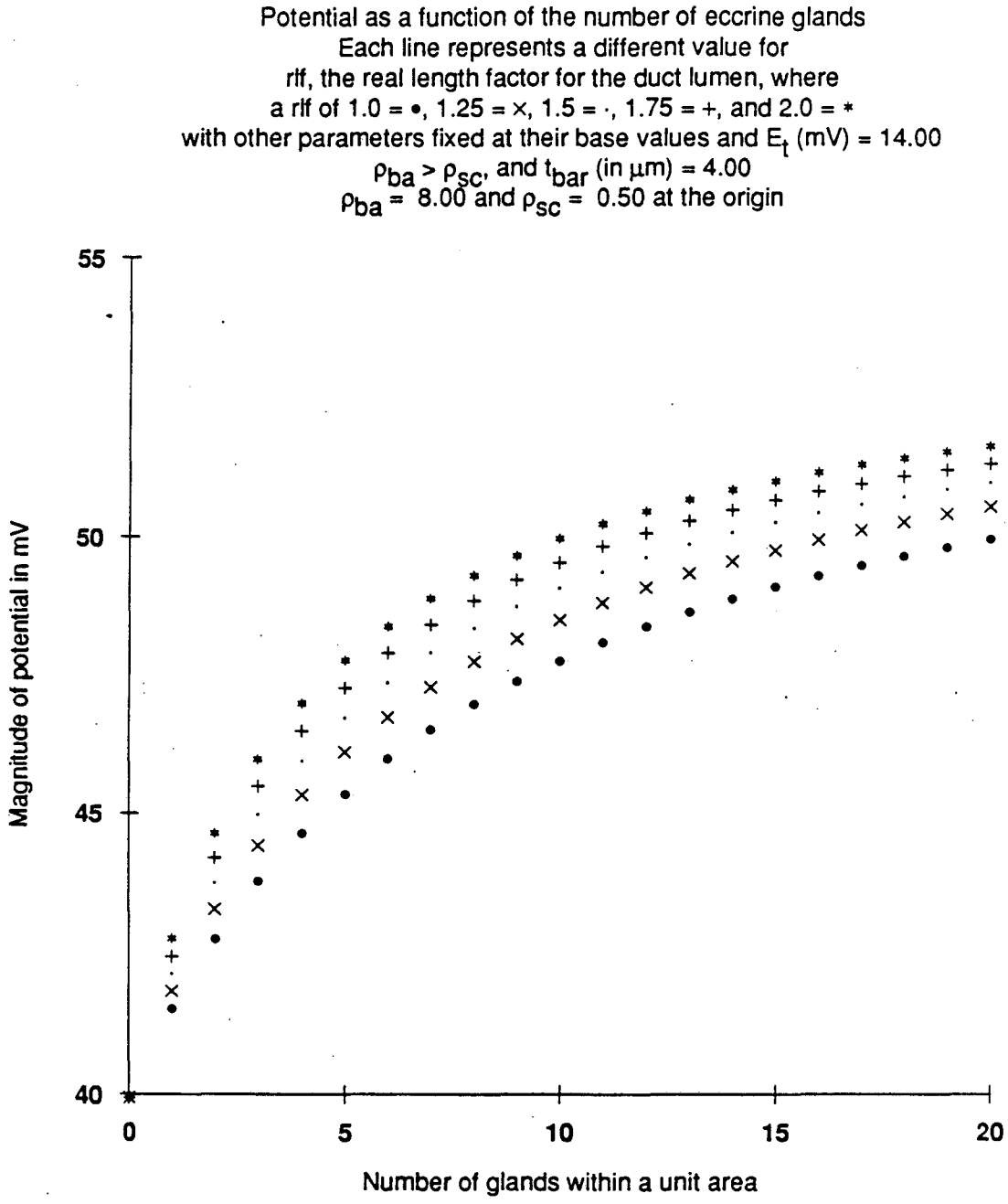

Figure 25: *Representative plot for plots 23, 25, 31 and 33.*

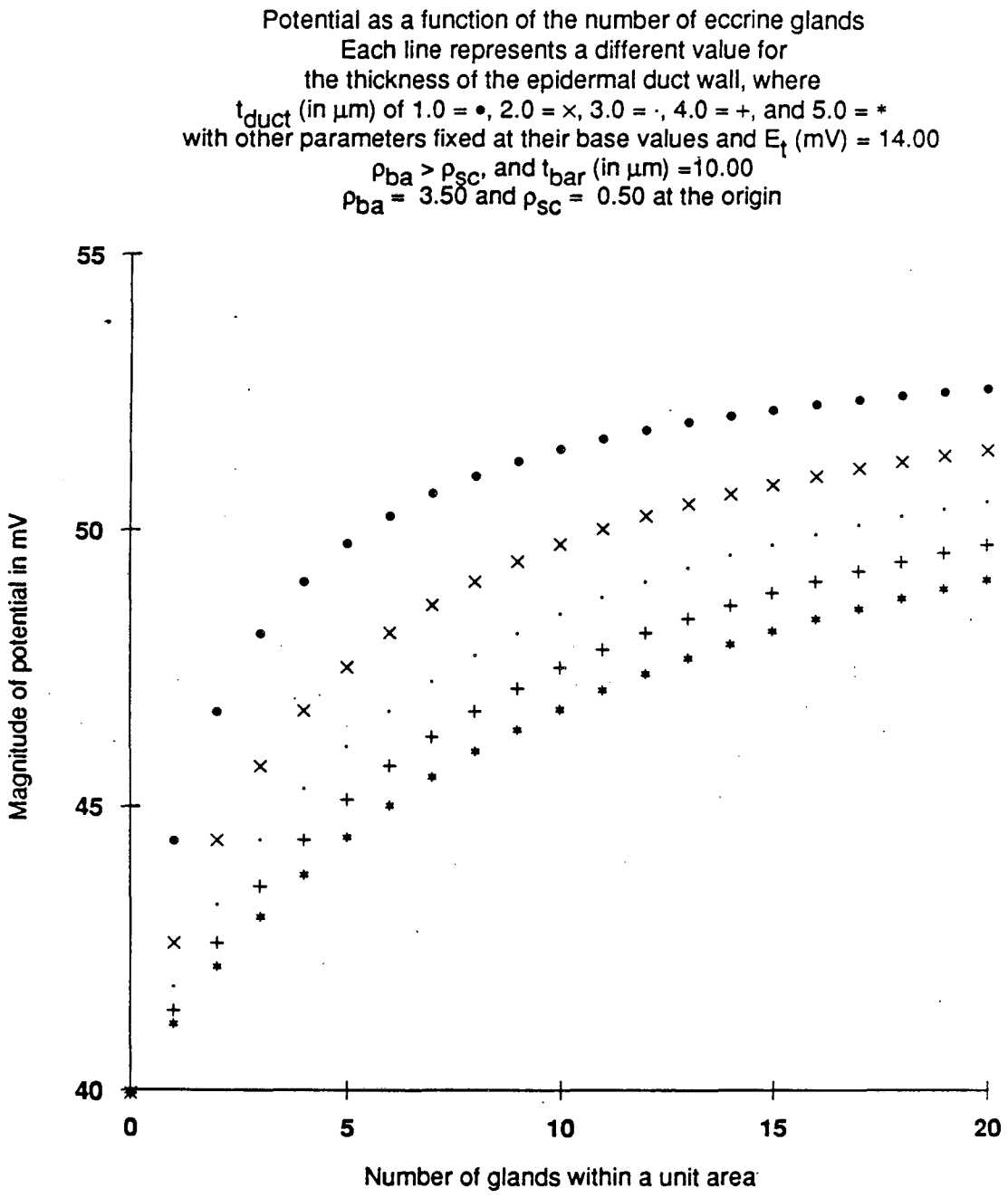

Figure 26: *Representative plot for plots 27 and 29.*

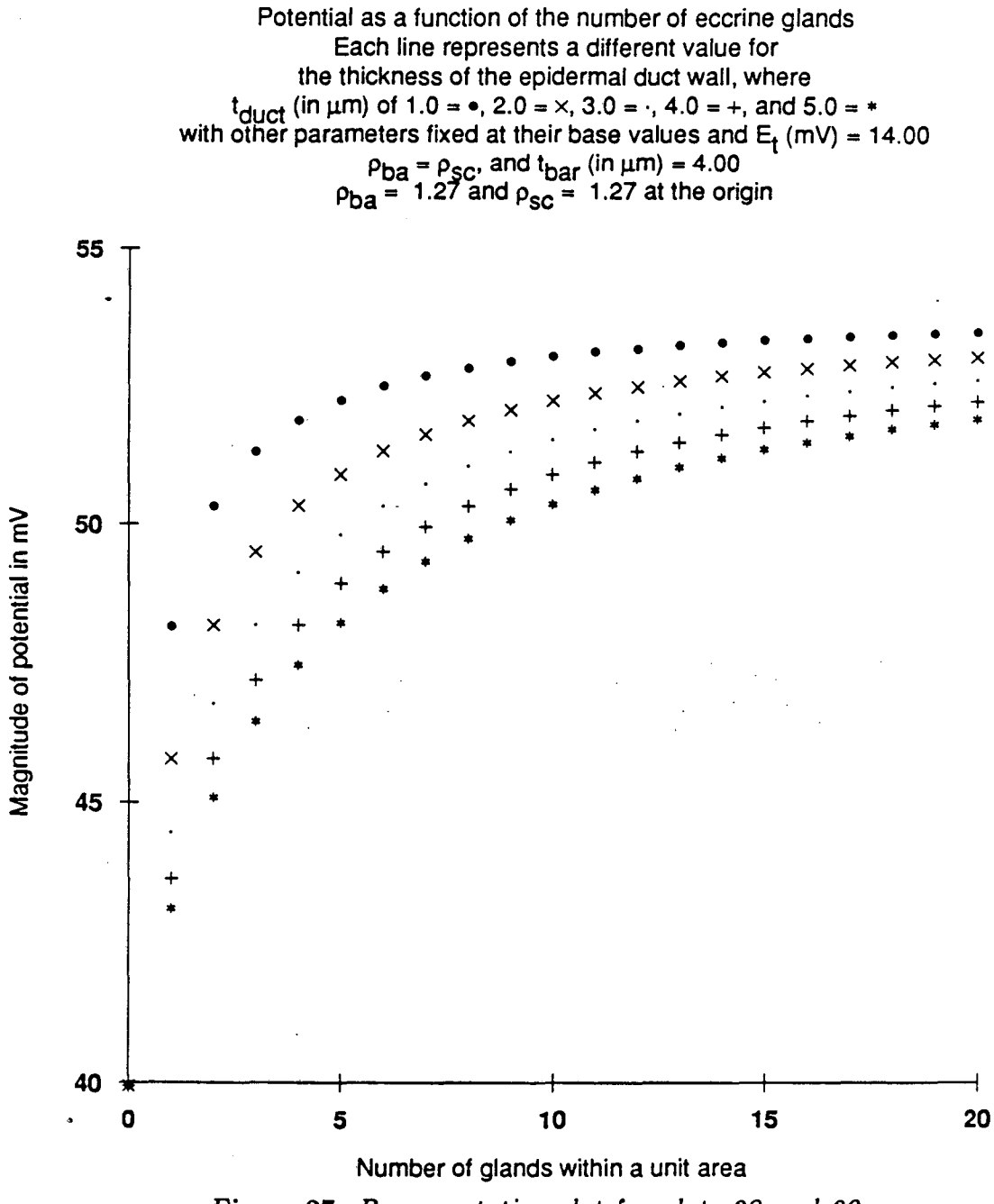

Figure 27: *Representative plot for plots 28 and 30.*

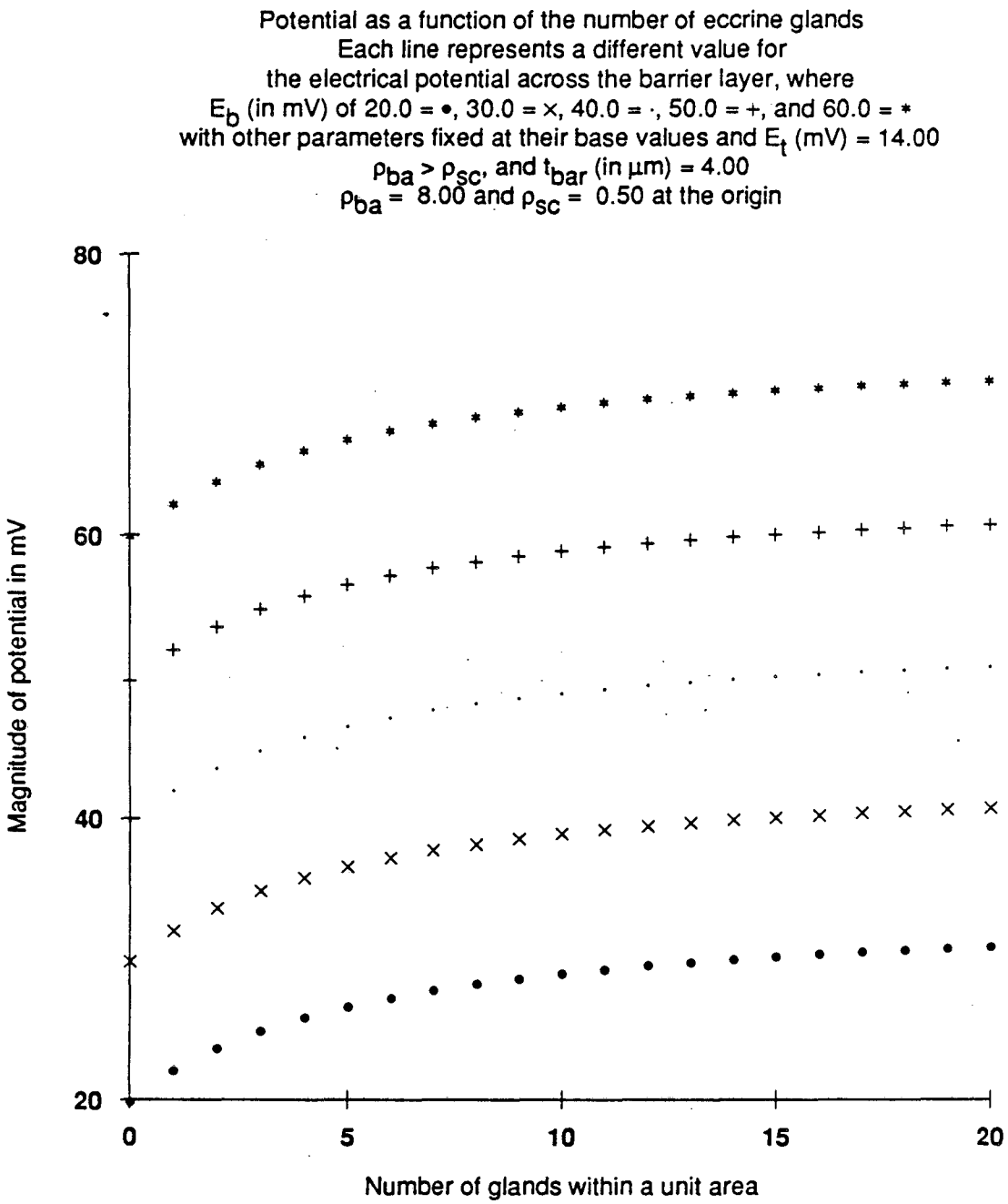

Figure 28: *Representative plot for plots 35 through 38.*

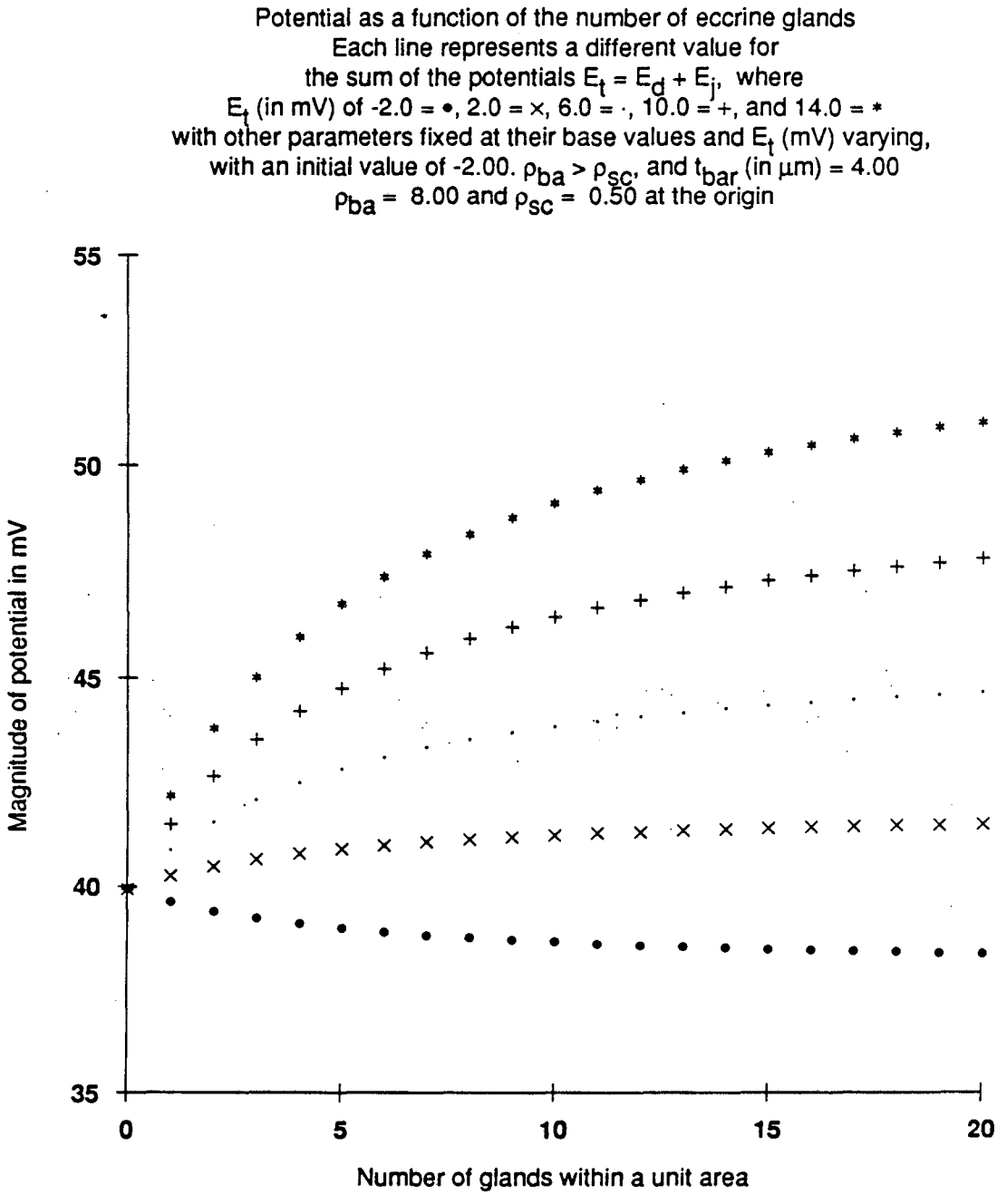

Figure 29: *Representative plot for plots 39 through 42.*

6 Detection of Pore Pattern by Fourier Analysis

6.1 Summary

A spectral analysis of the spatial frequencies present in the eccrine gland location data was made using fast Fourier transform (FFT) techniques (Section 6.2). Radial profiles of the power spectra and autocorrelation estimates demonstrated that the glands were not randomly located on the skin surface, but instead exhibited patterning of two sorts (Section 6.3). The mean modal intergland distance[31] over all the samples was 0.49 mm (with a variance of ±0.043). The distribution of eccrine gland pores has not been quantified before, but this finding is consistent with what is known about skin growth and development (Section 6.4). An additional pattern with a mean separation of 1.84±0.35 mm occurred in most of the data. This pattern, which consisted of roughly circular islands of gland-free skin, may be associated with hair follicles.

Simulations of gland distribution by a stochastic model were used to test and extend the interpretations of the profiles (Sections 6.5 and 6.6). This is apparently the first time that Fourier techniques have been applied to the analysis of point processes of biological origin (Section 6.7). Fourier analysis can provide information about the two-dimensional spatial organization of points accurately and more rapidly than conventional methods, but has the disadvantage of a computational requirement for processing large arrays.

[31]The modal separation is the interpoint distance that occurs most frequently in the distribution.

6.2 Two-dimensional Fourier transform analysis

6.2.1 Theory

Let the spatial transform of a function $f(x,y)$ be $F(u,v)$, i.e.

$$f(x,y) \Leftrightarrow F(u,v),$$

where $\Leftrightarrow$ denotes Fourier transformation. By the Wiener-Khinchin theorem, the transform of the power spectrum $|F(u,v)|^2$ is the complex autocorrelation of $f(x,y)$:

$$|F(u,v)|^2 \Leftrightarrow f(x,y) \otimes f^*(-x,-y) = f(x,y) \odot f^*(x,y),$$

and thus

$$F(u,v)F^*(u,v) \Leftrightarrow f(x,y) \odot f^*(x,y)$$

where $\otimes$ is the convolution operation and $\odot$ is the correlation operation [92,93,94].

To avoid false overlaps in the convolution, the data array must be surrounded by a frame of zero samples (zero-filled), with the frame width on each side equal to half the image dimension in that direction (Figure 30). This is the two-dimensional analog of choosing a period large enough to avoid overlap in the convolution of two one-dimensional waveforms [95]. The sampled image is represented by a two-dimensional lattice in which the original image is repeated over and over. The Fourier method of estimating the autocorrelation thus 'slides' two identical periodic matrices over each other. Contributions to this convolution from 'false' overlaps (also termed 'wraparound artifact') will occur between the left and right as well as the upper and lower portions of the original image unless the the data matrix is augmented with zeros in all directions (Figure 30).

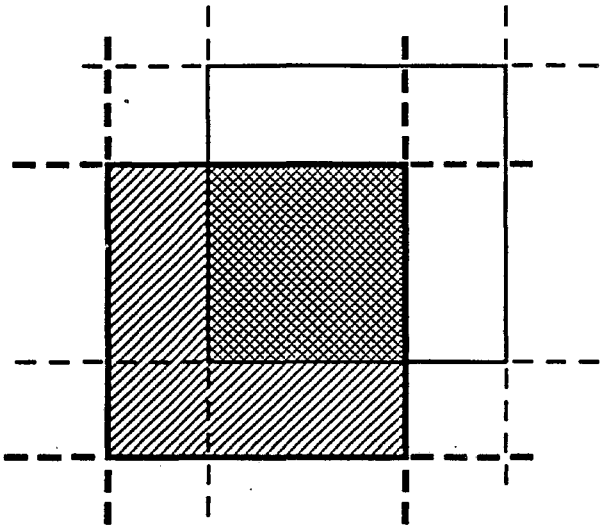

Figure 30: *False overlaps (shaded area) contribute to the autocorrelation (crosshatched area) unless the image is surrounded by a frame of zeros.*

6.2.2 Implementation

Analysis of the gland location data took place in three stages: (1) preparation of the data for transform analysis; (2) forward transformation to determine the power spectrum; and (3) inverse transformation to obtain the autocorrelation estimate. As previously described in Section 4.3, a 512x512 digitized image of each blot disc was used to create a data matrix of the same size in which the (x,y) location of each gland was set to one against a null background. This real array was zero-filled, premultiplied[32] (to shift the transform zero to the center), and then forward transformed. The magnitude of the resultant was stored as the power spectrum (PS). The PS was then inverse transformed and the absolute value of the

[32]Odd rows (1, 3, 5, ...) are multiplied by a vector consisting of +1 −1 +1 −1 ... to negate elements (2, 4, 6, etc.), and even rows (2, 4, 6, ...) are multiplied by a vector consisting of −1 +1 −1 +1 ... which negates elements (1, 3, 5, ...).

resultant real array was stored as the autocorrelation estimate (ACE). The data, PS and ACE matrices were displayed as two-dimensional digital images with pixel brightness proportional to magnitude.

Two versions of the spatial frequency analysis program were used. The first accepted an input matrix of size 1024x1024 and could accomodate the entire dataset. The Fourier transform routines used were Fortran implementations of the FFT algorithms in Brigham [95]. The second, much faster program worked with a subset of the data. This version made use of an Analogic Devices AP400 array processor and its FFT library routines, which limited the input array size to 512x512 but decreased analysis time by a factor of eighty. Apart from the matrix transformations routines employed (and the size of the input matrix), the programs were identical. Both versions were written in FORTRAN 77 and ran on a VAX 11/780 with 4 megabytes of RAM. Program operation was verified using test images (impulse and square) that had predictable power spectra and autocorrelation estimates.

6.2.3 Radial profile representation of the spatial power spectrum and the autocorrelation estimate

Both the PS and the ACE matrices were radially symmetric about image zero (256,256). This made it possible to construct a 'mean radial profile' (Figure 31) of the two-dimensional image. Each profile is an intensity-averaged, normalized sum of all radial slices from the center to the edge of the image along the intensity (Z) axis, with the frequency space index on the X-axis and intensity on the ordinate. These profiles formed the basis of this analysis.

The intensities in the image matrix were radially averaged as follows: The

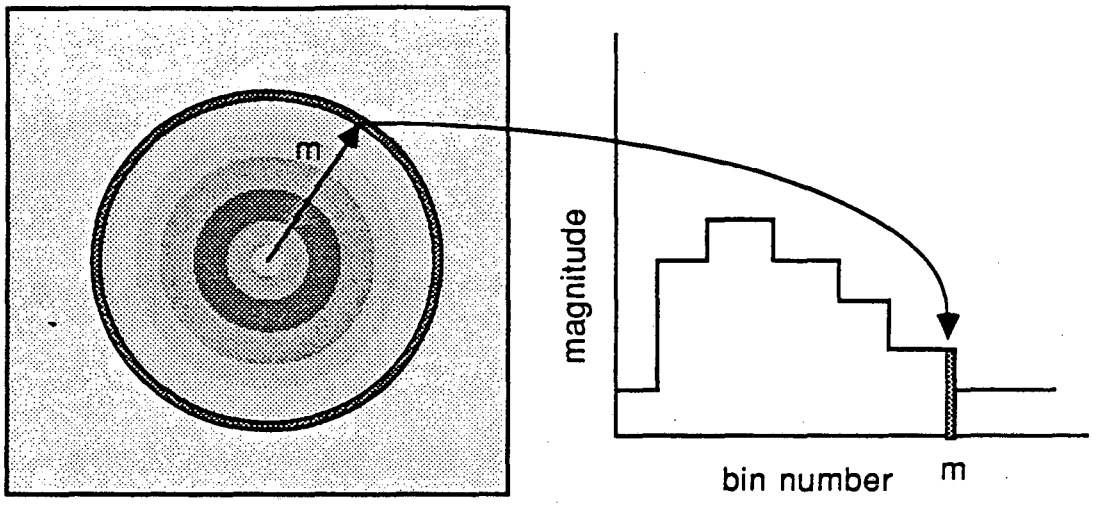

Figure 31: *Each bin in the radial profile represents the mean intensity per pixel at integral radius m in the 2-D image.*

distance from (i,j) to the image center was rounded to the nearest integer m (i.e. there was no interpolation), the intensity at (i,j) was added to bin(m), and count(m) was incremented. Each such integral radius sweeps out a ring of pixels in the PS that have real radii r such that $m - 0.5 < r < m + 0.5$ (Figure 31). The mean intensity at radius m is thus (total intensity in bin(m))/(total count(m)). The number of useful bins was determined by the largest spatial frequency detectable in the discrete transform $u_c = f_s/2 = 512/2 = 256$, where f_s is the Nyquist sampling frequency.

In the power spectrum (Figure 32), the spatial frequency is $u = n/NT$ (where n is the frequency space index[33], N the number of samples, and T the spatial sample interval), thus the inter-pattern spacing $1/u$ in the original data is NT/n

[33]The DC value is in the first bin, so n = (bin number - 1).

or 512/(bin number - 1) mm. For the autocorrelation estimate (Figure 33), a maximum at n indicates that features separated by n in the matrix are highly correlated [96]. In both cases, the DC value (which represents the total power in the PS and corresponds to the inner product of the data array with itself at zero displacement in the ACE) was zeroed before scaling the array for display and computing the radial profile for the analysis[34].

6.2.4 The effects of zero-filling and windowing on the radial profile

Zero-filling of the data arrays was accomplished in two ways. To construct a 1024x1024 input array, the original 512x512 data array was augmented by a 128-pixel wide 'strip' of zero values on each side, the result being a 1024x1024 matrix surrounded by a frame of zero values. The 512x512 input arrays were obtained by multiplying the original data matrix with a unit right rectangular cylinder or 'pillbox' function with $r = 128$, the result being a disk of data points surrounded by zeros exactly similar to (but smaller than) the larger array. Although the smaller matrix had approximately 65% fewer data points than the larger array, the radial profiles of 'large' and 'small' transforms (see Figure 32 and Figure 33) were similar. Since the analysis of a larger array required eighty times the processing time of a small one, the fast version of the analysis was used routinely, with the final analysis of each dataset done using the slow version.

Circular rather than square zero-filling was employed to avoid biasing the radial averages. The transform of the function used for square zero-fill (the unit rectangle $l(x, y)$) is the product of two sinc functions and is not radially symmetric. Since

[34]In the power spectrum, large near-DC values were zeroed as well.

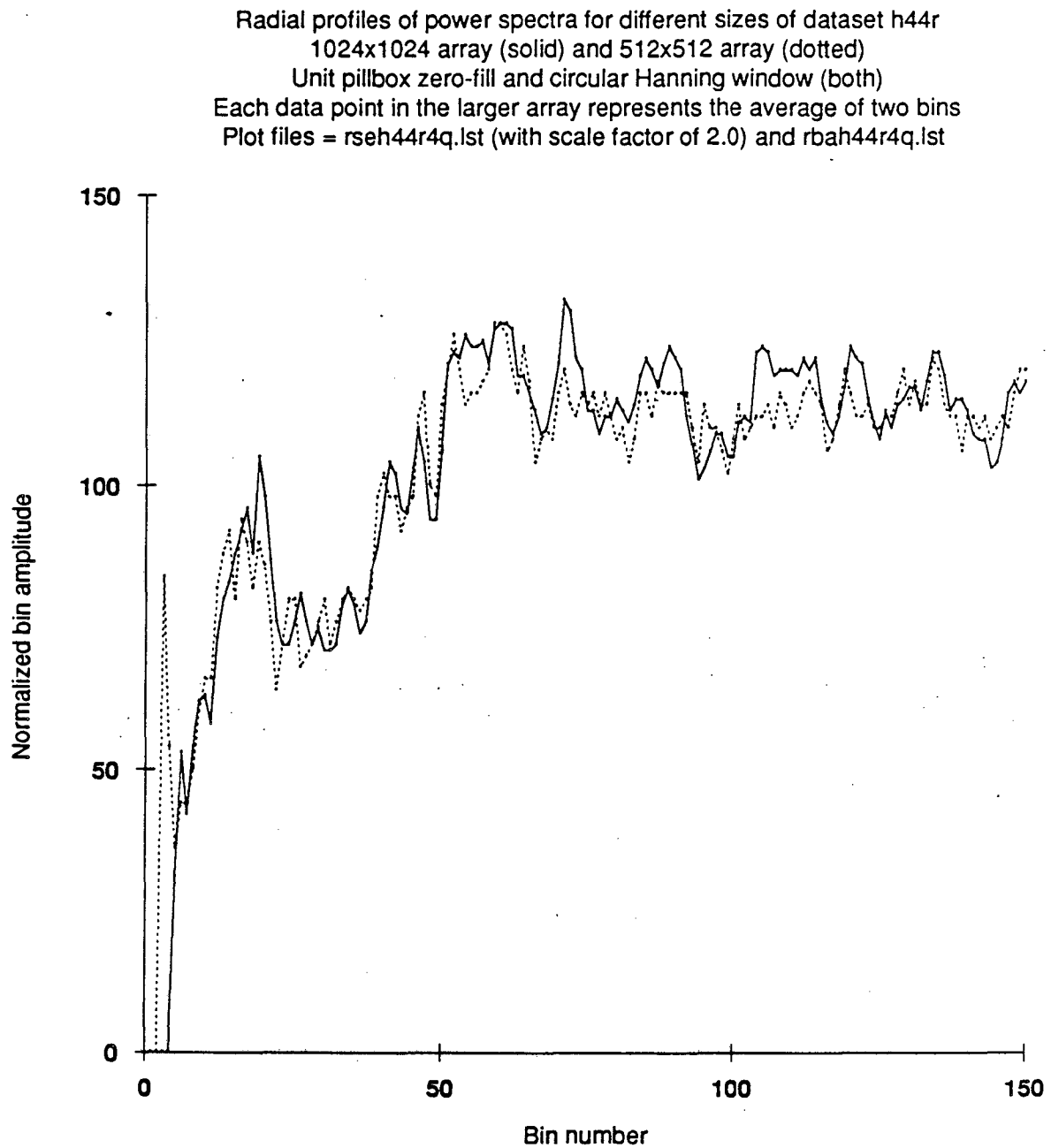

Figure 32: *Comparison of power spectum radial profiles of complete (1024x1024) and reduced (512x512) datasets for sample h44r.*

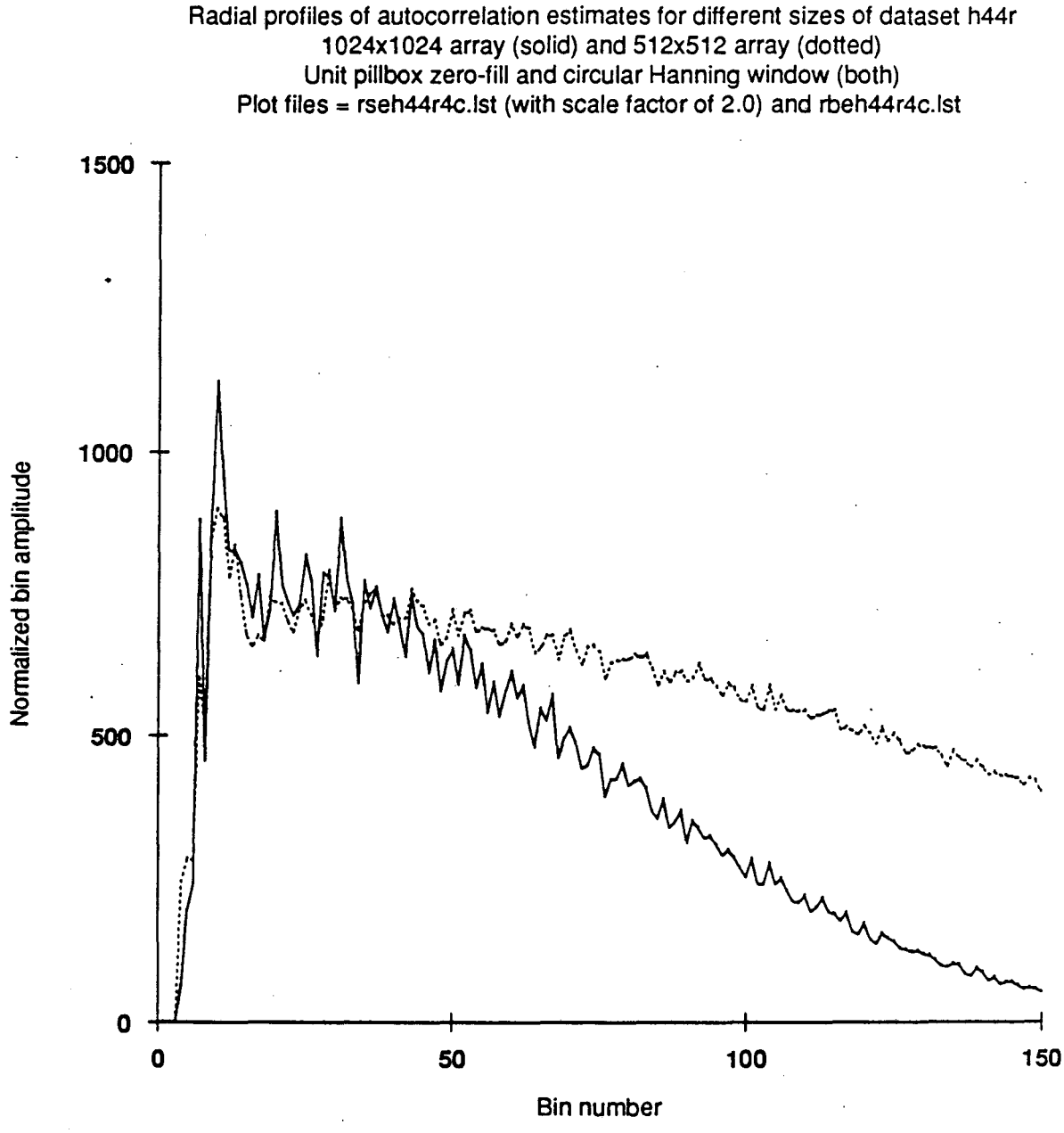

Figure 33: *Comparison of autocorrelation estimate radial profiles of complete (1024x1024) and reduced (512x512) datasets for sample h44r.*

square zero-filling (i.e. square windowing) is equivalent to the convolution of the data array transform with the sinc product

$$f(x,y)l(x,y) \Leftrightarrow F(u,v) \otimes sinc(u)sinc(v),$$

$F(u,v) \otimes sinc(u)sinc(v)$ is not radially symmetric either. The transform of the pillbox, however, is the radially symmetric jinc function[35], and thus the convolution $F(u,v) \otimes jinc(q)$ is radially symmetric. The disadvantage of circular zero-filling is that it results in a smaller dataset:[36] multiplying by a pillbox of radius r results in a matrix that is $\pi/4$ the size of one created by a square that has sides of $2r$.

The sharp edge of the pillbox means that the side lobes of its transform are not insignificant [92]. This effect was particularly apparent in the power spectrum at low spatial frequencies. As expected, the use of additional filtering to taper the pillbox smoothly to zero at its edges reduced the large sidelobes of the jinc function but increased the width of the main lobe. Figure 34 compares the power spectrum profiles of the sinc product, the jinc, and a jinc with a 'circular' Hanning window (see below). An approximation of the shape of each window's transform can be obtained by rotating its profile about the Y-axis. It is clear from this that convolution of the data transform with the transform of the square window will introduce artifact which can be avoided by convolving instead with the bell shape of the circular Hanning window, and that the Hanning window will tend to 'smooth' the profile. This damping of the frequency response in the windowed profiles did however make it easier to interpret them.

[35]The jinc function is defined [97] as $jinc(q) = J_1(\pi q)/2q$, where J_1 is the Bessel function of the first kind of order one.

[36]There was no loss of data in the analysis of the 1024x1024 matrix since the original dataset was circular.

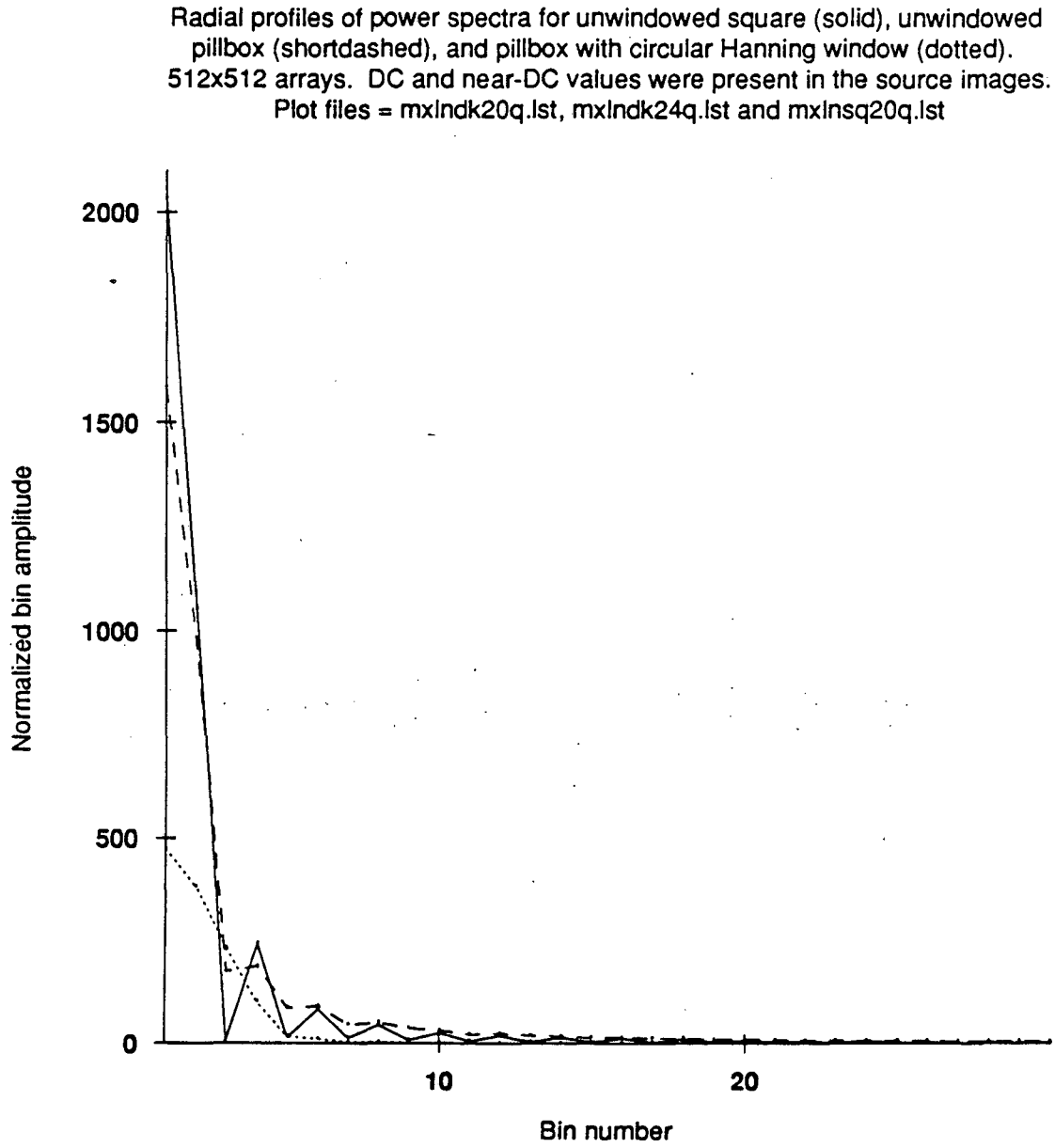

Figure 34: *Comparison of power spectrum profiles of an unwindowed square (solid), unwindowed pillbox (shortdashed), and a pillbox with its edge tapered by a circular Hanning window (dotted line). Note that DC and near-DC values are present in these profiles, and that only the first 30 bins are represented.*

The effects of various windowing schemes [92] on a pillbox are shown in Figure 35. The Hanning window was chosen for use in all the analyses because it tapered to zero at the beginning of the lower region of interest (bins 14 to 20) and did not shift the power peak. The radial symmetry of the image was maintained by using a 'circular' Hanning filter based on a quarter cosine rotated about image center. Apart from differences in amplitude, the windows had almost identical data transform profiles (Figure 36).

6.3 Analysis results and interpretation

6.3.1 Gland location power spectra

Spatial frequency power spectra were derived for the 16 samples of gland locations. The radial profiles of all spectra had the same general shape (see Figure 32):

- The initial bins (two bins for 1024x1024 profiles, and four for 512x512 profiles) were empty because the DC and near-DC components of the profile were zeroed for the display[37].

- Power then rose to a maximum between bins 14 to 20, which corresponded to a mean spacing of 1.48 to 2.11 mm.

- This maximum was followed by a reduction in profile power between bins 23 and 34 in most but not all of the profiles.

- The peak power for the profile occurred between bins 52 and 63, representing mean spacings of 0.45 to 0.55 mm.

[37] A spike that appeared in the fifth bin of several profiles was the tail of the DC convolution with the jinc.

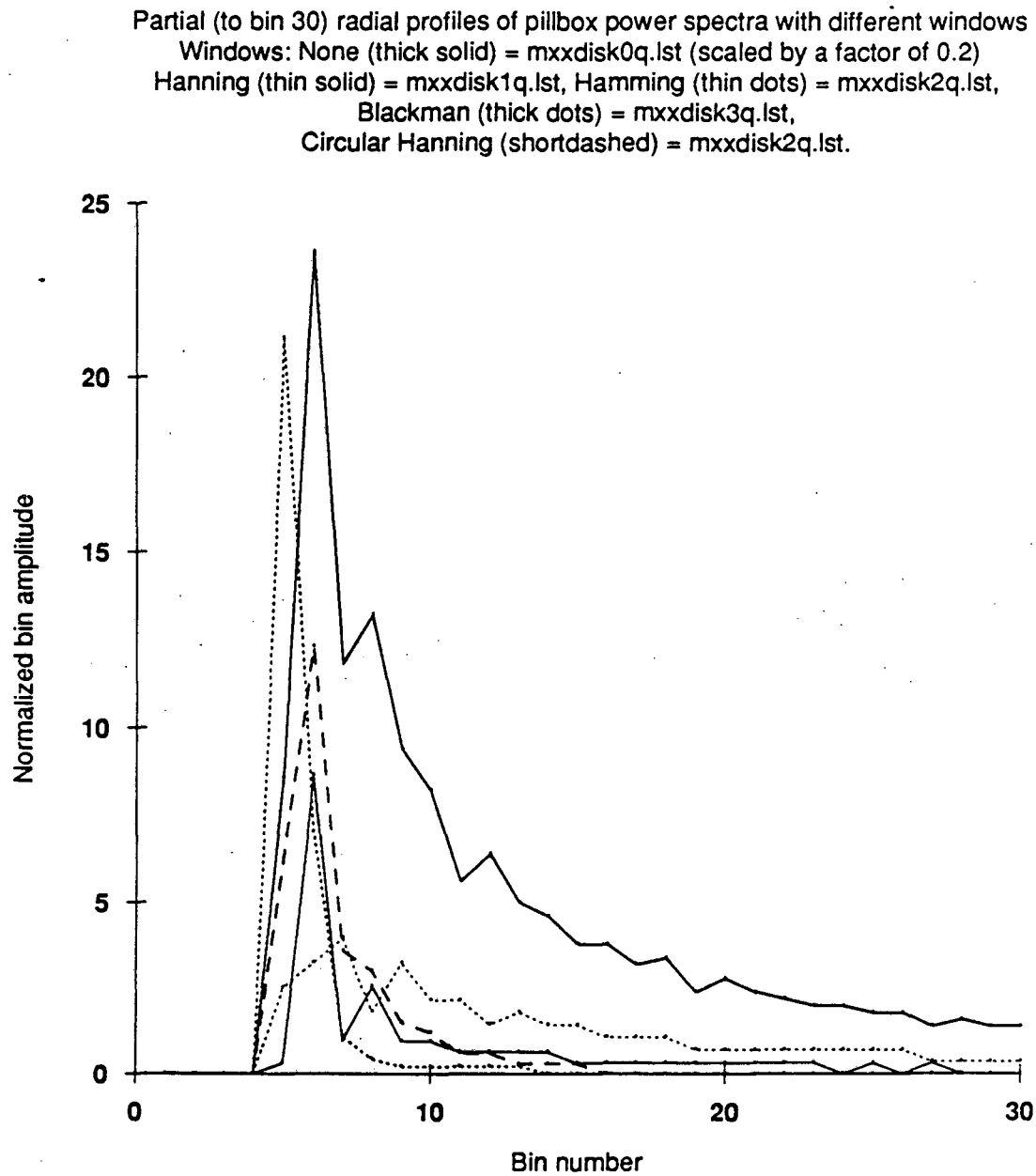

Figure 35: *Effect of various windows on the power spectrum profile of a pillbox.*

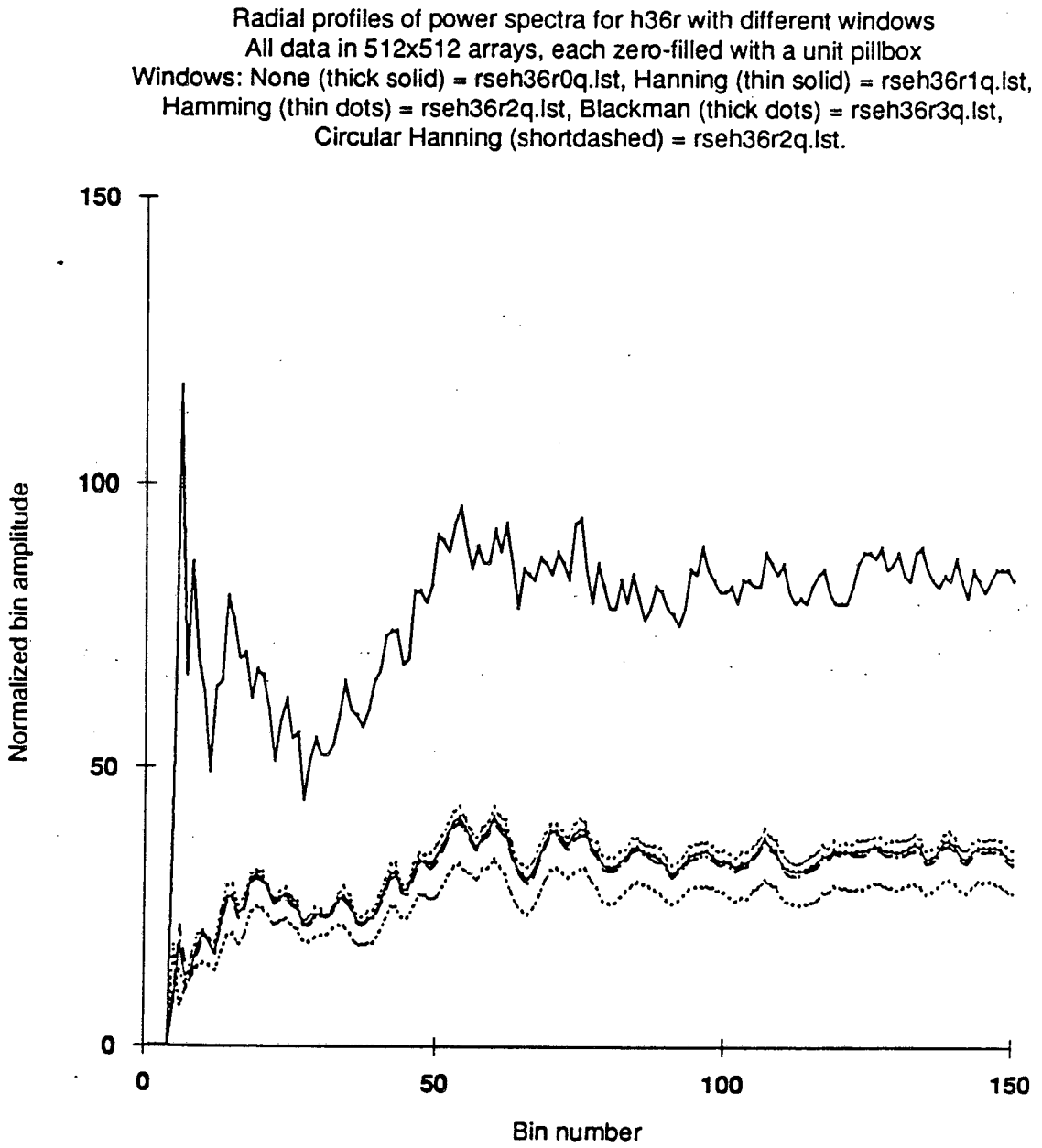

Figure 36: *Effect of various windows on the power spectrum profile of data.*

- There were a number of minor peaks present in each profile between the first and second frequency maxima.

Small shifts in peak values occurred if different binning criteria were used[38], but the overall profile shape was not affected.

The low frequency maximum which occurred between bins 14 and 20 was associated with a pattern of small roughly circular gland-free regions or 'holes' in the field of points. Gland location data in which these regions were visually present characteristically had power spectrum profiles with a low frequency maximum followed by a power minimum (Figure 37), whereas profiles of samples in which holes were not visible had several low frequency peaks and no power minimum. The power peak between bins 52 and 63 represented the modal spacing between the points themselves. As discussed in Section 6.3.2 below, a similar value for the spacing was obtained from the ACE, and this value was very close to the minimum interpoint spacing. Finally, the secondary peaks between the two maxima were harmonics of the first maximum's component frequencies. The association of each peak with a fundamental spatial frequency gave another estimate of the range of the low frequency maximum. A similar estimate could not be made for the second maximum since the harmonics of its components were buried in the high frequency fluctuations.

The interpattern spacings present in the 16 samples are shown in Tables 9 and 10, with the mean spacing and the unbiased estimate of the standard deviation[39]

[38]For example, the intensity values could be rounded down rather than being rounded to the nearest integer.

[39]The small number of samples results in a slight negative bias in the estimation of σ. This bias is corrected by multiplying the calculated moment by a factor of $\frac{n}{n-1}$, where n is the total number of samples [98].

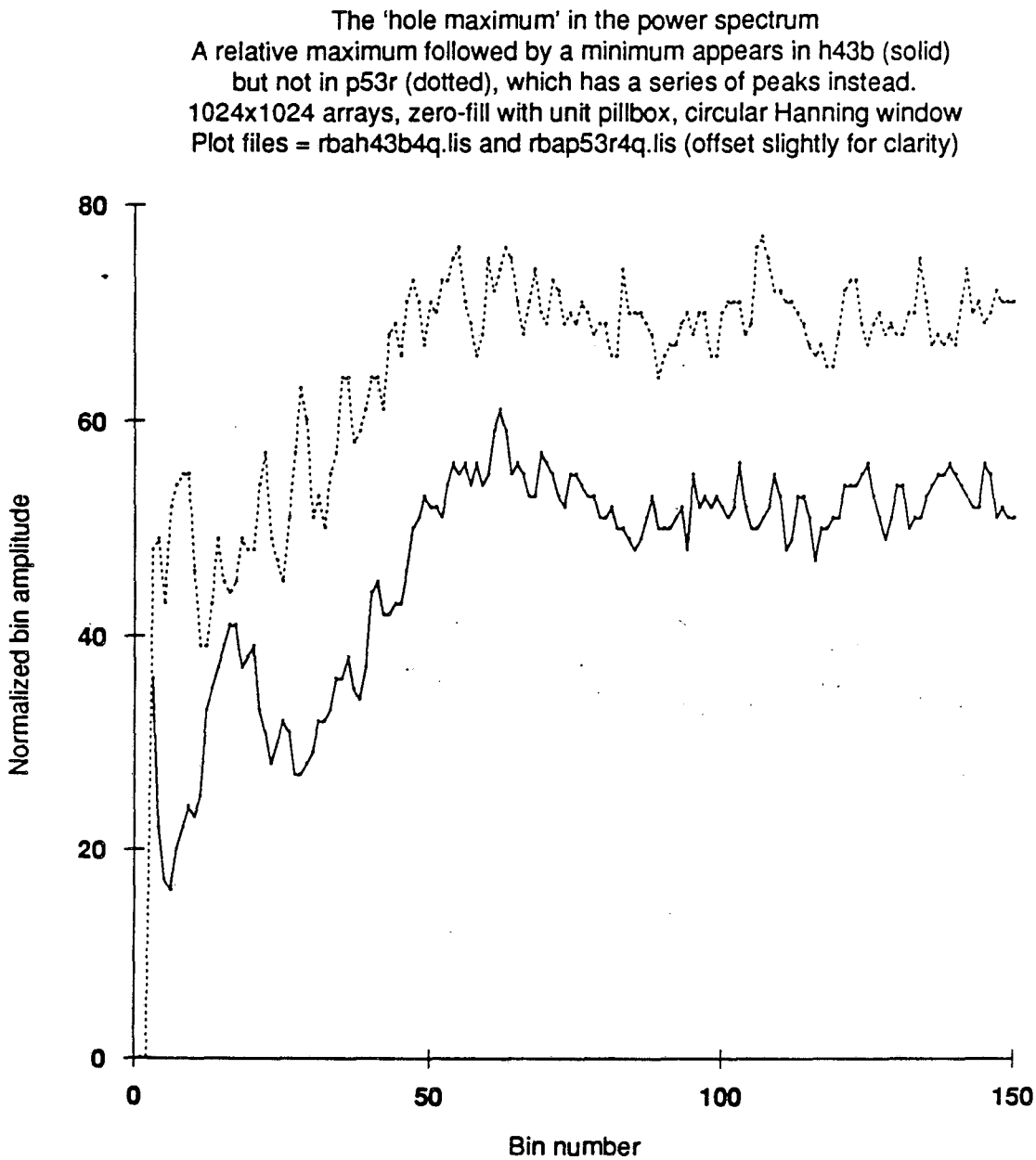

Figure 37: *The 'hole' maximum in the power spectrum profile.*

in the last two rows of each table. The superimposition fit, which is discussed in Section 6.6 below, represented the closest fit of a simulated distribution. The distances relating to the low-frequency maximum and the minimum following it are not tabulated for p53r and p54b, since these samples did not display a definite low-frequency maximum. In two cases (samples k44b and m46b), the low frequency maximum consisted of a single peak, and thus the peak 'range' for these samples is a single number. Interpretation of the profiles was aided by the analysis of simulations, which are discussed in Section 6.5.

6.3.2 Gland location autocorrelation estimates

Autocorrelation estimates were also computed for the 16 samples of gland locations. All such autocorrelation estimate profiles had a similar shape (see Figure 33):

- The first bin was empty due to the zeroing of the DC component.
- The next few bins were empty because of the requirement that pores be separated by a minimum of three pixels, a criterion which was used to distinguish a single large gland blot from two or more merged blots.
- Bin amplitude then rose rapidly to a profile maximum between bins 9 and 11. Since the first bin contained the value for correlation at zero displacement, the distance of separation for each bin was equal to the bin number less one. This gave a range for pore separations of 8 to 10 pixels, or 0.44-0.55 mm, which agreed with the result of 0.49 $\pm$0.040 mm obtained from the PS.

Sample	Range of low frequency peaks	Local maximum	Superimpo-sition fit	Range from harmonics
h36r	1.57 - 2.18	2.18	1.77	1.77 - 2.15
h41r	1.49 - 2.02	1.66	1.66	1.66 - 1.88
h43b	1.49 - 1.88	1.88	1.66 - 1.77	1.49 - 1.77
h44r	1.57 - 2.18	1.88	1.77	1.77 - 2.15
h53b	1.41 - 1.88	1.88	1.77	1.88 - 2.15
h54b	1.49 - 2.18	2.18	1.82	1.66 - 1.99
h55r	1.18 - 2.35	1.41	1.44	1.38 - 2.15
j43b	1.29 - 2.18	2.18	1.88 - 2.21	1.49 - 2.32
j44b	1.29 - 2.18	2.18	1.49 - 2.21	1.77 - 2.32
k42b	1.49 - 2.35	1.49	1.49	1.49 - 2.15
k42r	1.35 - 2.35	1.49	1.49	1.38 - 2.15
k44b	1.57	1.57	1.49	1.49 - 2.15
m42r	1.13 - 1.88	1.49	1.44	1.49 - 2.15
m46b	2.35	2.35	2.15	1.49 - 2.54
p53r	N/A	N/A	N/A	N/A
p54b	N/A	N/A	N/A	N/A
$\overline{X}$	1.48 - 2.11	1.84	1.67 - 1.75	1.59 - 2.14
σ_u	±0.31 ±0.25	±0.35	±0.22 ±0.30	±0.17 ±0.20

Table 9: *Interpattern distances associated with peaks of low spatial frequency.* $\overline{X}$ *is the arithmetic mean, and* σ_u *is the unbiased estimate of the standard deviation for all samples [98]. All measures are in mm.*

Sample	Range of profile minimum	Range of high frequency peaks	Local maximum	Superimposition fit	Peak in ACE
h36r	0.78 - 1.35	0.47 - 0.54	0.54	0.47	0.50
h41r	0.83 - 1.29	0.44 - 0.51	0.51	0.46	0.50
h43b	0.76 - 1.29	0.41 - 0.53	0.46	0.41	0.44
h44r	0.81 - 1.35	0.45 - 0.55	0.49	0.46	0.50
h53b	0.83 - 1.29	0.46 - 0.54	0.54	0.47	0.44
h54b	0.86 - 1.35	0.44 - 0.57	0.46	0.46	0.50
h55r	0.86 - 1.23	0.43 - 0.56	0.52	0.50	0.50
j43b	0.86 - 1.23	0.46 - 0.56	0.46	0.44	0.50
j44b	0.86 - 1.18	0.44 - 0.56	0.46	0.44	0.50
k42b	0.78 - 1.13	0.44 - 0.56	0.48	0.50	0.44
k42r	0.88 - 1.29	0.44 - 0.54	0.54	0.50	0.50
k44b	0.88 - 1.29	0.50 - 0.57	0.54	0.50	0.55
m42r	0.86 - 1.09	0.44 - 0.56	0.44	0.50	0.55
m46b	1.09 - 1.35	0.42 - 0.57	0.42	0.50	0.50
p53r	N/A	0.46 - 0.52	0.52	0.52	0.55
p54b	N/A	0.46 - 0.59	0.46	0.52	0.44
$\overline{X}$	0.85 - 1.26	0.45 - 0.55	0.49	0.48	0.49
σ_u	$\pm.085$ $\pm.090$	$\pm.023$ $\pm.022$	$\pm.043$	$\pm.034$	$\pm.040$

Table 10: *Interpattern distances associated with profile minima and peaks with high spatial frequency.* $\overline{X}$ *is the arithmetic mean, and* σ_u *is the unbiased estimate of the standard deviation for all samples [98]. All measures are in mm.*

- The amplitude of the profile dropped rapidly after this maximum, and then declined slowly for the remainder of the profile[40].

Autocorrelation estimate peak data for all samples appears in Table 10.

6.4 Interpretation of results

The power spectra and autocorrelation estimates of the data suggest that the spatial organization of eccrine gland openings (pores) on the skin surface is as follows:

1. The pores have a modal[41] intergland spacing of approximately 0.44-0.55 mm.

2. There is a secondary pattern in most of the distributions that consists of small gland-free areas.

The first finding is probably a consequence of normal skin growth. With some exceptions (such as the formation of scars or stretch marks), increases in skin surface area are believed to take place by the diffuse addition of new tissue throughout the area rather than by the formation of patches of new skin [100]. The number of eccrine glands does not change after birth, and as the individual grows, gland density decreases as the result of dilution; the skin of a year-old infant has eight to ten times the gland density of an adult [57]. The existence of a modal intergland spacing is thus not surprising.

[40] A 'hole' peak, which would appear between bins 13 and 16 in the ACE, could not be distinguished from the surrounding fluctuations.

[41] The mode is the spatial frequency that occurs most often in the distribution [99], i.e. the peak with the highest power in the PS.

The origin of the gland-free areas is less clear. The 'hole' pattern could be artifact: The 'hole' peak was not strongly present in several power spectrum profiles; a similar secondary pattern can appear in simulations which have interpoint distances and point totals similar to the real data matrices; and the total number of data samples was small. There is, however, a possibility that the pattern has an anatomic basis. In cases where the hairs in a photograph of the test area could be counted, the total number of hairs was close to the total number of holes in the gland location data. The spatial distribution of the hairs was also similar to that of the small gland-free regions. Unfortunately, the hole pattern was detected some time after the experiments were performed, and the follicle location data obtained when the measurements were made was not sufficient to test for a correspondence between gland free areas and hair follicles.

One explanation for the absence of such holes in some of the data is that a lack of glands in the immediate vicinity of a hair follicle may only be apparent if most of the glands in the surrounding area are active, so that a 'hole' is outlined by the pores surrounding it. Since up to 40% of the sweat glands of sedentary individuals living in a temperate climate may be quiescent [73], a pattern formed in this manner is likely to be present in physically active subjects, who have a larger proportion of active to inactive glands [57]. In fact, the 'hole' pattern was apparent in the gland location power spectra of those subjects who exercised and was absent in the profiles of those who did not.

6.5 Simulations and modelling

A stochastic model for the gland locations was constructed. Gland locations were uniformly distributed in a circular field, with a radius of exclusion around each point representing the minimum intergland distance. The model parameters were (1) the probability that the interpoint distance would be between certain minimum and maximum separations, (2) the maximum number of points in the field, and (3) the number of attempts that would be made to insert a new point into the field. The model could also create circular point-free regions (i.e. artificial holes) in this field of points, with control over the same parameters (the maximum number of holes, etc.) that were used to locate the points. The simulations were also useful in the interpretation of certain profile features, and could be used to test for complete spatial randomness in the data.

6.5.1 Cumulative inversion

The technique of cumulative inversion [101] was used to generate uniform distributions for the points (gland locations) and the interpoint distances in the circular area. Cumulative inversion can be applied if $f(s)$, the probability distribution function (PDF) of a random variable s is known, where $f(s)\Delta s$ is the probability that the variable will assume a value in the interval $(s, s + \Delta s)$. The cumulative density function (CDF) for s is the probability that the variable will assume a value less than or equal to some limiting value of s. If the CDF for $f(s)$ is $F(s)$, then

$$F(s) = \int_{-\infty}^{s} f(s')ds'.$$

$F(s)$ is a random variable uniformly distributed between zero and one, and if the function F can be inverted, then values of s with a PDF of $f(s)$ can be determined. If for instance a pseudo-random number generator is used to generate η uniformly between zero and one, then

$$s = F^{-1}(\eta)$$

will generate s randomly according to the PDF $f(s)$. The application of the technique is best demonstrated by its use below.

6.5.2 Derivation of the interpoint distance distribution

A trapezoidal probability density function (Figure 38) was used as a simple model of the distribution of interpoint distances, where a is the minimum interpoint distance, b and c are breakpoints and d is the maximum distance between points. Between the breakpoints the probability of acceptance is one, while between a and b as well as c and d the probability is less than unity and the acceptance of values that fall in these ranges is conditional. This particular model was chosen because preliminary analysis of the data suggested that most of the points were about the same distance apart, and this model was a simple way to both establish that requirement and have some means of manipulating it. The interpoint distance was in effect a radius of exclusion in the neighborhood of the point, and the limitation of a maximum interpoint distance prevented the creation of unacceptably large domains of exclusion.

The uniform distribution of interpoint distances was determined as follows:

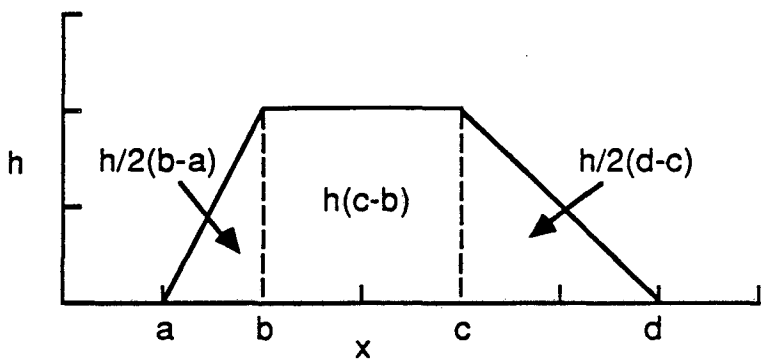

Figure 38: *Trapezoidal probability density function used to determine interpoint distances.*

With the area of the trapezoid set equal to the total probability density, i.e.

$$1 = \frac{h}{2}(b-a) + h(c-b) + \frac{h}{2}(d-c)$$

the PDF for the trapezoid is

$$p(x) = \begin{cases} 0 & \text{for } x \leq a \\ h(\frac{x-a}{b-a}) & \text{for } a \leq x \leq b \\ h & \text{for } b \leq x \leq c \\ h(\frac{d-x}{d-c}) & \text{for } c \leq x \leq d \\ 0 & \text{for } x \geq d \end{cases}$$

The corresponding cumulative density function, obtained by integrating $p(x)$, is

$$P(x) = \begin{cases} 0 & \text{for } x \leq a \\ \frac{h}{2}\frac{(x-a)^2}{b-a} & \text{for } a \leq x \leq b \\ \frac{h}{2}(b-a) + h(x-b) & \text{for } b \leq x \leq c \\ \frac{h}{2}(b-a) + h(c-b) + \frac{h}{2}(d-c) - \frac{h}{2}\frac{(d-x)^2}{d-c} & \text{for } c \leq x \leq d \\ 1 & \text{for } d \leq x \end{cases}$$

Inverting this function and letting

$$\begin{aligned} bp1 &= \frac{h}{2}(b-a) \\ bp2 &= 1 - \frac{h}{2}(d-c) \end{aligned}$$

we have

$$x = f(y) = \begin{cases} a + \left(\frac{2y(b-a)}{h}\right)^{\frac{1}{2}} & \text{for } y \leq bp1 \\ b + \frac{(c-b)(y-bp1)}{bp2-bp1} & \text{for } bp1 \leq y \leq bp2 \\ d - \left(\frac{2(1-y)(d-c)}{h}\right)^{\frac{1}{2}} & \text{for } bp2 \leq y \end{cases} \tag{4}$$

If y $(= p(x))$ is randomly distributed between zero and one, then x (the interpoint distance) is randomly distributed according to the PDF for the trapezoid $p(x)$.

6.5.3 Derivation of the distribution of points in a circular field

Once its minimum interpoint distance has been set, the point must be placed somewhere within the field of points. The function used to fill the circular area

uniformly,

$$r = (2\pi R^2 y)^{\frac{1}{2}},$$

where R is the domain radius and r is the distance from the point to the center, was also determined using cumulative inversion. In this case, the two-dimensional PDF is a cylinder of height h, so that

$$1 = \int_0^\infty \int_0^{2\pi} p(r\cos\theta, r\sin\theta) r dv d\theta = \pi h R^2$$

and $h = 1/\pi r^2$. The PDF for this function is then

$$p(x,\theta) = \begin{cases} \frac{r}{\pi R^2} & \text{for } 0 \leq r \leq R \\ 0 & \text{for } r > R \end{cases}$$

and the corresponding CDF is

$$P(x,\theta) = \begin{cases} \frac{r^2}{2\pi R^2} & \text{for } 0 \leq r \leq R \\ 1 & \text{for } r > R \end{cases}$$

Solving for r,

$$r = (2\pi R^2 y)^{\frac{1}{2}} \tag{5}$$

for y between zero and one.

Once an interpoint distance was determined by Equation 4, Equation 5 was used to generate a radial value r_t. An angle θ_t (equal to $2\pi\eta$, where η was a pseudo-random number between zero and one) was computed and the program attempted to insert the new point into the existing field of points at (r_t, θ_t). A total of N insertion attempts were made for a given r_t (with a fresh θ for each attempt) before

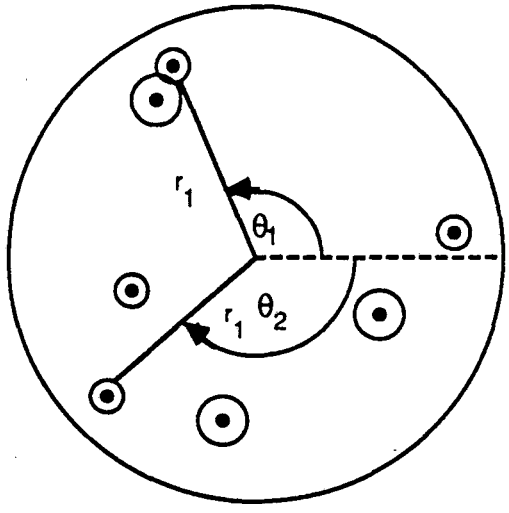

Figure 39: *Insertion of a new point. The location at (θ_1, r_1) is not accepted since the new radius of exclusion intersects with an old one. A successful insertion occurs at (θ_2, r_1).*

that radius was abandoned and a new one generated (Figure 39). If a total of M such attempts (each with a new radius) failed, the simulation was considered finished before the maximum number of points had been inserted.

6.6 Results of simulations

The simulations verified and extended the interpretations of the data profiles. Point distributions with a narrow range of interpoint distances ('monochromatic' distributions) were generated by a trapezoidal PDF in which $a = b = c$ and $d = c + 0.1$. The PS profiles of ten such distributions were averaged together to make a mean profile. This mean profile provided an estimate of peak shape and location at the particular spatial frequency. Visual fits of such mean profiles to major peaks in data profiles (Figure 40) were in good agreement with the values taken directly

from the profiles (Tables 9 and 10).

Mean autocorrelation estimate profiles were constructed in a similar fashion. In simulations with a minimum interpoint distance of 0.165 mm (three pixels), the ACE profile rose from zero to the maximum within two bins while the data profiles, which had the same minimum interpoint distance by virtue of the pore separation criterion, reached their maximum more slowly, after 6 to 8 bins. This demonstrated that the initial rapid rise in the data profiles was not an artifact of the pore separation criterion, but instead represented the clustering of interpoint separations near the modal interpoint separation. The fact that the profile amplitude is near zero at three pixels separation also suggests that (neglecting multiple pores of the same gland) there may be a minimum intergland distance which is slightly less than the minimum acceptable distance embedded in the pore location software.

Modelling was also used to study aspects of the profiles that were a consequence of the process of profiling. The mean profiles provided an idea of the shape of the real data peak at a particular frequency, and made it easier to distinguish peak broadening due to quantization error from broadening due to the merger of adjacent peaks. Sampling error was confirmed as a source of low frequency fluctuations in a similar fashion[42]. Simulated profiles were also used to verify the interpretation of the secondary peaks as harmonics. The model software was also the source of test patterns (such as an impulse, unit square, etc.) for the analysis software.

Finally, simulation profiles that resembled data profiles (Figure 41, Figure 42) could be obtained by using the same approximate number of points, setting the lower limit for interpoint distance near to the modal interpoint distance in the data

[42]Since the number of circumferential pixels averaged for each integral radius is proportional to the radius, large fluctuations in the profile could (and did) occur for radii near the origin.

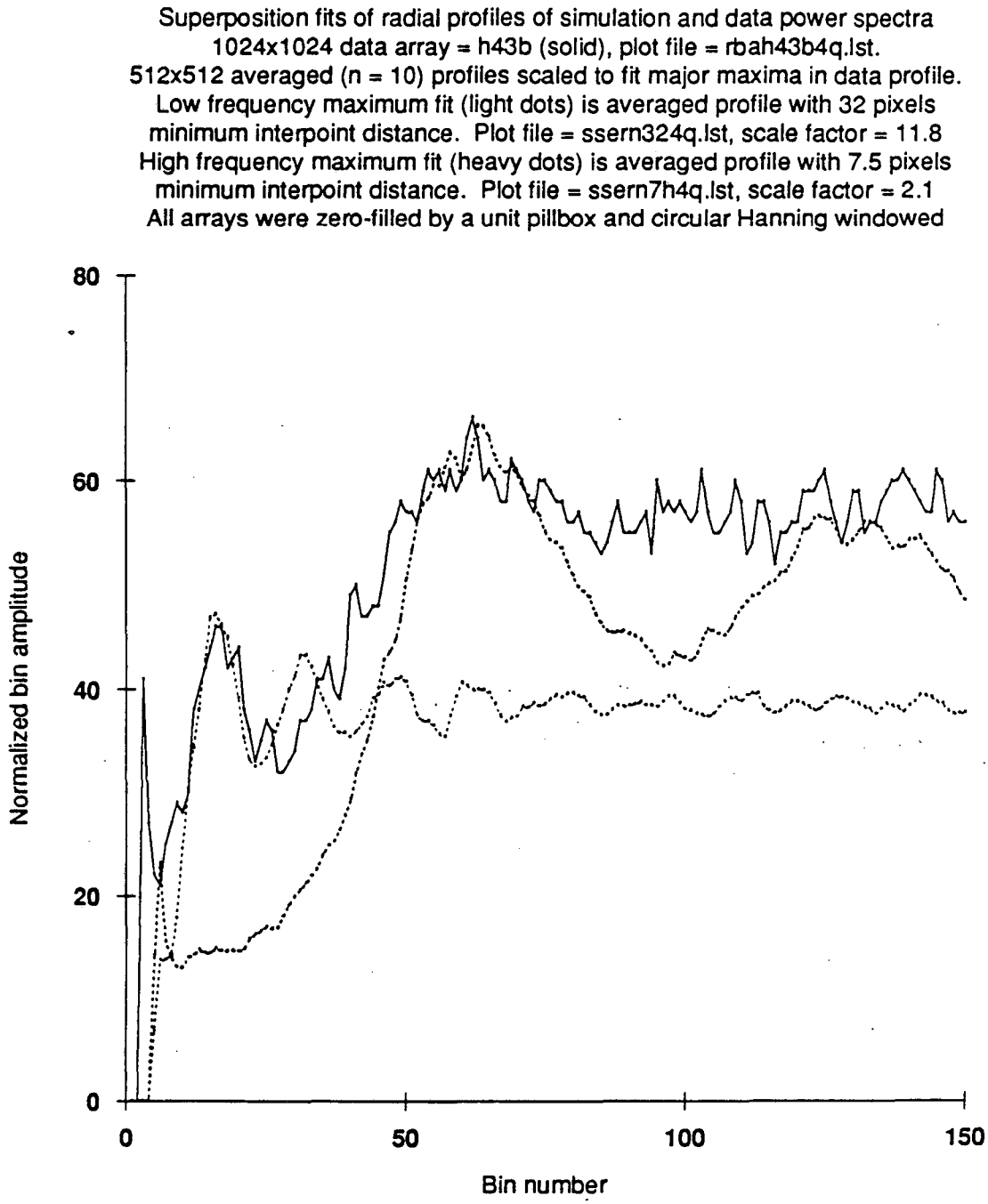

Figure 40: *Visual fit of mean profiles to a data profile.*

and adjusting the inter-hole spacing appropriately.

6.7 Comparison of Fourier analysis with conventional methods for detection of pattern.

The analysis of a spatial point distribution for the presence of pattern begins by testing the distribution for complete spatial randomness (CSR) [102]. This is usually accomplished by comparing the empirical distribution function (EDF) of the location data with simulation envelopes derived from the EDFs of multiple independent simulations (see Figure 43, from Diggle). Each such simulation is based on a particular measure of interpoint distance or event density, for example point-to-nearest-event distance. If some portion of the data EDF falls outside the envelopes defined by the simulation EDFs, then the distribution is taken to be non-random. In contrast, it is immediately apparent from the examination of the power spectrum and autocorrelation estimate profiles whether or not a given distribution is random. If any question exists, a profile of a random distribution can be created by averaging the profiles of N random simulations (in this case, simulations with no constraint on interpoint distances and no holes created in the field of points) and comparing this with a data profile.

If pattern is present in the data-set, the next task is the formulation and fitting of a stochastic model for the distribution. The conventional approach compares the data to envelopes generated by simulations of a fitted model. As has been demonstrated, Fourier analysis proceeds in much the same way, but with the important difference that the existence of pattern and its quantification are an immediate

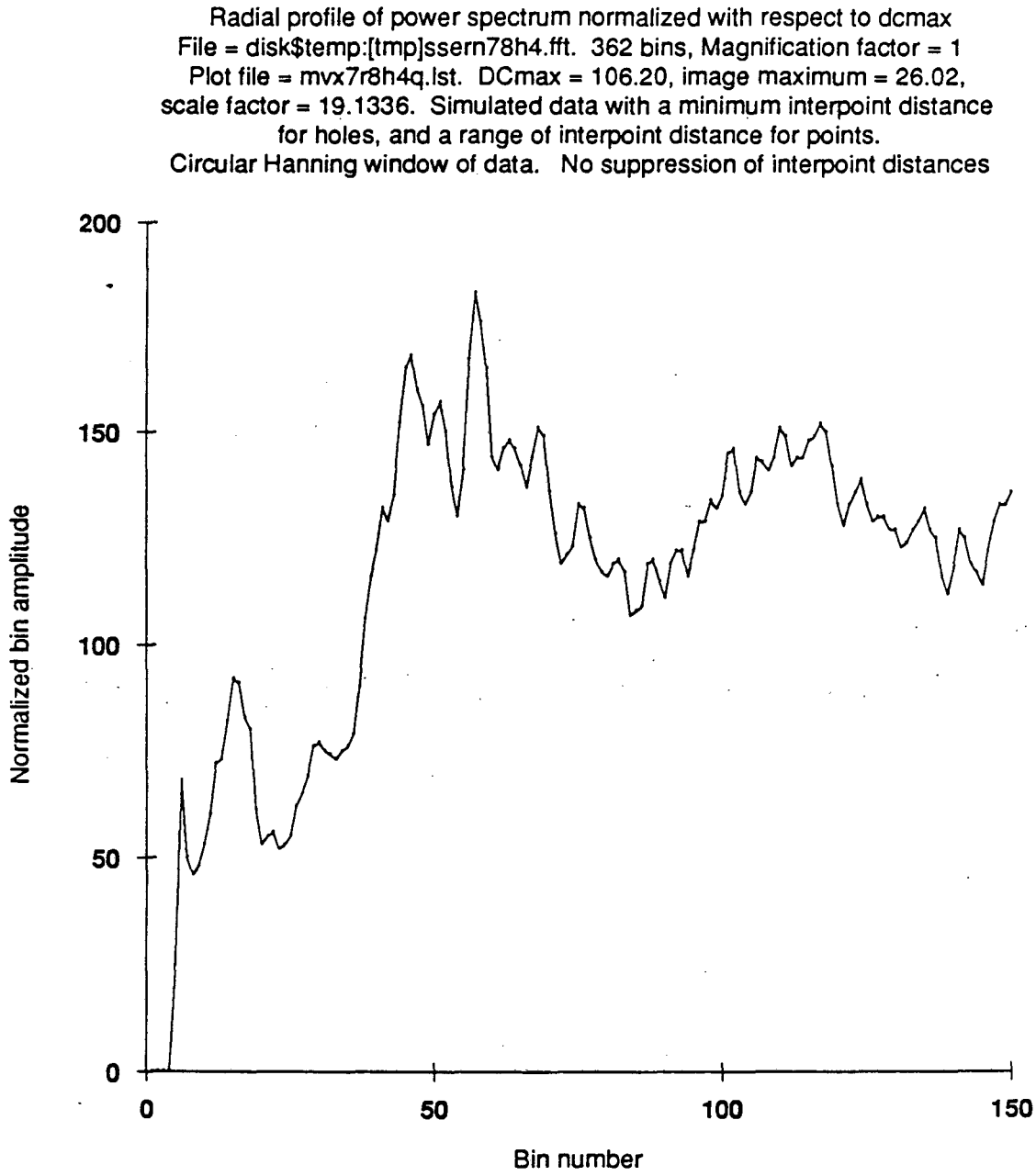

Figure 41: *Power spectrum profile of data simulation.*

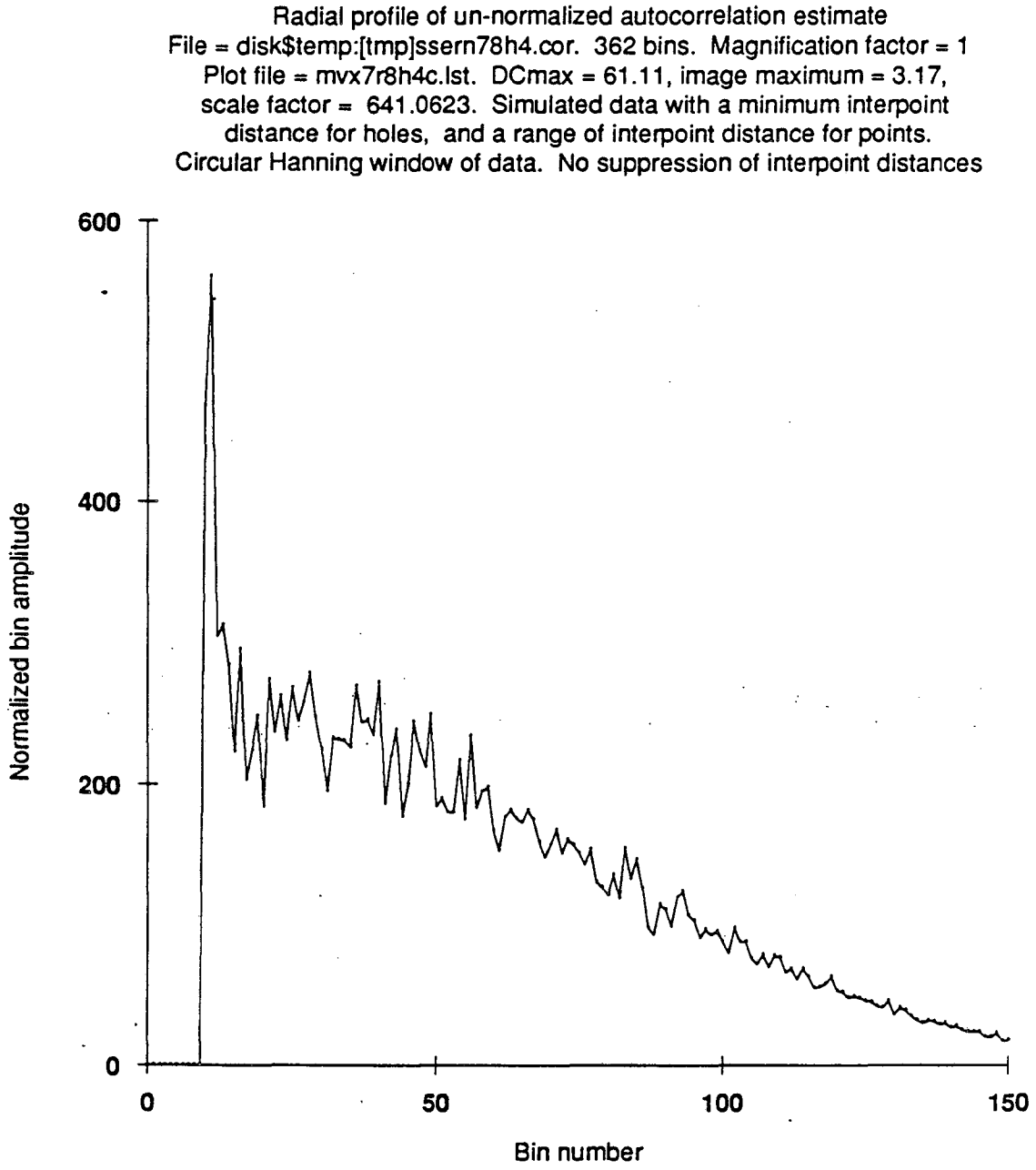

Figure 42: *Autocorrelation estimate profile of data simulation.*

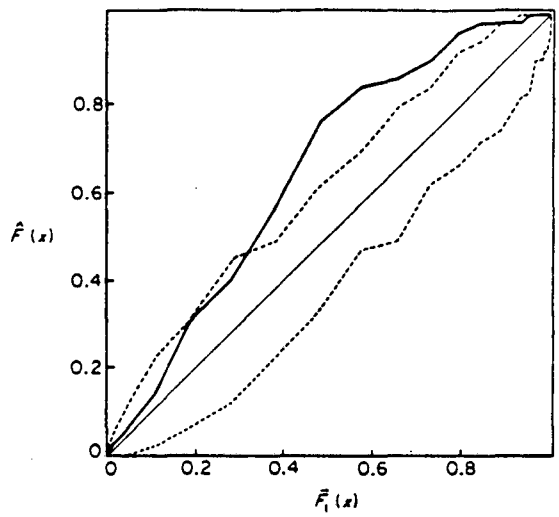

Figure 43: *EDF plot of nearest neighbor distances for biological cells, where the dark line is data and dashed lines are upper and lower envelopes from 99 simulations of CSR (from Diggle [102]).*

result of the initial analysis.

Digital signal analysis has previously been used to quantify some aspects of skin structure [103], but this is apparently the first time Fourier analysis has been employed in the analysis of biologically related spatial point patterns. The advantage of the technique is that spatial information is immediately quantifiable, and that large data-sets are not a barrier. Its disadvantage is a large computational hardware requirement: However, as computing machinery continues to decrease in cost, this will become less of an obstacle.

7 Conclusions

7.1 Summary of results

The transdermal potential in the same area on the backs of the hands of six subjects was measured with electrodes, an electrolyte, and skin/electrode interfaces that were designed to minimize artifact. Careful attention to signal amplification, recording and the electrical environment ensured that an accurate record was made of the potential differences present. The experimental conditions (including the selection and habituation of subjects, the preparation of the area according to standard protocols, and the measurement procedures and environment) were chosen in order to minimize eccrine gland activity and provide measurements reflecting only non-sudorific contributions to the potential.

Gland pores in the area were located by stimulating the glands with pilocarpine and making prints or blots of their secretions with a specially prepared paper. The pore centers were then located in digitized images of the gland prints, and the correlation between the measured potential and the number of glands at the site of each measurement was tested. The pore location arrays also formed the basis of a spectral analysis of the spatial frequencies present in the point pattern. Simulations of gland distributions by a stochastic model were used to verify the uniqueness of the findings.

7.2 Inactive glands as a source of potential

Two results of these investigations stand out, the first being that non-secreting eccrine glands appear to play no role in the generation of the transdermal potential,

and the second (which is discussed below) that the pores on the skin exhibit a definite pattern. No correlation was found between the magnitude of the potential and the estimated number of eccrine glands at each measurement site for nearly all subjects. The apparent correlation present in a few samples was probably due to experimental error or chance. This result agreed with the prediction of our equivalent circuit model that the passive glands provided a minimal contribution to the potential and that there was at least one other source of potential variability. The analysis here shows that one possible source is variability in the permeability barrier of the skin. If the barrier behaves like a permselective membrane, then it is capable of maintaining a potential across itself. Regional variations in membrane permselectivity can account for the observed variations in this potential. If this is in fact the case, then the potential difference may be useful as an assessment of the competence of the barrier.

7.3 Potential contributions from hairs

It has been pointed out that the state of the eccrine glands must be characterized when making potential measurements, and this caveat should probably be extended to include the pilosebaceous apparatus as well. Under certain conditions (presumably if the hydrophobic sebaceous secretions are removed) hair follicles are believed to act as diffusion shunts for ionic substances [35,80]. Since the alcohol used in these studies to dehydrate the skin appeared to remove this secreted material, it was somewhat surprising to find that the potential over hair follicles was not substantially different from surrounding values. In contrast, Barker and his coworkers discovered a rough correlation of low transcutaneous voltage with hairiness,

which they suggest is due to current leakage along the follicles [2]. If indeed follicle density is the active factor (rather than epithelial thickness, for example) then one possibility is that follicle paths can exist when the skin is well hydrated, but that the time of hydration was not sufficient for the establishment of such a connection in the experiments of this thesis.

7.4 Evaluation of methods

The techniques used to determine the grid of potentials and to locate the pores on the skin provided adequate samples of both distributions, but the method used to establish the correspondence between the gland location array and the array of potentials could be improved. One method of doing so would have been to use the electrode tip to locate the position of the pen guides in the fiducial template directly (after locking it in place on the skin), rather than using the template to make the ink marks and then determining their positions. However, this refinement of the method would not affect the results. The effective area of the electrode is not well defined and may in fact vary from one site to the next, so that the number of glands in each electrode area will always be an approximation.

7.5 Spatial distribution patterns of eccrine glands

The gland location matrix was also used to quantify the spatial distribution of the pores on the skin, which has not been done previously. A spectral analysis of the spatial frequencies present in the eccrine gland location data was made with Fourier techniques. Slices from the center to the edge of the two-dimensional images

were used to construct 'mean radial profiles', which reduced the three-dimensional (X, Y and intensity) images to a two-dimensional plot. The image must be radially symmetric in order to create a radial profile, but this display technique is very useful in the evaluation of the sort of diffuse transform that is obtained from a distributed pattern.

Radial profiles of the power spectra and autocorrelation estimates found evidence of pattern in the gland distribution, in that the pores tend to be about the same distance apart (0.49 $\pm$0.043 mm) and may also be absent in the immediate neighborhood of hair follicles. This is evidently the first time that Fourier techniques have been used to make a spectral analysis of biologically related spatial point patterns. Fourier analysis can provide information about the two-dimensional spatial organization of points accurately and more rapidly than can conventional statistical methods, but has the disadvantage of a large computational requirement. However, as the cost of computing machinery continues to decline, this technique will very likely find as wide an application in biology and social science as it has in physics and engineering.

7.6 Directions for future investigations

The existence of selectivity in the skin permeability barrier could be investigated by experimental measurements of diffusion potentials across model systems [50] such as keratinizing cell cultures or excised animal skin. However, the best approach to the question of what generates and influences the transdermal potential would be to investigate the paths taken by ionic compounds through the skin, the ionic species that constitute the flow, and the permeabilities or resistivities of skin

structures (particularily the barrier layer) to various ionic species. The vibrating probe electrode [104] has been used to vectorize ionic flow and might be applied in the identification of current sources and sinks in mammalian skin [2]. An alternate approach would be to visualize the paths of current flow with tracers and dyes [43,105]. Such studies would likely result in new or improved diagnostic and therapeutic methods for dermatologic disease, as well as adding to our fundamental understanding of skin physiology.

8 Bibliography

1. Woodrough, R.E. *An investigation into the measurement, interpretation, and clinical application of slowly-varying electrical potential difference on the surface of the human body.* Ph.D. Thesis, University of London, 1976.

2. Barker, A.T., Jaffe, L.F. and Vanable, J.W. The glabrous epidermis of cavies contains a powerful battery. *American Journal of Physiology*, **242**:R358-R366, 1982.

3. Foulds, I.S. and Barker, A.T. Human skin battery potentials and their possible role in wound healing. *British Journal of Dermatology*, **109**:515-522, 1983.

4. Fowles, D.C. Mechanisms of electrodermal activity. Chapter 9 in *Methods in Physiological Psychology. Vol. I: Bioelectric Recording Techniques. Part C: Receptor and Effector Processes*, edited by R.F. Thompson and M.M. Patterson, pp. 231-271. Academic Press, N.Y., 1974.

5. Woodrough, R.E. Measurement, interpretation and clinical application of slowly varying electrical potential difference. Chapter 5 in *Medical Electronics Monographs*, Numbers 23-27, edited by D.W. Hill and B.W. Watson, pp. 129-157. Peter Peregrinus Ltd, Herts, England, 1977.

6. Cole, K.S. and Curtis, H.J. Electric impedance of nerve and muscle. *Cold Spring Harbor Symposiums in Quantitative Biology*, **4**:73-89, 1936.

7. Salter, D.C. Quantifying skin disease and healing in vivo using electrical impedance measurements. In: *Non-Invasive Physiological Measurements*, edited

by P. Rolfe, Academic Press, London, 1979.

8. Salter, D.C. Alternating current electrical properties of human skin measured *in vivo*. Chapter 29 in *Bioengineering and the Skin*, edited by R. Marks and P.A. Payne, pp. 267-274. MTP Press, Lancaster, 1981.

9. Jacques, S. *Measurement of the water content of the stratum corneum of human skin using microwave probe.* Master's Thesis, Electrical Engineering and Computer Science, University of California, Berkeley, 1979.

10. Williamson, P.S., Fowles, D.C. and Weinberger, M. Electrodermal potential and conductance measurements clinically discriminate between cystic fibrosis and control patients. *Pediatric Research*, **19**:810-814, 1985.

11. Sloan, J.B. and Soltani, K. Iontophoresis in dermatology. *Journal of the American Academy of Dermatology*, **15**:671-684, 1986.

12. Cobbold, R.S.C. *Transducers for Biomedical Measurements: Principles and Applications*, John Wiley, New York, 1974.

13. Tregear, R.T. *Physical functions of skin.* Academic Press, London, 1966.

14. Edelberg, R. Electrical activity of the skin: its measurement and uses in psychophysiology. Chapter 9 of *Handbook of Psychophysiology*, edited by N.S. Greenfield and R.A. Sternbach. Holt, Rinehart and Winston, Inc., New York, 1972.

15. Venables, P.H. and Christie, M.J. Electrodermal Activity. Chapter 1 in *Techniques in Psychophysiology*, pp. 4-67. John Wiley and Sons, London, 1980.

16. Athenstaedt, H., Claussen, H. and Schaper, D. Epidermis of human skin: pyroelectric and piezoelectric sensor layer. *Science*, **216**:1018-1020, 1982.

17. Ödman, S. Potential and impedance variations following skin deformation. *Medical and Biological Engineering and Computing*, **19**:271-278, 1981.

18. Ödman, S. and Öberg, P.Å. Movement-induced potentials in surface electrodes. *Medical and Biological Engineering and Computing*, **20**:159-166, 1982.

19. Ödman, S. On the spread of deformation potentials in the skin. *Medical and Biological Engineering and Computing*, **20**:451-456, 1982.

20. Quinton, P.M. and Bijman, J. Higher bioelectric potentials due to decreased chloride absorption in the sweat glands of patients with cystic fibrosis. *The New England Journal of Medicine*, **308**(20):1185-1189, 1983.

21. Bijman, J. and Quinton, P.M. Apparent absence of cystic fibrosis sweat factor on ion-selective and transport properties of the perfused human sweat duct. *Pediatric Research*, **18**(12):1292-1296, 1984.

22. Sato, K. Differing luminal potential difference of cystic fibrosis and control sweat secretory coils in vitro. *American Journal of Physiology*, **247**;:R646-R649, 1984.

23. Boucher, R.C.Jr., Bromberg, P.A. and Gatzy, J.T. Airway transepithelial electric potential in vivo: species and regional differences. *The Journal of Applied Physiology*, **48**:169-176, 1980.

24. Knowles, M.R., Carson, J.L., Collier, A.M., Gatzy, J.T. and Boucher, R.C. Measurements of nasal transepithelial electric potential differences in normal human subjects *in vivo*. *The American Review of Respiratory Disease*, **124**:484-490, 1981.

25. Turner, K.S., Powell, D.W., Carney, C.N., Orlando, R.C., and Bozymski, E.M. Transmural electrical potential difference in the mammalian esophagus in vivo. *Gastroenterology*, **75**:286-291, 1978.

26. Edelberg, R. Relation of electrical properties of skin to structure and physiological state. *The Journal of Investigative Dermatology*, **69**(3):324-327, 1977.

27. Christie, M.J. Electrodermal activity in the 1980's: a review. *Journal of the Royal Society of Medicine*, **74**:616-622, 1981.

28. Feinberg, B.N. and Fleming, D.G., Editors *CRC Handbook of Engineering in Medicine and Biology. Section B: Instruments and Measurements. Volume 1.* CRC Press, West Palm Beach, Florida, 1978.

29. Spiegler, K.S. and Wyllie, M.R.J. Electrical potential differences. Chapter 7 in *Physical Techniques in Biological Research*, Second Edition, Volume II Part A (Physical Chemical Techniques), edited by D.H. Moore. Academic Press, New York, 1968.

30. Millington, P.F. and Wilkinson, R. *Skin*, Cambridge University Press, Cambridge, 1983.

31. Moschella, S.L. and Huxley, H.J., Editors. *Dermatology*, Volume 1, Second Edition. W.B. Saunders, New York, 1985.

32. Jarrett, A., Editor *The Physiology and Pathophysiology of the Skin.* Volume 1, The Epidermis. Academic Press, London, 1973.

33. Briggaman, R.A. Epidermal-dermal interactions in adult skin. *The Journal of Investigative Dermatology*, **79**:21s-24s, 1982.

34. Jakubovic, H.R. and Ackerman, A.B. Structure and function of skin. Chapter 1 in *Dermatology*, Volume 1, 2nd Edition, edited by S.L. Moschella and H.J. Huxley. W.B. Saunders, New York, 1985.

35. Scheuplein, R.J. Permeability of the skin: a review of major concepts. *Current Problems in Dermatology*, **7**:172-186, 1978.

36. Dugard, P.H. Skin permeability theory in relation to measurements of percutaneous absorption in toxicology. Chapter 22 in *Advances in Modern Toxicology*, Volume 4: Dermatotoxicology and Pharmacology, Edited by F.N. Marzulli and H.I. Maibach. John Wiley, New York, 1977.

37. Scheuplein, R.J. Properties of the skin as a membrane. Chapter X in *Advances in Skin Biology*, Volume 12 of *Pharmacology and the Skin*, edited by R. Montagna, E.J. Van Scott, and R.B. Stoughton. Appleton-Century-Crofts, New York, 1972.

38. Hurley, H.J. Permeability of the skin. Section IV in *Dermatology*, Volume 1, 2nd Edition, edited by S.L. Moschella and H.J. Hurley. W.B. Saunders, New York, 1985.

39. Elias, P.M., Cooper, E.R., Korc, A., and Brown, B.E. Percutaneous transport in relation to stratum corneum structure and lipid composition. *The Journal*

of Investigative Dermatology, **76**:297-301, 1981.

40. Elias, P.M. Epidermal lipids, barrier function and desquamation. *The Journal of Investigative Dermatology*, **80**:44s-49s, 1983.

41. Bowser, P.A. and White, R.J. Isolation, barrier properties and lipid analysis of stratum compactum, a discrete region of the stratum corneum. *British Journal of Dermatology*, **112**:1-14, 1985.

42. Squier, C.A. Effect of enzyme digestion on the permeability barrier in keratinizing and non-keratinizing epithelia. *British Journal of Dermatology*, **111**:253-265, 1984.

43. Squier, C.A. and Hall, B.K. The permeability of skin and oral mucosa to water and horseradish peroxidase as related to the thickness of the permeability barrier. *The Journal of Investigative Dermatology*, **84**:176-179, 1985.

44. Landmann, L. Epidermal permeability barrier: transformation of lamellar granule-disks into intercellular sheets by a membrane-fusion process, a freeze-fracture study. *The Journal of Investigative Dermatology*, **87**:202-209, 1986.

45. Menton, D.N. and Eisen, A.Z. Structure and organization of mammalian stratum corneum. *Journal of Ultrastructure Research*, **35**:247-64, 1971.

46. Jarrett, A., Editor *The Physiology and Pathophysiology of the Skin.* Volume 5, The Sweat Glands, Skin Permeation, Lymphatics, The Nails. Academic Press, London, 1978.

47. Sollner, K. The electrochemistry of porous membranes, with particular reference to ion exchange membranes and their use in model studies of biophysical interest. *Journal of Macromolecular Science - Chemistry*, **A3**(1):1-86, 1969.

48. Jacobson, H. Preparation and properties of a variable charge ion-exchange membrane. *Journal of Physical Chemistry*, **66**(3):570-572, March 1962.

49. Petri, E.M. and Stavaerman, A.J. Electrochemical properties of lupin seed protein. *Discussions of the Faraday Society*, **13**:151-159, 1953.

50. Picheny, M.A. and Grodzinsky, A.J. Method for measurement of charge in collagen and polyelectrolyte composite materials. *Biopolymers*, **15**:1845-1851, 1976.

51. Eisenman, G., Editor. Volume 1: Macroscopic Systems and Models, of *Membranes - A Series of Advances*. Marcel Dekker, Inc., New York, 1973.

52. Cronin, K.D. and Kirsner, R.L.G. Assessment of sympathectomy - the skin potential response. *Anaesthesia and Intensive Care*, **7**(4):353-357, 1979.

53. Venables, P.H. and Martin, I. The relation of palmar sweat gland activity to level of skin potential and conductance. *Psychophysiology*, **3**:302-311, 1967.

54. Elias, P.M. and Friend, D.S. The permeability barrier in mammalian epidermis. *The Journal of Cell Biology*, **65**:180-191, 1975.

55. Hill, M.W., Squier, C.A. and Linder, J.E. A histological method for the visualization of the intercellular permeability barrier in mammalian stratified squamous epithelia. *Histochemical Journal*, **14**:641-648, 1982.

56. Venables, P.H. and Christie, M.J. Mechanisms, instrumentation, recording techniques, and quantification of responses. Chapter 1 in *Electrodermal Activity in Psychological Research*, Edited by W.F. Prokasy and D.C. Raskin. Academic Press, New York, 1973.

57. Montagna, W. *The Structure and Function of the Skin*, 2nd Edition. Academic Press, N.Y., 1974.

58. Quinton, P.M. Sweating and its disorders. *Annual Review of Medicine*, **34**:429-52, 1983.

59. Thaysen, J.H. The sweat glands. Chapter 13 in *Membrane Transport in Biology*, Volume 3: Transport Across Multi-Membrane Systems, edited by G. Giebisch, pp. 379-414. Springer-Verlag, Berlin, 1978.

60. Kitson, N. and Van Lennep, E.W. Intercellular junctions and the permeability barrier in human sebaceous glands. *The British Journal of Dermatology*, **110**:601-606, 1984

61. Geddes, L.A. *Electrodes and the Measurement of Bioelectric Events*, Wiley-Interscience, New York, 1972.

62. Jaffe, L.F. and Nuccitelli, R. Electrical controls of development. In *The Annual Review of Biophysics and Bioengineering*, **6**:445-76. Annual Reviews, Inc., Palo Alto, California, 1977.

63. Ebling, F.J. *Textbook of Dermatology*, Second Edition, Volume 1, edited by A. Rook, D.S. Wilkinson and F.J. Ebling. Blackwell, Oxford, 1972.

64. Yamamoto, T. and Yamamoto, Y. Non-linear electrical properties of skin in the low-frequency range. *Medical and Biological Engineering and Computing*, **19**:302-310, 1981.

65. Ott, H.W. *Noise Reduction Techniques in Electronic Systems*, John Wiley, New York, 1976.

66. Morrison, R. *Grounding and Shielding Techniques in Instrumentation*, 2nd Edition. John Wiley, New York, 1977.

67. FASEB. *Biological Handbook: Blood and Other Body Fluids.* Sections II: Blood Electrolytes, 21-23 and XXIV: Dermal Secretions. edited by P.L. Altman, pp 467-468, 1982. W.B. Saunders, Philadelphia.

68. Dole, V.P. and Thaysen, J.H. Variation in the functional power of human sweat glands. *The Journal of Experimental Medicine*, **98**:129 -143, 1953.

69. Goodman, L.S. and Gilman, A., Editors. *The Pharmacological Basis of Therapeutics*, 5th Edition. MacMillan, New York, 1975.

70. Agrawala, A.K. and Kulkarni, A.V. A sequential approach to the extraction of shape features. *Computer Graphics and Image Processing*, **6**:538-557, 1977.

71. Webster, J.G. Reducing motion artifacts and interference in biopotential recording. *IEEE Transactions on Biomedical Engineering*, **BME-31**:823-826, 1984.

72. Höltzle, E. and Kligman, A.M. Mechanism of antiperspirant action of aluminum salts. *The Journal of the Society of Cosmetic Chemists*, **30**:279-295, September/October, 1979.

73. Reller, H.H. and Luedders, W.L. Pharmacologic and toxicologic effects of topically applied agents on the eccrine sweat glands. Chapter 1 in *Advances in Modern Toxicology*, Volume 4: Dermatotoxicology and Pharmacology, Edited by F.N. Marzulli and H.I. Maibach. John Wiley, New York, 1977.

74. Höltzle, E. and Kligman, A.M. Factors influencing the anti-perspirant action of aluminum salts. *The Journal of the Society of Cosmetic Chemists*, **30**:357-367, November, 1979.

75. Putterman, G.J., Strassburger, J. and Fitzgerald, J.J. *In vitro* sorption of aluminum complex to guinea pig stratum corneum. *The Journal of Investigative Dermatology*, **77**:319-324, 1981.

76. Illingworth, C.M. and Barker, A.T. Measurement of electrical currents emerging during the regeneration of amputated finger tips in children. *Clinical Physics and Physiological Measurements*, **1**:87-89, 1980.

77. Chan, S.H.H. What is being stimulated in acupuncture: evaluation of the existence of a specific substrate. *Neuroscience and Biochemical Reviews*, **8**:25-33, 1984.

78. Rosenblatt, S.L. The electrodermal characteristics of acupuncture points. *American Journal of Acupuncture*, **10**(2):131-137, 1982.

79. Pethig, R. *Dielectric and Electronic Properties of Biological Materials.* Wiley, N.Y., 1979.

80. Schaefer, H., Zesch, A. and Stüttgen, G. *Skin Permeability.* Springer-Verlag, Berlin, 1982.

81. Desoer, C.A. and Kuh, E.S. *Basic Circuit Theory*, Chapter 10. McGraw-Hill, New York, 1969.

82. Yamamoto, T. and Yamamoto, Y. Electrical properties of the epidermal stratum corneum. *Medical and Biological Engineering*, **14**:151-158, 1976.

83. Yamamoto, T. and Yamamoto, Y. Dielectric constant and resistivity of epidermal stratum corneum. *Medical and Biological Engineering*, **14**:494-499, 1976.

84. Quatrale, R.P, Cobel, D.W., Stoner, C.L and Felger, C.B. The mechanism of anitperspirant action of aluminum salts. II. Histological observations of human eccrine sweat glands inhibited by aluminum zirconium chlorohydrate glycine complex. *The Journal of the Society for Cosmetic Chemistry*, **32**:195-221, July-August 1981.

85. Papa, C.M. and Kligman, A.M. Sweat pore patterns. *The Journal of Investigative Dermatology*, **46**:193-197, 1966.

86. Weast, R.C. and Selby, S.M., Editors. *CRC Handbook of Chemistry and Physics*, 83rd Edition. The Chemical Rubber Company, Cleveland, Ohio, 1983-4.

87. Bartek, M., LeBudde, J.A. and Maibach, H.I. Skin permeability *in vivo*: comparison in rat, rabbit, pig and man. *The Journal of Investigative Dermatology*, **54**:114-123, 1972.

88. Kuno, Y. *Human perspiration* C.C. Thomas, Springfield, Illinois, 1956.

89. Breathnach, A.S. *The Ultrastructure of Human Skin*, J and A Churchhill, London, 1971.

90. Christie, M.J. and Venables, P.H. Basal palmar skin potential and the electrocardiogram T-wave. *Psychophysiology*, 8:779-786, 1971.

91. Heinz, E. *Electrical Potentials in Biological Membrane Transport.* Springer-Verlag, Berlin, 1981.

92. Oppenheim, A.V. and Schafer, R.W. Design of FIR filters using windows. In *Digital Signal Processing*, pp. 239-250. Prentice-Hall, New Jersey, 1975.

93. Rabiner, L.R., Schafer, R.W. and Dlugos, D. Correlation Method for Power Spectrum Estimation. In *Programs for Digital Signal Processing*, edited by The Digital Signal Processing Committee IEEE Acoustics, Speech, and Signal Processing Society, pp. 2.2-1 to 2.2-14. IEEE Press/John Wiley, New York, 1979.

94. Steward, E.G. Fourier transforms, convolution and correlation. Chapter 4 in *Fourier Optics, An Introduction*, pp. 61-82. Ellis Horwood, Ltd., Chichester, 1983.

95. Brigham, E.O. *The Fast Fourier Transform*, Prentice-Hall, Englewood Cliffs (NJ), 1974.

96. Frank, J. The Role of Correlation Techniques in Computer Image Processing. Chapter 5 in *Computer Processing of Electron Microscope Images*, edited by P.W. Hawkes, pp. 187-194. Springer-Verlag, Berlin and Heidelberg, 1980.

97. Bracewell,R.N. Fourier Techniques in Two Dimensions. Section 3, Part 1 in *Fourier Techniques and Applications*, edited by John F. Price, pp. 45-71. Plenum Press, New York, 1985.

98. Cramér, H. *Mathematical Methods of Statistics*, Princeton University Press, Princeton (NJ), 1946.

99. Snedecor, G.W. and Cochran, W.G. *Statistical Methods*, Sixth Edition, The Iowa State University Press, Ames(Iowa), 1967.

100. Maibach, H.I. Personal communication, 1985.

101. Bruno, M.F. *The Evaluation of Errors Due to Compton Scattering in Gamma-Ray Emission Imaging* Master's Thesis, Electrical Engineering and Computer Science, University of California, Berkeley, 1983.

102. Diggle, P.J. *Statistical Analysis of Spatial Point Patterns* Academic Press, London, 1983.

103. Hoppe, U., Sauermann, G. and Lunderstädt, R. Quantitative analysis of the skin's surface by means of digital signal processing. *Journal of the Society of Cosmetic Chemists*, **36**:105-123, March/April 1985.

104. Nuccitelli, R., Editor. *Ionic currents in development.* Volume 210 of Progress in Clinical and Biological Research. A.R. Liss, New York, 1986.

105. Gadsby, P.D. Visualization of the barrier layer through iontophoresis of ferric ions. *Medical Instrumentation*, **13**:281-283, Sept.-Oct. 1979.

A Human Use Approvals

BERKELEY: COMMITTEE FOR PROTECTION
OF HUMAN SUBJECTS

March 4, 1981

MR. CHRISTOPHER CULLANDER
Donner Laboratory/LBL

Re: "Microtopography of Skin Electric Properties" - Graduate Research - DOE 4454

The referenced protocol was reviewed and approved by the Committee for Protection of Human Subjects on February 27, 1981.

The number assigned this project is 81-2-87. Any future correspondence concerning this protocol should refer to this number. The expiration date of this approval is February 26, 1982. If the project is to continue beyond that date, a continuation protocol, including a brief progress report, must be submitted for Committee review and approval one month in advance of the expiration date.

With respect to the Committee's approval of your use of human subjects, any significant changes or untoward events must be brought promptly to the Committee's attention.

Should you have any questions regarding this matter, please contact the CPHS staff at the A&E Building, 642-7461.

A. Dobie Jenkins
Executive Officer

ADJ:fk

cc: Professor Thomas F. Budinger
Director Edward L. Alpen
Ms. Jan DeMoor ✓

BERKELEY: COMMITTEE FOR PROTECTION
OF HUMAN SUBJECTS

April 23, 1982

MR. CHRISTOPHER CULLANDER
Donner Laboratory/LBL

Re: "Microtopography of Skin Electrical Potentials" - DOE 4454
(Substudy of BUDINGER, T.F., "Experimental Medicine Clinical")

The referenced protocol was reviewed and approved by the Committee for Protection of Human Subjects on April 23, 1982.

The number assigned this project is 82-4-16. Any future correspondence concerning this protocol should refer to this number. The expiration date of this approval is April 22, 1983. If the project is to continue beyond that date, a continuation protocol, including a brief progress report, must be submitted for Committee review and approval one month in advance of the expiration date.

With respect to the Committee's approval of your use of human subjects, any significant changes or untoward events must be brought promptly to the Committee's attention.

Should you have any questions regarding this matter, please contact the CPHS staff at the A&E Building, 642-7461.

A. Dobie Jenkins
Executive Officer

ADJ:pb

cc: Director Edward L. Alpen
Ms. Jan DeMoor
Professor T. F. Budinger

BERKELEY: COMMITTEE FOR PROTECTION
OF HUMAN SUBJECTS

May 16, 1983

MR. CHRISTOPHER CULLANDER
Donner Laboratory/LBL

Re: "Microtopography of Skin Electrical Potentials" - Dissertation Research (under BUDINGER, T.F. "Experimental Medicine Clinical" - DOE 4454)

The referenced protocol was reviewed and approved by the Committee for Protection of Human Subjects on May 13, 1983.

The number assigned this project is 83-5-16. Any future correspondence concerning this protocol should refer to this number. The expiration date of this approval is May 12, 1984. If the project is to continue beyond that date, a continuation protocol, including a brief progress report, must be submitted for Committee review and approval one month in advance of the expiration date.

With respect to the Committee's approval of your use of human subjects, any significant changes or untoward events must be brought promptly to the Committee's attention.

Should you have any questions regarding this matter, please contact the CPHS staff at the A&E Building, 642-7461.

A. Dobie Jenkins
Executive Officer

ADJ:sb
cc: Acting Director T.L. Hayes
Executive Officer Jan DeMoor
LBL Human Use Committee
Professor Thomas F. Budinger

BERKELEY: COMMITTEE FOR PROTECTION
OF HUMAN SUBJECTS
(642-7461)

June 22, 1983

MR. CHRISTOPHER CULLANDER
Donner Laboratory/LBL

Re: "Microtopography of Skin Electrical Potentials" - Dissertation Research - (Under Dr. Budinger's "Experimental Medicine Clinical" - DOE 4454)

The referenced project as revised per your addendum of early June, 1983, was reviewed and approved by the Committee for Protection of Human Subjects on Friday, June 17, 1983.

The number assigned this addendum is 83-6-39. Please refer to this number in any future correspondence concerning this project. The expiration date of this approval is June 16, 1984. If the project is to continue beyond that date, a continuation protocol, including a brief progress report, must be submitted for Committee review and approval one month in advance of the expiration date.

With respect to the Committee's approval of your use of human subjects, any significant changes or untoward events must be brought promptly to the Committee's attention.

Should you have any questions regarding this matter, please contact the CPHS staff at the A&E Building.

A. Dobie Jenkins
Executive Officer

ADJ:fk

cc: Dr. Thomas F. Budinger
Director Thomas L. Hayes
Ms. Jan DeMoor

This report was done with support from the Department of Energy. Any conclusions or opinions expressed in this report represent solely those of the author(s) and not necessarily those of The Regents of the University of California, the Lawrence Berkeley Laboratory or the Department of Energy.

Reference to a company or product name does not imply approval or recommendation of the product by the University of California or the U.S. Department of Energy to the exclusion of others that may be suitable.

LAWRENCE BERKELEY LABORATORY
TECHNICAL INFORMATION DEPARTMENT
UNIVERSITY OF CALIFORNIA
BERKELEY, CALIFORNIA 94720